RF Project 760931/710709
Final Report

the
ohio
state
university
research foundation
1314 kinnear road
columbus, ohio
43212

THE ORTHOGONAL IN-SITU MACHINING OF SINGLE AND POLYCRYSTALLINE ALUMINUM AND COPPER

Dissertation
by
Paul H. Cohen, B.S., M.S.

Project Title:

DEFORMATION STRUCTURES IN METAL CRYSTALS
DUE TO WEAR AND MACHINING AT HIGH SPEEDS

J. T. Black, Principal Investigator

For the Period
December 1, 1977 - December 31, 1981

NATIONAL AERONAUTICS AND SPACE ADMINISTRATION
Lewis Research Center
Cleveland, Ohio 44135

Grant No. NSG-3164

May, 1982

THE ORTHOGONAL IN-SITU MACHINING
OF SINGLE AND POLYCRYSTALLINE ALUMINUM AND COPPER
VOLUME I

DISSERTATION

Presented in Partial Fulfillment of the Requirements
for the Degree Doctor of Philosophy in the
Graduate School of The Ohio State University

By

Paul H. Cohen, B.S., M.S.

* * * * *

The Ohio State University
1982

Reading Committee:

Dr. J. T. Black, Chairman
Dr. T. Altan
Dr. W. A. T. Clark
Dr. R. Hoagland

Approved By

Adviser
Department of Industrial
and Systems Engineering

DEDICATION

The dissertation and all the work which went into it is dedicated to my late father, Jack Cohen, and late uncle, Selwyn Goodman. Without their guidance and inspiration, it would not have been possible.

ACKNOWLEDGEMENTS

The author would like to express his deep gratitude and appreciation to his adviser, Dr. J. T. Black, for his guidance, patience and friendship during his education, as well as his family for making him feel like a part of theirs.

Professors T. Altan, W. A. T. Clark, R. Hoagland, D. Kibbey and K. H. Moltrecht of The Ohio State University also deserve special thanks for their time, help and contributions to my education.

Special thanks are due to Dr. R. Harmer and the Materials and Ceramics Laboratory at the University of Dayton Research Institute for allowing the author to use their X-ray and scanning electron microscopy facilities, as well as Mr. D. Wolf and Mr. S. Elliot for their help.

The author also wishes to express his gratitude to Mr. Clarence James and Mr. Cedric Sze of The Ohio State University for their contributions in the design and construction of the in-situ hardware and instrumentation, as well as their friendship.

In addition, the author would like to thank Dr. Robert Bill and NASA for the financial support extended to the author through NASA Grant NSG-3164.

Lastly, the author thanks his mother and sister for their love, understanding and moral support during the course of this research.

VITA

[redacted] [redacted]	Born - [redacted]
1976	B.S.I.E., University of Rhode Island, Kingston, R. I.
1976 - 1980	Teaching Associate, Department of Industrial and Systems Engineering, The Ohio State University, Columbus, Ohio
1979	M.S., The Ohio State University, Columbus, Ohio
1980 - 1981	Research Associate, Department of Industrial and Systems Engineering, The Ohio State University, Columbus, Ohio

PUBLICATIONS

Cohen, P. H., Black, J. T., "Tool Life Distributions", Discussion of ASME Papers 76-WA/Prod36 and 76-WA/Prod37, Journal of Engineering for Industry, Vol. 97, No. 3, 1977.

Black, J. T., Cohen, P. H., Breneiser, D., "Residual Stress Distributions - A Probabilistic Design", Proceedings NAMRC VI, May 1978, pages 331-338.

Cohen, P. H., Black, J. T., "Development of a Standard Machining Data Machine", Proceedings NAMRC VIII, May 1980, pages 258-265.

Cohen, P. H., Black, J. T., Horne, J. G., Shih, A., "Orthogonal Machining of Single Crystals", Proceedings NAMRC IX, May 1981.

Cohen, P. H., Lahoti, G., Altan, T., "Computer-Aided Design of a Roll Pass Schedule for the Shape Rolling of Round Rod From Square Bar", Proceedings NAMRC IX, May 1981.

FIELDS OF STUDY

Major Field: Industrial and Systems Engineering

Studies in Metal Cutting.	Professor J. T. Black
Studies in Metal Forming.	Professor T. Altan
Studies in Metallurgy.	Professors W. A. T. Clark and R. Hoagland

TABLE OF CONTENTS

LIST OF TABLES

LIST OF FIGURES

LIST OF SYMBOLS

Text

C, C_1, C_2, n	constants
b_1	initial width
b_2	final width
F	friction force
F_H	horizontal force
F_n	force normal to shear force
F_s	shear force
F_v	vertical force
ℓ	length of contact
ℓ_f	length of sliding contact
ℓ_s	length of sticking contact
ℓ_{s1}	length of non-uniform sticking contact
ℓ_{s2}	length of uniform sticking contact
N	force normal to friction
r	chip thickness ratio
R	resultant force
t_1	depth of cut
t_2	thickness of chip
u	specific energy
u_f	specific energy due to friction
u_s	specific energy due to shear
V	cutting velocity
V_c	chip velocity
V_s	shear velocity
$\dot{W}$	energy rate
$\dot{W}_f$	energy rate due to friction
$\dot{W}_s$	energy rate due to shear
α	back rake angle
β	friction angle
γ	shear strain
θ	orientation of single crystal
θ^*	orientation of crystal relative to cutting tool.
μ	coefficient of friction
σ	normal stress on rake face
σ_{max}	maximum stress on rake face
σ_n	normal stress on shear plane
τ_f	shear stress on rake face
τ[illegible]	shear stress in lamella

τ_S	dynamic shear stress
τ_{SF}	shear stress in shear front
ϕ	shear angle

Computer Printouts

AS	shear area (in.^{2})
DEG	orientation (degrees)
DIR	direction of resultant ($\beta - \alpha$) (deg.)
F	friction force (lbs.)
FH	horizontal force (lbs.)
FN	force normal to shear force (lbs.)
FS	shear force (lbs.)
FV	vertical force (lbs.)
HPU	specific horsepower (hp/in^3/min)
MU	coefficient of friction
N	force normal to friction (lbs.)
PHI	shear angle (degrees)
PUS	proportion of energy in shear
SN	normal stress on the shear plane (lbs./in.^{2})
TAU	dynamic shear stress (lbs./in.^{2})

CHAPTER I.

INTRODUCTION

Metal cutting is a plastic deformation process characterized by large strains, exceptionally high strain rates, and few constraints on the deformation which occurs in a small volume. Each of these factors cause metal cutting to be a unique process, difficult to understand. In addition, the dynamic shear (flow) stress and shear angle, the two variables which define the tool-workpiece interaction are not directly measurable. They are calculated based on measurements of a frequently curled, always jagged and uneven chip and thus subject to large error. As a consequence, some of the results predicted by the basic mechanics of the process have never been verified. Compared with other forms of plastic deformation, very little is known and understood about metal cutting.

Although metallurgists have long performed single crystal deformation experiments to learn the fundamental aspects of several modes of deformation, relatively few single crystal machining experiments have been performed.

In order to view small scale deformation to gain a greater qualitative understanding of deformation processes, experiments done within a Scanning Electron Microscope (SEM) or in-situ have been performed. Some have even been instrumented for the extraction of quantitative data. Although there are many examples of dynamic in-situ testing in tensile, torsional and fatigue modes of deformation, only three examples of in-situ machining exist in the literature, only one of which has been instrumented to measure forces (see Chapter II).

From the above discussions, it is clear that there is a great deal to be gained in performing dynamic in-situ machining experiments on single crystals with a fully instrumented cutting stage capable of recording the deformation (on video tape) while measuring force components, tracking crystal orientation, as well as a clock for timing events within a fraction of a second. Such a system would allow for high magnification and resolution studies of polycrystalline mechanics as well as those of single crystals.

CHAPTER II

LITERATURE REVIEW

Introduction

Perhaps the simplest definition of machining is the removal of material in the form of chips from a workpiece, usually by machine. Despite this simple definition, metal cutting is a very complex phenomenon which is not fully understood. The chip forming process in metal cutting is an extreme and unique deformation process distinguished by:

1. Exceptionally large strains.(1)
2. Unusually high strain rates resulting from an extremely small plastic zone (of questionable size and shape).(1)
3. The rubbing over the tool rake face of a freshly formed surface which is chemically clean and chemically active.
4. The large number of process parameters, like speed and feed, which can have widely varied settings.
5. A large number of metallurgical parameters in the workpiece and tool materials which influence the process.

While there is no agreement on the shape of the deformation zone, it is, however, generally accepted that the magnitude of the shear stress at which the cutting process operates will be constant for a given material at a given temperature. It should be noted that this characteristic shear stress (flow stress) is different from the flow stress for other metal deformation processes since the material is constrained and deformed in a unique manner.

As mentioned, metal cutting is a chip forming process. Three types of chips have been traditionally identified (2,3). The Type I or discontinuous chip (Figure 2.1) occurs when a brittle work material is cut and severe strain causes periodic fractures in the primary (shear) deformation zone. Discontinuous chips may also be produced when ductile materials are machined at very low speeds and high feeds(4). The Type II or continuous chip (Figure 2.1) is achieved in the machining of most ductile metals. Most metal cutting research has dealt with this chip type since it is a steady-state process. When certain conditions between the cutting tool and chip exist, it is possible for the chip material to actually weld to the rake face of the tool forming a built-up edge (BUE). This BUE material increases friction which causes layer upon layer of chip material to build up until it becomes unstable, breaks off, and is carried away either by the chip or the work. This is known as a Type III Chip - continuous with a built-up edge (Figure 2.1).

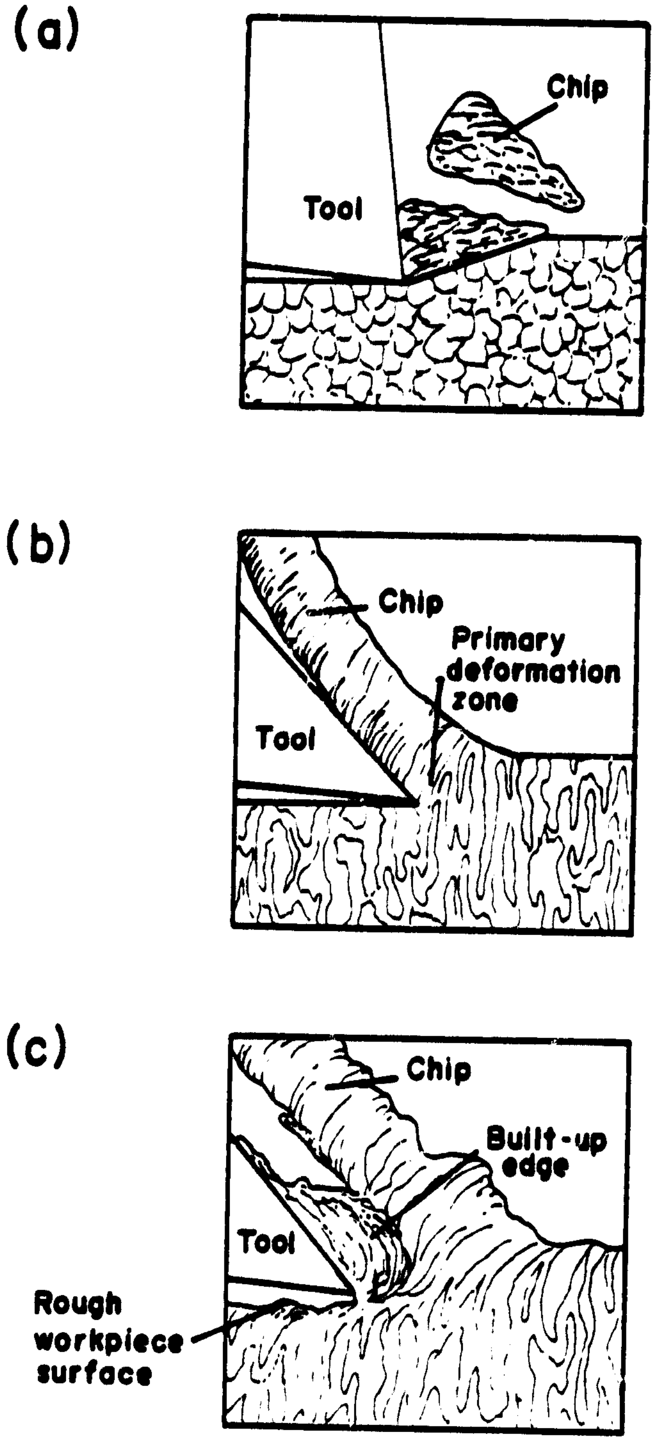

Figure 2.1. Chip Types in Metal Cutting

Merchant Analysis

The classical thin zone mechanics model was first proposed in this country by Merchant in 1945(3). The mechanics were developed for orthogonal cutting with a Type II chip with a planar shear process coupled with the following additional assumptions:

1. The tool tip is sharp and no rubbing or ploughing occurs between the tool and the workpiece.
2. The deformation is two-dimensional or orthogonal, i.e., no side spread.
3. The stresses on the shear plane are uniformly distributed.
4. The resultant force R on the chip is equal, opposite, and colinear to the force R' to the chip at the tool chip interface.

Merchant demonstrated the mechanism of shear with the analogy shown in Figure 2.2 where the metal is assumed to be displaced forward like a deck of cards. During this process the crystal structure will elongate in a direction defined by ψ which is different from the angle of shear. Each element has a finite thickness ΔS which is displaced through a distance ΔX with respect to its next closest element. Hence the shearing strain is given by

$$\gamma = \frac{\Delta S}{\Delta X} \qquad (2.1)$$

and from the geometry of Figure 2.2 it can be shown that

$$\gamma = \cot(\phi) + \tan(\phi - \alpha) \qquad (2.2)$$

where ϕ is the shear angle and α the back rake angle. Similar geometrical reasoning also yields that the direction

ORIGINAL PAGE IS
OF POOR QUALITY

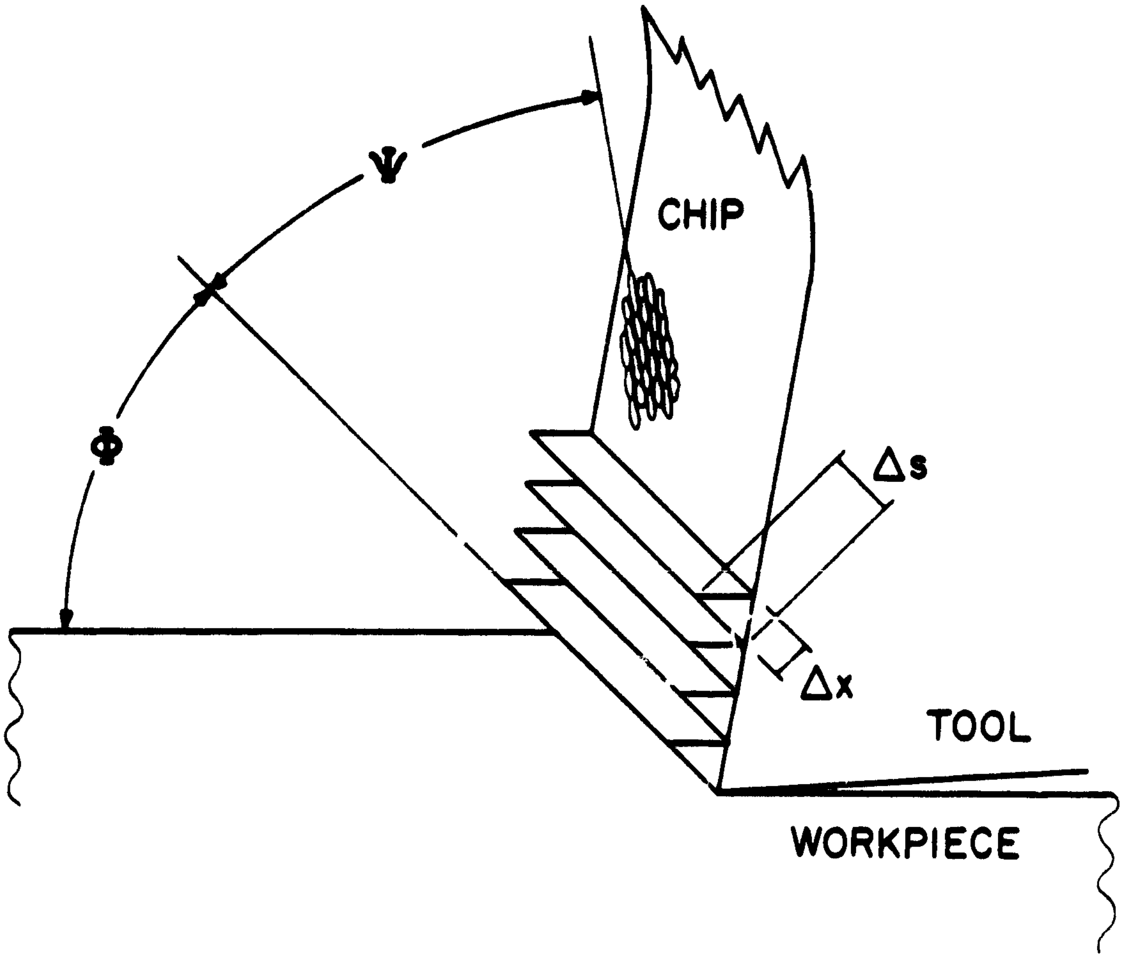

Figure 2.2. Schematic Representation of Shearing Strain, γ, in Orthogonal Cutting

of crystal elongation is

$$2 \cot (2\psi) = \cot (\phi) + \tan (\phi - \alpha) \qquad (2.3)$$

where ψ represents the direction of elongation. Thus the elongation direction and shearing strain are related by

$$\gamma = 2 \cot (2\psi) \qquad (2.4)$$

As previously stated, one unique characteristic of metal cutting is its very large strain. Strains on the order of 2 to 3 or more are quite common.

Simple velocity relationships can also be derived (from Figure 2.3) since the velocity of the chip (V_c) relative to the workpiece (V_s) must equal the vector sum of the velocity of the chip relative to the tool (V_c) and the velocity of the tool relative to the workpiece (V). Thus,

$$V_c = \frac{\sin (\phi)}{\cos (\phi - \alpha)} V \qquad (2.5)$$

$$V_s = \frac{\cos (\alpha)}{\cos (\phi - \alpha)} V \qquad (2.6)$$

where α is the back rake angle of the tool and ϕ the shear angle. The strain can now be expressed in terms of velocity as

$$\gamma = \frac{V_s}{V \sin (\phi)} \qquad (2.7)$$

and the strain rate of the cutting process by

$$\dot{\gamma} = \frac{\Delta S}{\Delta X \Delta t} = \frac{V_s}{\Delta X} = \frac{\cos (\alpha)}{\cos (\phi - \alpha)} \cdot \frac{V}{\Delta X} \qquad (2.8)$$

where ΔX is the thickness of the deformation zone, and Δt is the time to obtain the final value of strain. Typical strain rate values in metal cutting are of the order of 10^6

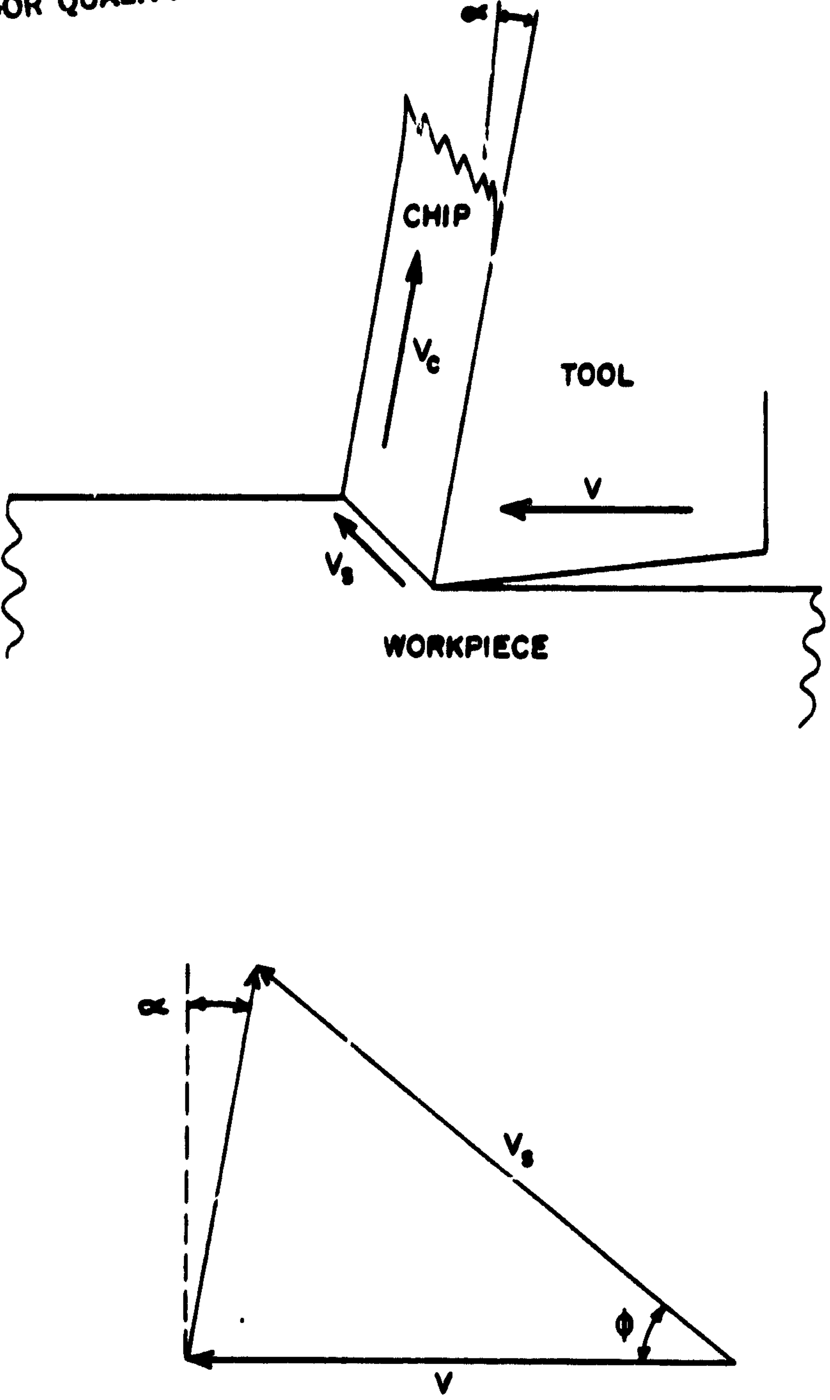

Figure 2.3. Velocity Relationships in Orthogonal Cutting

seconds^{-1}, a high value when compared with strains of 10^{-3} seconds^{-1} for ordinary tensile testing and 10^{3} seconds^{-1} for the most rapid impact tests$^{(5)}$.

The process of metal cutting has three identifiable deformation zones. The primary one involves the periodic shearing of the metal at the shear zone, but this is preceded by compression deformation on the workpiece. A secondary deformation involves the contact region between the chip and tool called the tool-chip interface. The force components acting on the shear plane and tool-chip interface are shown in Figure 2.4 in the free body diagram of the chip. The shear deformation has a force acting parallel to the shear zone (F_s) and one normal to it (F_N). The chip surface adjacent to the rake face rubs the tool with a velocity V_c. The resulting frictional force, F, is therefore parallel to the rake face while N is the force normal to the friction force. All of the force components acting on the deformation zones may be expressed in terms of the measured force components - the horizontal cutting force F_H and its perpendicular force F_V. F_H is sometimes called F_c the cutting force or F_p, the power force while F_v is called F_t or F_q by other authors. On the rake face

$$F = F_H \sin(\alpha) + F_v \cos(\alpha) \qquad (2.9)$$

$$N = F_H \cos(\alpha) - F_v \sin(\alpha) \qquad (2.10)$$

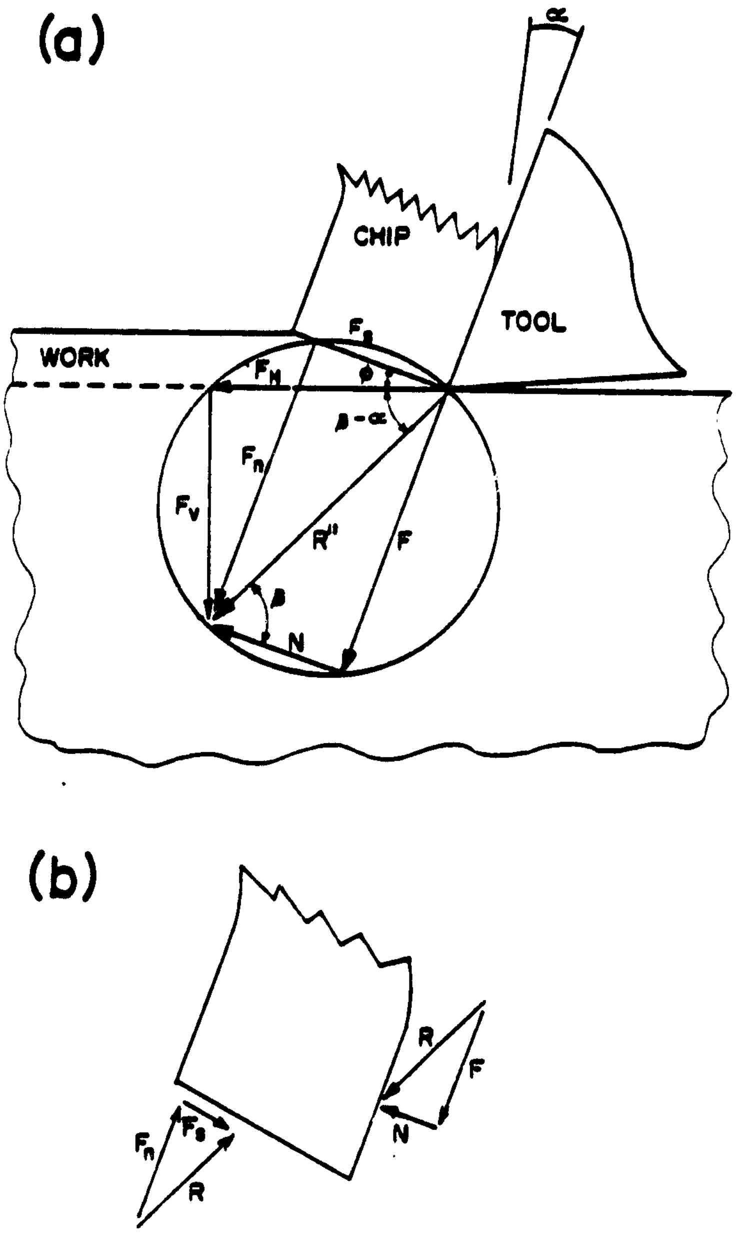

Figure 2.4. The Geometry and Forces in Orthogonal Cutting

the coefficient of friction μ on the rake face may be similarly expressed

$$\mu = \frac{F}{N} = \frac{F_H \sin(\alpha) + F_V \cos(\alpha)}{F_H \cos(\alpha) - F_V \sin(\alpha)} = \tan(\beta) \quad (2.11)$$

where β is the friction angle. This concept of friction implies the friction force F and its normal N are uniformly distributed over the tool-chip interface.

The forces along the shear zone may be written

$$F_s = F_H \cos(\phi) - F_V \sin(\phi) \quad (2.12)$$

$$F_N = F_H \sin(\phi) + F_V \cos(\phi) \quad (2.13)$$

As will be shown, the calculation of the shear (flow) stress, τ_s, requires knowledge of not only force magnitude but also the direction of flow. In metal cutting, the shear direction defines that direction. The shear angle can be determined in many ways. It can be directly measured through high speed photographic methods or "quick stop" methods which terminate the deformation with the chip intact so that the shear angle can be measured. The second group of methods uses the Continuity Theorem to relate the dimensions and motions of the deformed chip to the undeformed volume. By equating the volume of the deformed and undeformed chip

$$\rho_1 \ell_1 b_1 t_1 = \rho_2 \ell_2 b_2 t_2 \quad (2.14)$$

where ρ_1 is the density of the undeformed chip and $\ell_1 b_1 t_1$, the length, width and thickness respectively of the undeformed chip. The subscript 2 refers to the same quantities for the deformed chip. The material density remains constant despite the severe plastic deformation and the width was assumed to remain constant (Assumption 2 of the Merchant Analysis). Therefore

$$\frac{\rho_2}{\rho_1} = \frac{t_1}{t_2} = r \qquad (2.15)$$

where the quantity r is called the chip thickness or chip length ratio depending on which quantity was measured from the chip. Further geometry reveals that r is related to the shear direction by

$$\tan(\phi) = \frac{r\cos(\alpha)}{1 - r\sin(\alpha)} . \qquad (2.16)$$

The cross sectional area of the undeformed chip, A, is clearly the product of the width of the workpiece and the depth of cut. The inclined shear area is

$$A_s = \frac{A}{\sin(\phi)} = \frac{b_1 t_1}{\sin(\phi)} \qquad (2.17)$$

The shear stress (τ_s) and normal stress (σ_n) on the shear plane may then be found as

$$\tau_s = \frac{F_s}{A_s} = \frac{F_H\cos(\phi) - F_v\sin(\phi)}{b_1 t_1/\sin(\phi)} \qquad (2.18)$$

$$\sigma_n = \frac{F_N}{A_s} = \frac{F_H\sin(\phi) + F_v\cos(\phi)}{b_1 t_1/\sin(\phi)} \qquad (2.19)$$

During a cut, the total energy required per unit time (power) is the product of the horizontal force F_H and the cutting velocity V. If the total energy required per unit time is divided by the metal removal rate, $b_1 x t_1 x V$, we obtain the energy per unit time or specific energy, u, as

$$u = \frac{F_H V}{b_1 t_1 V} = \frac{F_H}{b_1 t_1} . \qquad (2.20)$$

This specific energy may be partitioned into four portions (6,7):

1. The shear energy per unit volume, u_s, required to produce gross deformation in the shear zone

$$u_s = \frac{F_s V_s}{b_1 t_1 V} = \frac{\tau_s V_s}{V \sin (\phi)} \qquad (2.21)$$

2. The friction energy per unit volume, u_f, expended as the chip slides along the rake face of the tool

$$u_f = \frac{F V_c}{V b_1 t_1} \qquad (2.22)$$

3. The kinetic energy per unit volume required to accelerate the chip (momentum specific energy).

4. The surface energy per unit volume required to produce the new uncut surface area.

The kinetic specific energy and surface specific energies are negligible in typical cutting operation, thus

$$u \simeq u_s + u_f \qquad (2.23)$$

where u_s accounts for approximately 75% or more of the total energy(7).

While the force dynomometer method just described seems to be the most prevalent in research work, there are other ways to determine the power of energy consumed cutting. A wattmeter(8, 9) may be used to measure electrical inputs to the machine tool but this method is subject to motor efficiency and friction conditions in the machine and generally not very precise. Perhaps the oldest method utilizes caliorimeter techniques(10, 11). A heat balance is used to determine the energy expended. This method is reliable but only for those machine tools whose configurations facilitate good calorimeter enclosures. Another method utilizes a pendulum-hammer to measure energy consumption(12). The hammer is dropped from one height and rises to a different one after performing the cut. This difference in height reflects the energy that was used in the cutting operation. Changes in the momentum of a work-piece and fly-wheel have been used to measure the energy lost on a cut(13).

The idea of using a pendulum hammer and measuring the speed before and after the cut as done in momentum machining has been employed in the design of a Standard Machining Data (SMD) Machine(14). The SMD Machine, a retrofitted impact tester where the hammer has been replaced by a cutting tool and the normal specimen holder replaced by a piezoelectric dynamometer with a work-holding vise mounted on top, can measure the energy absorbed in the cutting process in two independent ways: 1) by dynamometry (F_H/b_1t_1) and 2) by calculating the change in kinetic energy as determined by measuring the speed of the moving tool immediately prior to and after the cut by the use of photo-coupled interrupter modules. Calculation of specific energies by changes in speed (kinetic energy) is a more accurate measure since the errors associated with the representation and reading of the force trace are eliminated. In addition, materials which yield non-continuous chips can be accurately evaluated.

Shear Angle Relationships

Merchant(3) was also able to obtain a functional relationship between shear angle and the friction angle. By applying Hamilton's Minimum Energy Principle, a continuum mechanics principle which states that the cutting process will always adjust itself to a minimum energy condition ($dF_H/d\phi = 0$). Merchant obtained(3)

$$\phi = \frac{\pi}{4} - \frac{1}{2}(\beta - \alpha) \qquad (2.24)$$

Many others have attempted to correlate the shear angle and friction angle. These continuum mechanics relationships fall into the general form

$$\phi = C_1 + C_2(\beta - \alpha) \qquad (2.25)$$

where C_1 and C_2 are empirical constants(1). Lee and Shaffer applied plasticity theory for an ideal rigid-plastic material, while assuming that the deformation occurred on a thin shear plane. They obtained values of $\frac{\pi}{4}$ and 1 for C_1 and C_2 respectively. The Lee and Schaffer model was subsequently modified by Cook, Shaw and Finnie(15) to include the shear plane as one which did not have maximum stress. They obtained

$$\phi = \left(\frac{\pi}{4} + \eta'\right) - (\beta - \alpha) \qquad (2.26)$$

where η' is not constant but varies with material. A summary of these and others from this family of equations are shown in Table 2.1.

The results of the Ernst and Merchant and Lee and Schaffer models are shown in Figure 2.5. Neither model compares favorably with experimental data. This, however, is to be expected since an attempt is being made to correlate the two deformation zones. The phenomena at these zones is not completely understood, nor is the chip fully constrained so as to make standard mathematical tools applicable. Continuum models fail for a multitude of reasons, however. In general they tend to make simplifying assumptions which are not entirely correct; i.e., that stress on the rake face is uniformly distributed or that the shear plane is (or is not) a plane of minimum energy or maximum stress. Continuum models do not take the material being machined and its properties into account.

Another method for predicting the shear angle uses Hill's Deformation Criteria to suggest that

$$\phi = \phi_o + C\sigma \qquad (2.27)$$

where C is an empirical constant, σ the surface slope of the workpiece, and ϕ_o the shear angle at zero surface slope. Using this criteria Kainth and Gupta(17) have obtained values of the constant C ranging from 0.2 to 1.0. All authors have concluded that C is not a material constant

Table 2.1. Summary of Shear Angle Prediction Equations(16)

INVESTIGATOR	DATE	C_1	C_2	EXPRESSIONS
Piispanen (Finland)	1937	$\pi/4$	1/2	
Merchant (USA)	1945	$\pi/4$	1/2	
Piispanen (Finland)	1927	$(\cot^{-1}K)/2$ (where $\tau=\tau_o+K\sigma$)	1/2	
Stabler (Scotland)	1951			$\frac{\pi}{4} - \beta + \alpha/2$
Hucks (Germany)	1951			$\frac{\pi}{4} - \frac{\tan^{-1}2\mu}{2} + \alpha$
Lee & Shaffer (USA)	1951	$\pi/4$	1	
Hucks (Germany)	1951			$\frac{\cot^{-1}K}{2} - \frac{\tan^{-1}2\mu}{2} + \alpha$ (where $\tau=\tau_o+K\sigma$)
Shaw, Cook, Finnie (USA)	1953			$\frac{\pi}{4} - \beta + \alpha + \eta'$

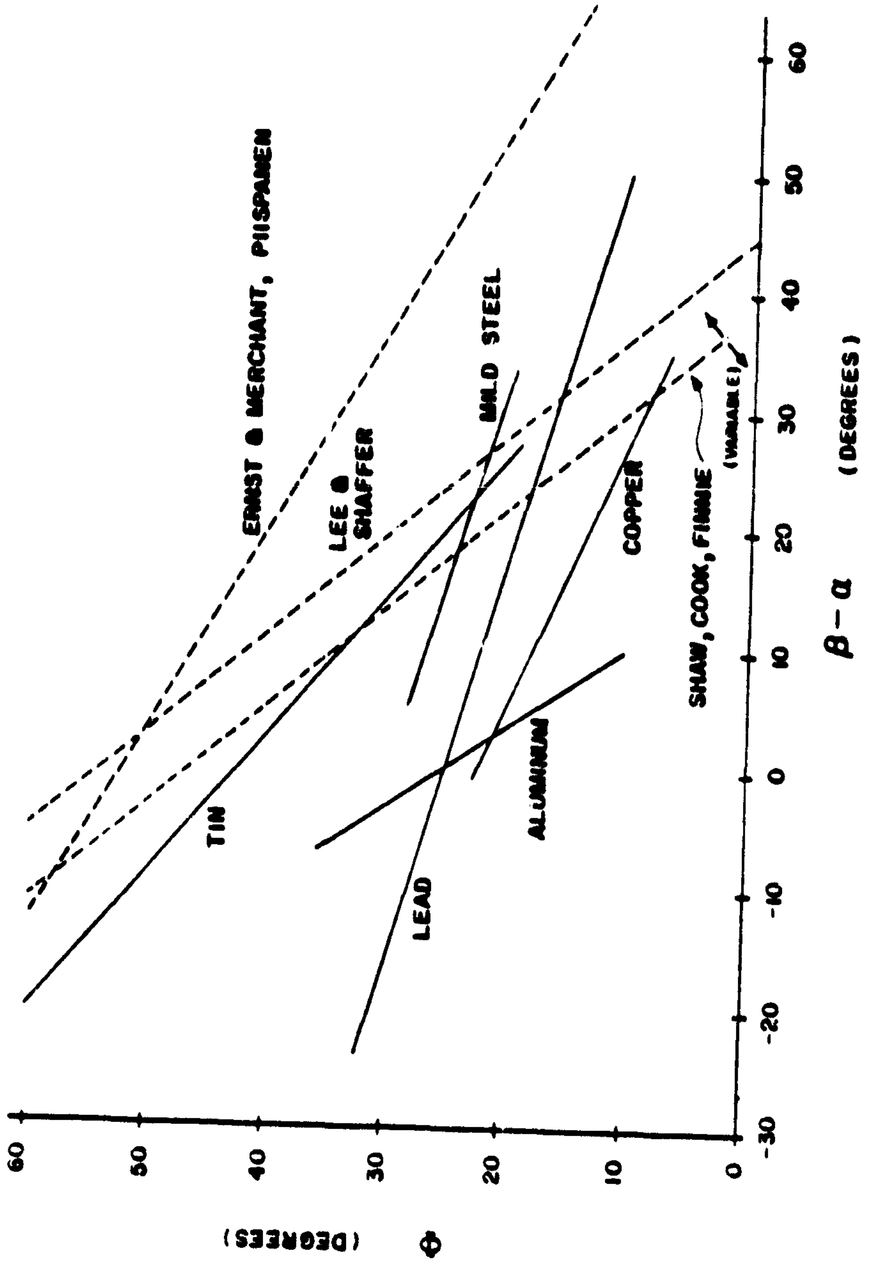

Figure 2.5. Shear Angle Predictions

and depends on the rake angle, surface slope, and steady state shear angle(17). Thus the results of this type of modeling have not been very successful. One of the more sophisticated continuum mechanics approached was by Kobayashi and Thomsen(18) who employed the Limit-Load Theorem and two new parameters, the effectiveness of the machine tool and the machinability of the workpiece to derive angle relationships and force relationships for orthogonal cutting. This analysis assumes a relationship between the shearing process at the shear plane and the friction process on the rake face (without proof or detailed consideration to the nature of the relationship). This analysis also assumes the shear to take place so as to consume minimum energy. This has been shown not to be the case by Ramalingam and Hazra in the machining of single crystals(19) but this approach may yet prove to be valid if a balance is considered between the tool-chip contact area and its loads with respect to the shear area and its loads.

Such an approach was taken by Rowe and Spick(20) where the thin zone approximation is used and the shear angle relationship is derived without reference to external forces and without assuming either a distribution or concept of secondary shearing stresses. Since it is not externally constrained, the shear plane is assumed to adopt a position such that the total energy expended in the system (the total energy expended on the shear plane plus the rake face) is minimum.

Considering first the rate of work done on the thin shear plane, it can be shown that

$$\dot{W}_s = \frac{dW_s}{dt} = F_s V_s = \frac{\tau_s t_1 w_1 V\cos(\alpha)}{\sin(\phi)\cos(\phi-\alpha)} \quad (2.28)$$

where $\dot{W}_s$ represents the shear work rate. Therefore, if the cutting conditions (t_1, w_1, V) are held constant, the rate of work on the shear plane will be proportional to the shear strain, $\cos\phi/\sin\phi\cos(\phi-\alpha)$.

The work rate on the rake face is needed to assess the total work rate and may be written as

$$\dot{W}_f = \frac{d\dot{W}_f}{dt} = FV_c = \frac{\tau_f w_2 \ell V\sin(\phi)}{\cos(\phi-\alpha)} \quad (2.29)$$

where $\dot{W}_f$ is the frictional work rate, τ_f the frictional shear stress and ℓ the contact length.

Thus the total work may be written as the sum of the friction and shear work rates as follows

$$\dot{W} = \dot{W}_s + \dot{W}_f = \frac{\tau_s t_1 w_1 V\cos\alpha}{\sin\phi\cos(\phi-\alpha)} + \frac{\tau_f w_2 \ell V\sin\phi}{\cos(\phi-\alpha)}. \quad (2.30)$$

The optimal shear angle, ϕ, is that angle which minimizes the total work rate, $\dot{W}$. As shown in Figure 2.6, the frictional work rate continuously increases with increasing shear angle (Curve 1) while the shear work rate (Curve 2) is a concave function of shear angle. As a result, the sum of the work rates (Curve 3) is a concave function with a distinct shear angle for minimum energy.

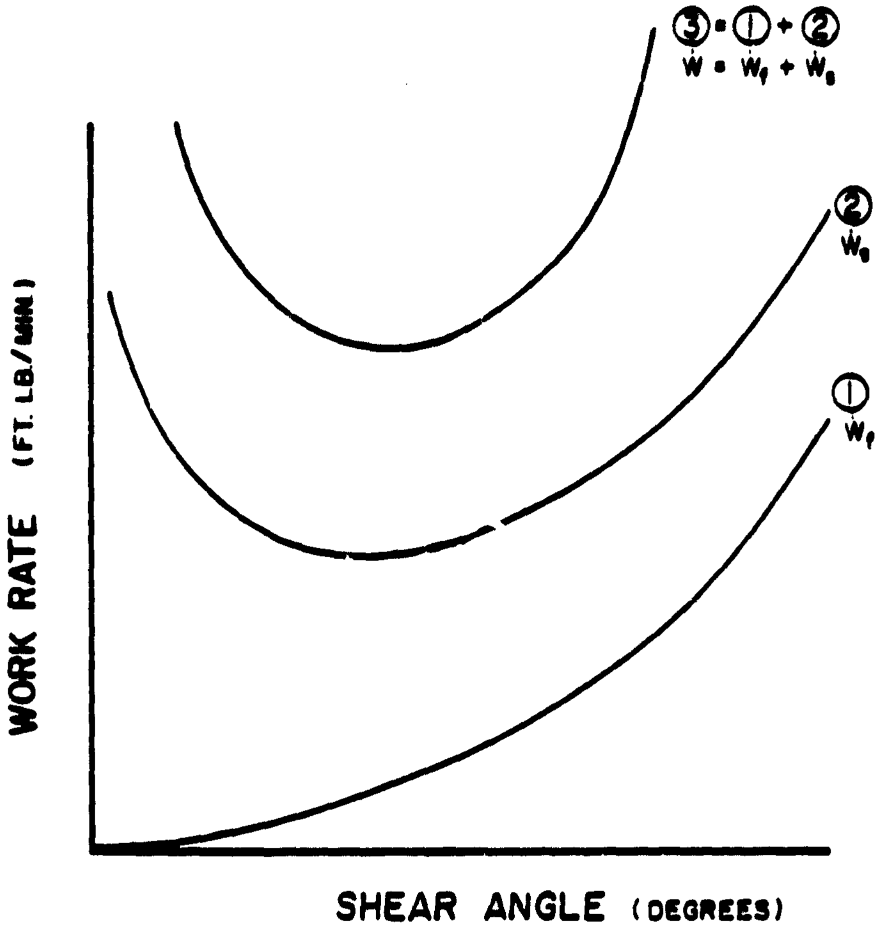

Figure 2.6. Work Rates in Metal Cutting for an Arbitrary Back Rake Angle

It should be noted that under "perfect" conditions of zero friction, that all materials should shear at 45°.

A variation of this method (21) assumes that the friction on the rake face arises from areas of both sticking and sliding friction due to a non-uniform distribution of shear stresses. The shear stress on the rake face is calculated from an "average" tool-chip contact length, which is a weighted average of the sticking region of constant shear stress and linearly decreasing shear stress over the remaining length. Machining experiments were performed on five workpieces with zero degree back rake angle carbide tools (21). Predicted values of shear angle for titanium and free machining steel were fairly close to the experimentally determined values, while nickel, copper, and low carbon iron showed poor agreement. One reason for this lack of agreement for the latter three materials is their sidespread during machining (i.e., a lack of adherence to plane strain conditions).

Energy rate methodology has also been applied to the three dimensional metal cutting problem (22, 23, 24). Usui, et al. partitioned the energy for the oblique cut into shear and frictional components using some orthogonal cutting geometric relationships and applying them as an approximation to the oblique case. The result is a complex descriptive model of the energy consumed in metal cutting expressed as a function of tool geometry, shear angle, cutting parameters (depth, width, speed), dynamic shear stress as well as friction angle, which is simulated to determine the shear angle that minimizes the total energy. However, the calculation of the friction angle necessitates that experiments be performed at equivalent orthogonal conditions and the results applied to the three dimensional case. Thus the model is not predictive in nature and assumes uniform shear and normal stress distributions on the rake face. As utilized by the authors, empirical expressions for shear friction angles were developed as functions of back rake angle and the component forces predicted for minimum energy. Thus the approach taken is really empirical.

Thick Zone Models

Besides the thin-zone models already mentioned, numerous thick-zone models have been developed. Palmer and Oxley(25) used cine film to monitor the paths of individual grains along the side of the workpiece. Their experimentally determined slip-line field and their basic model of the cutting process is shown in Figure 2.7. Careful observation of the figure shows that the chip is curved so as not to contact the tool until some distance up the rake face. The resultant force is shown to pass directly through the center of this contact. These assumptions are tenuous at best.

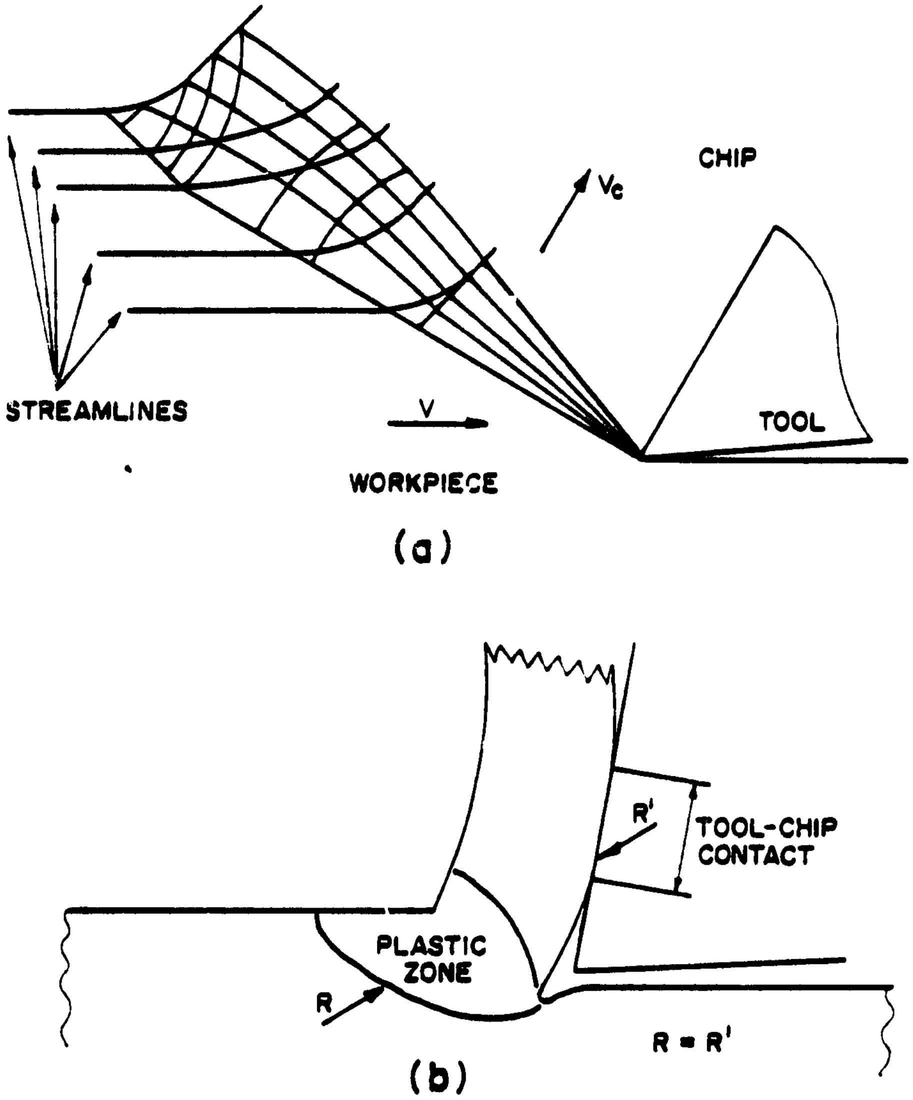

Figure 2.7. Thick Zone Models

Okushina and Hitomi(1) have done another thick-zone analysis which disregards slip-line fields and attempts to describe the deformation zone only utilizing the geometry of its boundaries. This analysis attempts to describe the shear process in terms of a speculative region in size, shape, and boundary conditions. This model was not totally successful either (see Figure 2.8).

It is difficult to give much credibility to thick-zone models, especially since the use of the scanning electron microscope to examine interrupted cut specimens of dynamic operations(26) has conclusively shown the deformation zone to be a narrow region, but not necessarily a flat plane.

Dislocation Mechanics

Being an unbounded process, there are obvious difficulties in obtaining a complete description of the cutting process utilizing continuum mechanics. Work has started in describing the process on a much more fundamental level, on the basis of line defects in the material (called dislocations) and their motions, interactions, annihilations, and multiplication. Dislocation Mechanics, besides dealing with the process on a more fundamental level, also gives physical insight into the experimentally proved constancy of the shear stress (or dynamic shear stress).

The shear stress has been shown to be related to the shear modulus G, dislocation density ρ, and Burgers Vector b.

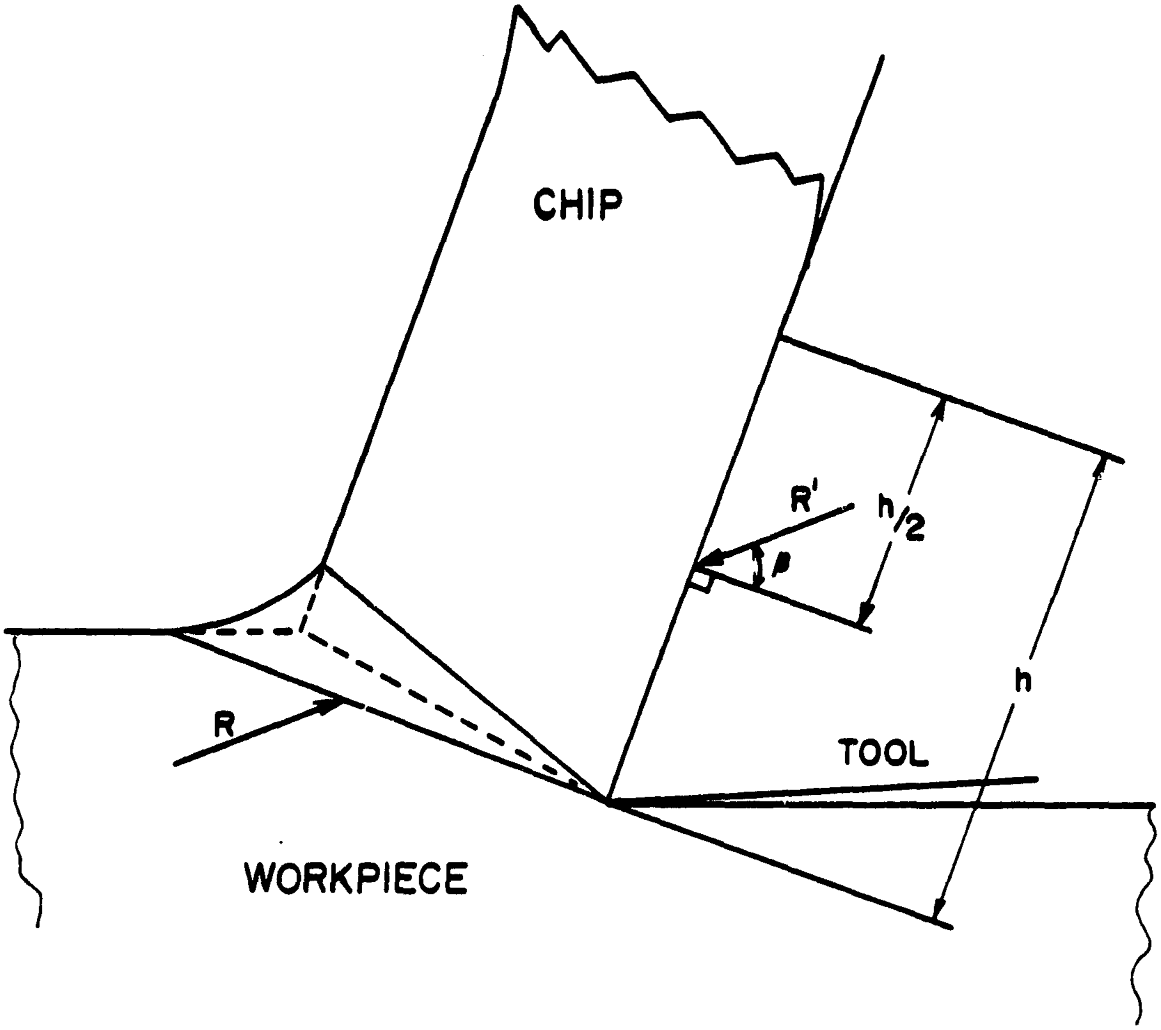

Figure 2.8. Okushina-Hitomi Model

An early study by Von Turkovich(27) applied this analysis to metal cutting obtaining

$$\tau_s = \alpha G b \rho^{1/2} \qquad (2.31)$$

where α is a constant. This model was based on the vacancy supersaturation induced climb of the dislocation as the controlling process in dynamic recovery to reach saturation hardening. This model has been shown fairly good correlation with the results of Ramalingam(19) but not with α as originally derived.

Stacking fault energy has also been shown to influence flow stress(27, 28). Black(28) correlated the stacking fault energy parameter γ/bG to the flow stress. The dimensionless parameter γ/bG was believed to be the principal factor which determines the work hardening behavior of fcc metals when γ is the stacking fault energy, b, the Burgers Vector and G the shear modulus of elasticity. Compression ahead of the shear produces a dislocation cell structure, which must be rearranged in some way by the shear process. Normally, dislocations must recombine in order to penetrate or circumvent barriers. This requires energy in the form of the applied stress which is developed during cutting. The model requires dislocation reassociation and measures the extent of dissociation by the stacking fault energy which reflects the energy needed for recombination. It is therefore reasonable to assume the relationship between the dynamic shear stress and the stacking fault energy. A high correlation was found and is shown in Figure 2.9(28).

The use of the scanning electron microscope to study the fundamental mechanism in metal cutting has revealed the process to be a discontinuous one(26, 28, 29, 30, 31). These studies show lamellae of the order of 2 to 4 μm separated by very thin planes known as shear fronts of thickness 200 to 400 Å. The periodic spacing observed is rather invariant to changes in the cutting conditions, being most influenced by crystallography which also influences the shear direction.

The most complete dislocation model of the cutting process has been done by Black(32). The model is based on the intermittent nature of the cutting process with dislocation sources operating from the tip of the tool. There is a rapid build-up in applied stress as the new dislocations from the tool tip intersect (pile-up against) the metastable subcell structures. When applied stress becomes sufficiently large, the new dislocations will cause some rearrangement of the metastable cells. A catastrophic shear front develops as a narrow band. The shear fronts develop in waves or sets, with a 2 to 4 μm spacing. There should be considerable heat generated during this stage. The catastrophic shear releases the applied strain energy and a sharp drop in the shear stress results, but very quickly

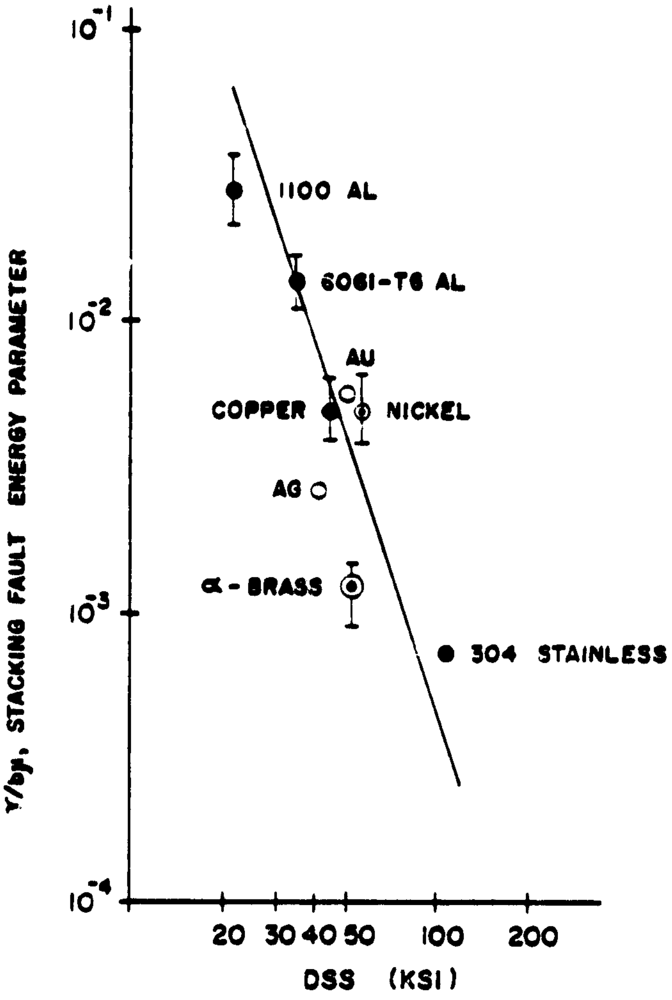

Figure 2.9. Stacking Fault Energy Parameter Correlated Against Dynamic Shear Stress

builds up again. The drop in shear stress cannot, however, be ordinarily detected since the shear front is microscopic and occurs in sets to form the lamella, and is not properly oriented for observation (see Figure 2.10).

The Cottrell-Stokes Law partitions the flow stress of a material into two portions - a thermally dependent portion τ_d and temperature independent part τ_g where

$$\tau_s = \tau_d + \tau_g \tag{2.31}$$

Black analogously models the dynamic shear stress as

$$\tau_s = \tau_{SF} + \tau_L \tag{2.32}$$

where τ_{SF} is the thermally activated flow stress in the shear front and τ_L is the athermally activated flow stress in the lamella. τ_L is due mainly to dislocation intersection while τ_{SF} is due mainly to the rearrangement of the metastable cell structure previously described. While not every premise of this model has been experimentally proven, it does, however, provide a reasonable and complete explanation of the process.

Additional Observations of the Cutting Process

As previously stated, metal cutting is a process in which intense plastic deformation takes place with extremely high strain rates. This has prompted some theories to attempt to connect the dynamic shear stress to strain rate and temperature. Bailey and Bhanvadia(33) have suggested that the deformation at the rake face of the tool may be

ORIGINAL PAGE IS
OF POOR QUALITY

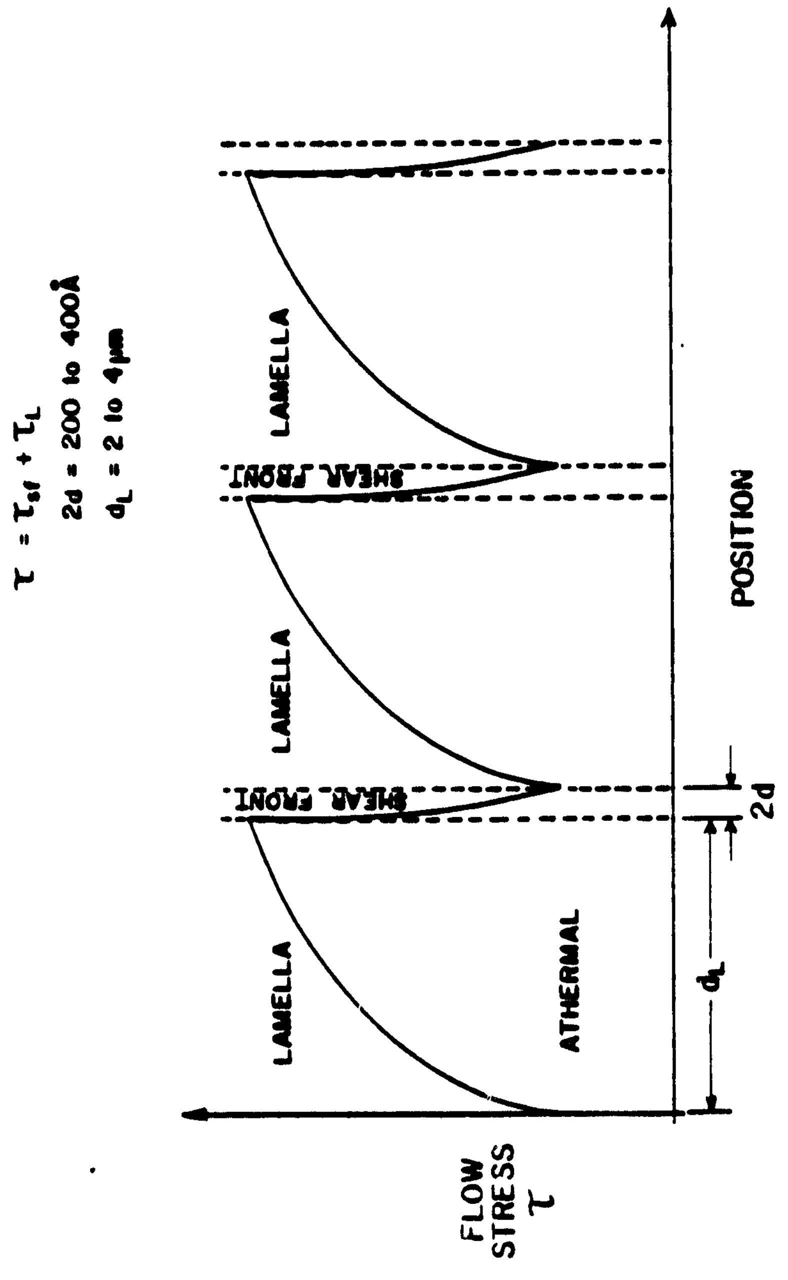

Figure 2.10. Black's Dislocation Model

thermally activated. They have attempted to correlate the temperature, velocity modified temperature, and strain rate with flow stress. They have used dislocation mechanics to explain the fundamentals of flow stress, but have used a thick-zone model with three zones of deformation to model the temperature-strain rate interaction.

The work of Sata(34) also states that changing temperature and strain rate effects flow stress. In a thick-zone analysis, he developed a velocity modified temperature which he believes to be the only parameter controlling flow stress. It is interesting to note that experimental work has shown dynamic shear stress to increase at exceptionally low strain rates (less than 2×10^4 $\sec^{-1}$ for copper) and remain constant for higher ones(25). Specific cutting energy has shown a similar trend(4).

Although there is still controversy regarding the theory and modelling of metal cutting there is, however, one concept which is generally accepted - that dynamic shear stress is a material constant over an extremely wide range of cutting conditions (see Table 2.2).

Single Crystal Machining

The plasticity of metal single crystals has been studied for many years in order to gain insights into the dislocation and workhardening behavior of metals. Much of the early work, as summarized by Schmidt and Boas(36) and

ORIGINAL PAGE IS
OF POOR QUALITY

Table 2.2. Experimentally Determined Values for Dynamic Shear Stress

Material	Cutting Speed V_c	Hardness	Bulk Temp of Workpiece	Measured Flow Stress D.S.S. (psi)	Notes
Aluminums					
6061-T6	20"/min	97 Bhn	R.T.	34,400±2000	Rolled Plate
6061-T5	537,2070 FPM		R.T.	34,200	T.S.=45,300 psi
6061-T6	30-4000 FPM	121±DPH	R.T.	36,300	(Extruded Tube)
High Purity (99.993%)	2500 FPM	35-36DPH	-326° F	31,604	
	2500 FPM	35-36DPH	90°F or R.T.	20.403	
	2500 FPM	35-36DPH	400°F	19,805	
1100	3060 fm/min	42-44DPH	-326°F	31,050	
1100	or 15000	42-44DPH	90°F	22,372	
1100	cm/sec	42-44DPH	400°F	19,615	
1100		42-44DPH	502°F	21,800	
1100 (99.0)	5/8 in/min		R.T.	21,200±6,200	Annealed single
1100	4.4 FPM	?	R.T.	13,300	crystal
1100 Annealed	5 FPM	*	R.T.	16,700	
1100 Hard	5 FPM	?	R.T.	17,200	
5080-0	1280-2080 SFPM	?	R.T.	20,300	
Gold	Slow	686 MN/m²	R.T.	20,300	
Gold (High Purity)	Slow	?	R.T.	40,300	
Austenitic S.S.	?	?	R.T.	91,300	
304 S.S.	?	?	R.T.	105,300±5000	
Coppers & Coppers Alloys					
Alpha Brass	20 in/min	89 Bhn	R.T.	52,600±6,200	T.S.=37,300 psi 69.7% Cu, 30.2% Zn
Alpha Brass	22-1760FPM	?	R.T.	54,800-72,900	
Alpha Brass	472,1720 FPM	?	R.T.	50,600	As rec'd. cold rolled
65-35 Brass	30-600FPM	149 DPH	R.T.	50-51,300	As rec'd. cold rolled
TPE Cu	30-600FPM	81 DPH	R.T.	44-45,300	
TPE Cu	250-700 FPM	?	R.T.	42,300	
TPE Cu	2500 FPM	83-86DPH	550°F	37,568	
TPE Cu	2500 FPM	83-86DPH	90°F	44,739	
TPE Cu	2500 FPM	83-86DPH	-326°F	55,627*	
TPE Cu	4-5 FPM	?	R.T.	36-39,000	
Copper	Low	1225 MN/m²	R.T.	35,600	Annealed
High Purity Cu	2500	120-126DPH	500°F	45,026	
High Purity Cu	2500	120-126DPH	90°F	57,273	
High Purity Cu	2500	120-126DPH	-326°F	67,310	
60-40 Brass	30 FPM	*	R.T.	47,300±1000	
Nickel	Slow	?	R.T.	61,300	
Nickel 200	*	140 BHN	R.T.	100,300	
Inconel 600	?	200 BHN	R.T.	100,300	
16-25-6 Alloy	250-310	207 BHN	R.T.	140,300±2500	
3816 Alloy	50-60	270 BHN	R.T.	156,300±5000	

* Values computed from published data. R.T. = Room Temperature

later by Mitchell(37) dealt with fcc crystals. By the mid fifties, transmission electron microscopy techniques were developed to image dislocations in thin foils directly. At this time, microscopists routinely employed ultramicrotomy techniques to obtain thin films from biological materials (composites of tissue and embedding plastics) for TEM examination and so it was natural for the microtomy technique to be used to obtain thin films of metals for TEM examination. These studies appear to be the first attempts to machine single crystals, as microtomy is a very refined version of orthogonal machining, generally employing diamond knives. These researchers quickly discovered that the thin films produced by microtomy had extensive dislocation tangles and complex arrangements due to the machining deformation, so microtomy techniques were, for the most part, discarded as a technique for obtaining thin films (most researchers turned to chemical or electrochemical thinning). As it was their objective to obtain thin films and not to study the process by which the films were made, few of the early investigators were concerned with the basic mechanism of machining, nor did they instrument their apparatus to measure cutting forces. Thus little quantitative information can be obtained from these early studies.

Clarebrough and Oglivie(38) were perhaps the first to machine single crystals in the late 1940's. Their work was published in 1950 by the American Society of Metals in a book which contained papers by the best known metal cutting researchers of that era. As a result, this work is relatively unknown and unrecognized. Clarebrough and Oglivie microtomed large grained polycrystals of lead (99.99% pure with the average grain size being 5 mm) produced by twenty-four hour annealing at 300°C. Grain boundaries as well as shear direction and chip morphology were clearly distinguishable by light microscopy.

All of the microtome cuts were performed using a High Speed Steel tool with a 0.00015 inch edge radius and 60-degree back rake angle. The depth of cut was kept constant at 0.0001 inch.

These cutting experiments revealed transverse markings across the top of the chip, perpendicular to the direction of cut. These transverse markings of lamella were seen to change periodicity when cutting a grain of different orientation. An accompanying change in shear direction was also observed. A built-up edge was also found to influence lamella spacing.

If a BUE was formed and the shear angle was small, the compression deformation ahead of the tool was observed to be greater than when no built-up edge was formed and the shear angle was large. Thus a strong correlation was found between crystallographic orientation and lamella spacing as well as shear direction and built-up edge.

R. Phillips at AEON Laboratories in England, machined single crystals in the late 1950's(39,40). A microtome with a diamond knife with 50° knife angle was used. Cutting speeds of 30 cm/s and depths of cut on the order of 100 microns were employed to obtain specimens for transmission electron microscopy. FCC aluminum and copper, as well as HCP magnesium and zinc metals, were machined. The maximum density FCC (111) plane was found to be the primary active slip plane, with some slip also occurring on the (100) plane. Thus, more than one slip system was activated.

Further tests(41) were performed on crystals with a (110) [100] orientation. An attempt was made to align the (111) plane approximately with the expected shear direction. Again, two slip directions were found when machining these aluminum single crystals and the chips varied in thickness by +15% indicating that the shear direction may have changed during the cut and multiple slip systems were operative. The chips displayed a classical shear front-lamella structure which could easily be distinguished from the more broadly spaced machine tool chatter markings(42).

Work by V. A. Phillips(43,44,45) reviewed and refined the microtomy techniques for metals but again the objective was to obtain thin films for optical and transmission electron microscopy While Phillips machined and discussed mostly polycrystals, he did observe that the most important factor controlling the deformation shear direction was the crystallographic orientation which also affected the shear front-lamella periodicity. Selected area diffraction (SAD) revealed in copper alumina chips that slip occurred on the (111) plane.

Ahlers and Vassamillet also microtomed copper alloys using diamond knives with similar tool geometry and speed of 0.38 mm/sec(46). High dislocation densities in the chips on the order of 10^{11} per square centimeter were verified. In addition to dislocation networks, long, straight fault bands were observed in pure copper and Cu-5at.% Ge and not in Cu-9.5 at.% Ge. The dislocations were arranged in irregular networks in the Cu and Cu-5 at.% Ge while in Cu-9.5 at.% Ge parallel bundles of dislocations formed in planar arrays. No extended stacking faults or twins were observed in Cu-9.5 at.% Ge. This was attributed to the decrease in stacking fault energy with increase in germanium solute.

Ogura(47, 48) microtomed aluminum single crystals (99.998% pure) with 50° cutting angle, 0.5 to 1.5 m/sec cutting speed and 100A depth of cut. Differences in shear direction (i.e., chip thickness) were observed to depend on orientation. Plastic deformation from the cutting process appeared to cause the formation of sub-boundaries and twin-bands. Some thin sections of aluminum were thought to have recrystallized due to irradiation caused by the 100kV electron beam.

Black(49) machined copper and aluminum single crystals in various orientations while systematically increasing the depth of cut. The periodicity of the shear fronts was correlated with depth of cut up to about 5 to 10 μm, beyond which the periodicity held constant for a given orientation. The structure was termed shear front-lamella and shown to be the fundamental structure in chip formation(30, 50).

More recently, work has been reported wherein the process has been instrumented to measure cutting forces for a given orientation so that flow stress could be computed(19, 51, 52). These studies verified that the cutting forces as well as the shear angle vary with crystallographic orientation for aluminum and copper single crystals.

Williams and Gane, working with high purity copper(51), found resolved shear stress to be 40% lower in crystals which had a (111) plane oriented close to the shear direction versus having the (111) plane parallel to the cutting direction. The latter orientation also resulted in thinner lamella.

Ramalingam and Hazra(19) machined single crystal 1100 aluminum in a variety of orientations and found that while the shear direction and cutting forces varied with orientation, the shear stress was constant, for the 39 orientations tested. The dynamic shear stress obtained was consistent with polycrystalline values.

Horne(52) constructed a vacuum planing machine to perform orthogonal cuts on (110) single crystals at speeds up to 1 ms^{-1} (197 sfpm) in vacuum down to 10^{-6} torr. Tools were made of T1 steel which had been hardened and tempered to 850 VPN with 40° back rake angle and instrumented with strain gauges to measure horizontal and vertical cutting forces.

Copper and aluminum single crystal workpieces were grown from high purity melt using seed crystals. Specimens were 3mm (0.12 in.) thick, initially 20 mm (0.79 in.) wide and cut by spark erosion into lengths of 80 mm (3.15 in.). All single crystals had a (110) face with differing cutting directions. Copper crystals of <100> <110> and <211> orientations as well as aluminum <100> and <211> crystals were machined at approximately 100 μm depth of cut and speed of 20 mms^{-1} (3.94 sfpm). The setup is shown in Figure 2.11.

In single crystal plane cutting the direction of shear was found to vary with crystallographic direction in both air and vacuum environment, with the air environment consistently yielding a lower shear angle for a given orientation (see Tables 2.3 and 2.4).

The flow stress of aluminum was found to be invariant with respect to crystallographic orientation, consistent with the work of Ramalingam and Hazra(19). Copper on the other hand, exhibited variations in the resolved shear

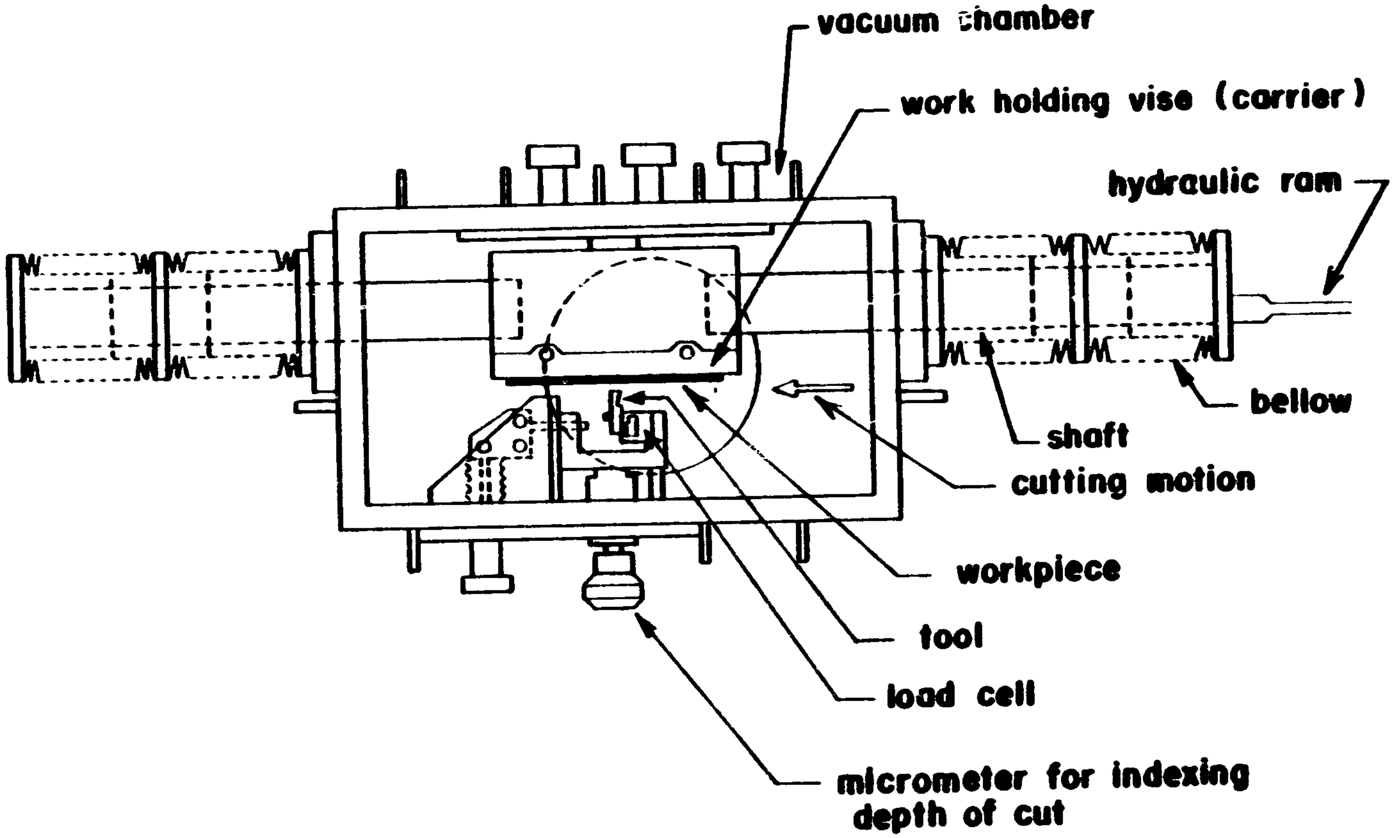

Figure 2.11. Vacuum Planing Machine

Table 2.3. Single Crystal Cutting of Copper

Crystal Orientation	Air			Vacuum		
	Shear Angle	Resolved Shear Stress kgf mm^{-2}	(psi)	Shear Angle	Resolved Shear Stress kgf mm^{-2}	(psi)
Polycrystal	16.6±0.5	30.4±0.7	(43200±1000)	20.5±1.1	30.3±1.1	(43100±1600)
(110)[100]	13.0±0.7	29.4±0.9	(41800±1300)	14.3±0.6	26.2±1.2	(37300±1700)
(100)[100](a)	5.9±0.4	23.4±0.8	(33300±1100)	8.0±0.5	22.5±0.9	(32000±1300)
(110)[110](b)	30.1±2.5	29.2±1.5	(41500±2100)	24.1±1.0	29.0±2.0	(41300±2800)
(110)[211]	22.2±1.3	32.6±0.5	(46400±700)	25.1±2.2	33.9±0.5	(48200±700)
(110)[211]rev	36.3±0.9	26.6±1.1	(37800±1600)	45.2±1.6	22.5±0.4	(32000±600)

Table 2.4. Single Crystal Cutting of Aluminum

Crystal Orientation	Air			Vacuum		
	Shear Angle	Resolved Shear Stress kgf mm^{-2}	(psi)	Shear Angle	Resolved Shear Stress kgf mm^{-2}	(psi)
Polycrystal	9.2±0.3	10.3±0.4	(14700±600)	10.8±0.2	9.5±0.2	(13500±300)
(110)[100]	9.2±0.3	9.7±0.3	(13800±400)	10.4±0.3	9.6±0.2	(13700±300)
(110)[211]	7.3±0.2	10.0±0.4	(14200±600)	7.6±0.2	9.6±0.1	(13700±100)
(110)$[2\bar{1}1]$rev (a)	8.6±0.2	10.0±0.1	(14000±100)	17.7±0.2	8.7±0.3	(12400±400)
(110)$[21\bar{1}]$rev (b)				31.1±1.6	9.5±0.3	(13500±400)

stress with orientation. These findings are consistent with the work of Williams and Gane(41). However, the contrast between the favorable (110) <100> orientation and the unfavorable (110) <211> orientation was not as marked, being on the order of 12%. The flow stress of the polycrystalline copper was determined to have a value intermediate between the favorable and unfavorable orientations and did not take on the highest (unfavorable) resolved shear stress as previously reported(51).

Thus, an apparent contradiction has been confirmed with copper having an orientation dependent shear stress and aluminum being orientation independent. It is suggested that this difference is due to stacking fault energy (SFE) differences between copper and aluminum(42). Aluminum with a high SFE (200 ergs/cm) has narrowly separated partial dislocations which can readily recombine, allowing cross-slip to take palce. This relatively easy movement of dislocations on multiple slip planes could explain the lack of dependence of the flow stress on orientation. Copper has a lower SFE (55 ergs/cm) and therefore widely separated partials which makes cross-slip much more difficult. Therefore, when the slip plane is aligned with the shear plane, slip can occur much more readily with a subsequent drop in shear stress.

In the case of the copper (110) <110> specimens, the shear direction appeared to take on two distinct values, "flipping" two or three times over the 80mm (3.15 in.) length of cut. This behavior was seen in the chip by sharp drastic changes in chip thickness. In the (110) <110> orientation, the resolved shear stress on the $(\bar{1}11)$ and (111) planes should be approximately the same (see Figure 2.12). Therefore, this behavior may be explained due to variations in rake face friction. Increased resistance to chip flow would favor the operation of the lower shear plane. Should the resistance to chip movement subsequently decrease, possibly because the structure resulting from the primary shearing process now makes slip along the rake face crystallographically more favorable, there is a return to the higher plane.

To date, only one experiment has attempted to machine continuously changing crystallographic orientations of a single crystal(53, 54). Single crystal copper discs were sliced (using EDM wire cutter) from a 1¼" bar of (100) oriented copper single crystal. These discs were metallurgically polished and a mounting hole was placed in the center, so they could be orthogonally machined, as shown in Figure 2.13. The plane of the disc was a (100) plane. The discs were x-rayed to determine their crystallographic orientation with respect to a marking line placed on the side. The discs were mounted as shown in Figure 2.14 and orthogonally machined with tools having three different

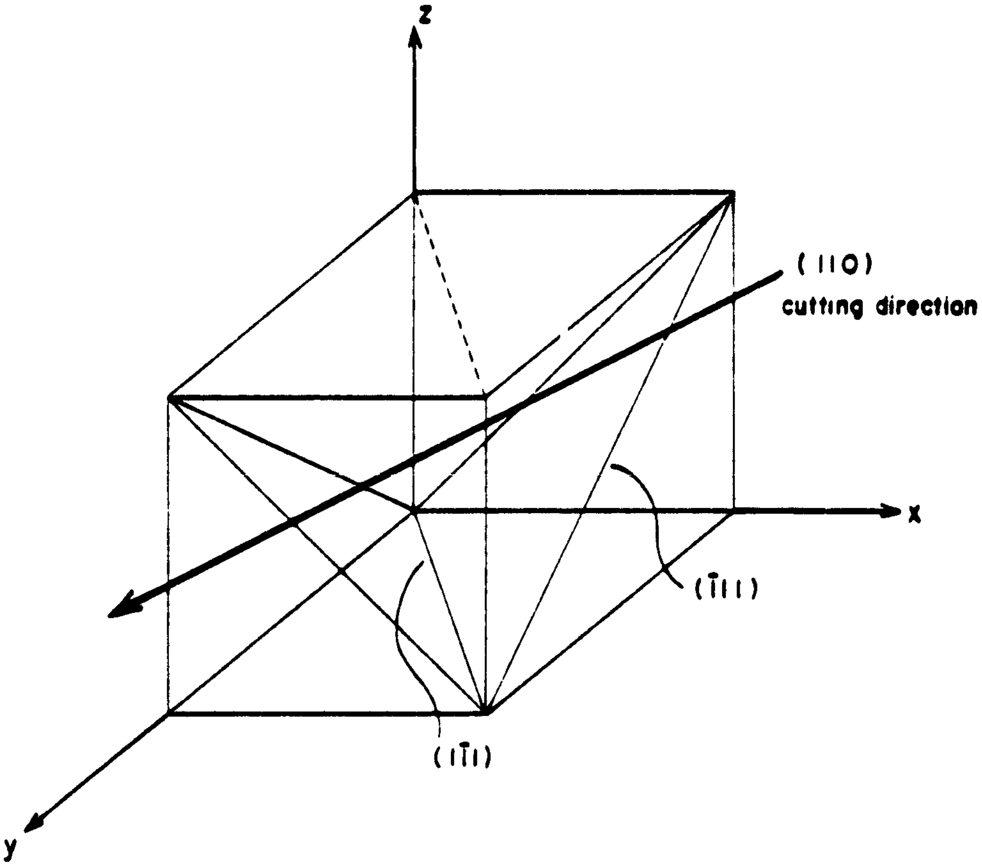

Figure 2.12. Relation of <110> Cutting Direction to (1$\bar{1}$1) and ($\bar{1}$11) Planes for Approximately Equal Resolved Shear Stress

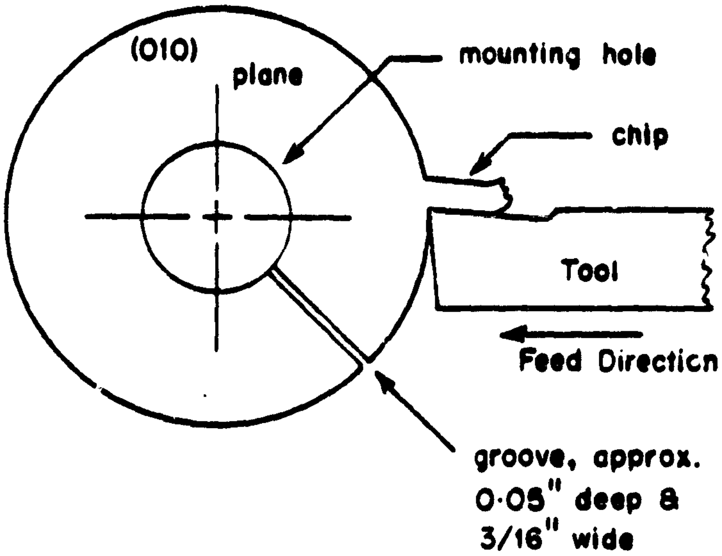

Figure 2.13. Schematic Illustration of Continuously Machined Single Crystal Copper Disk

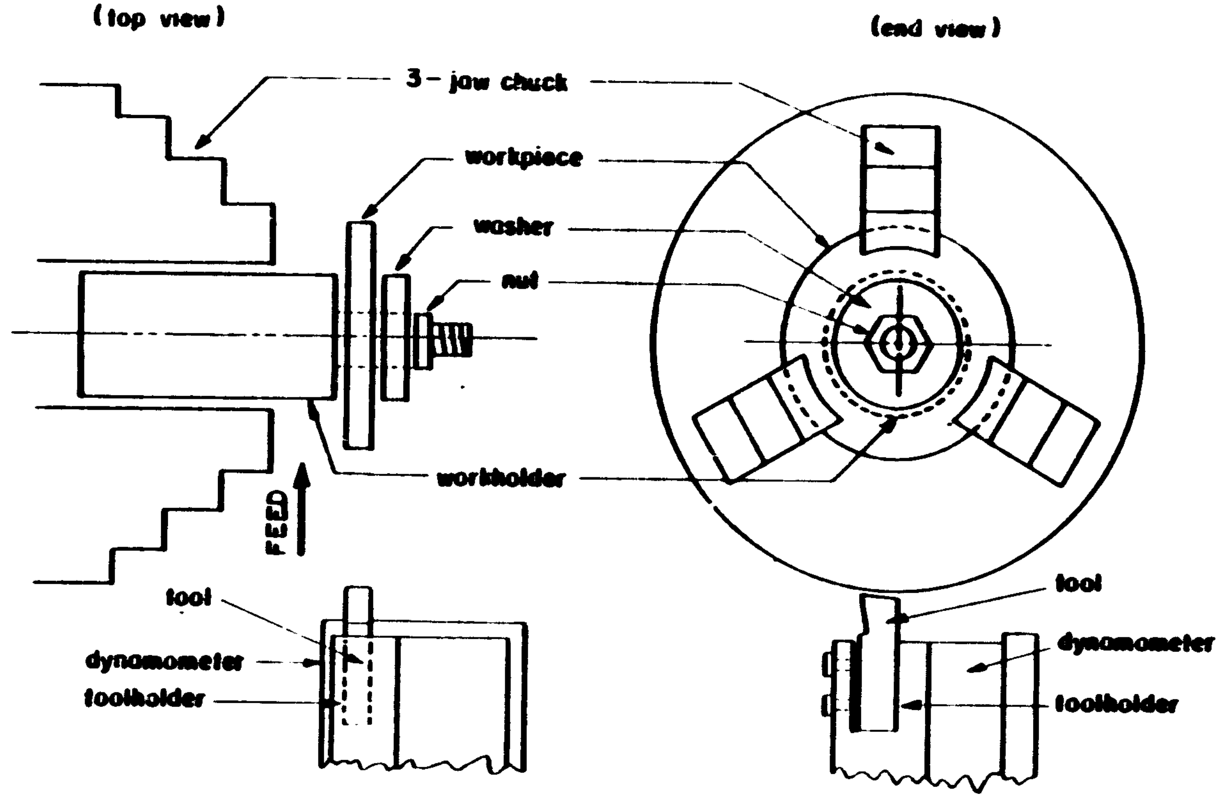

Figure 2.14. Top (Left) and End View of Experimental Setup Used for Orthogonal Machining of Single Crystal Copper Disc

rake angles (back rake angle, $\gamma = 19.3°$, $29.3°$, and $39.6°$). Plunge cutting (tool feed perpendicular to axis of rotation of workpiece) was performed at a depth of cut of .0025 inches per revolution and an rpm of 12. This resulted in the cutting speed decreasing from about 3.75 sfpm at the start to about 2.9 sfpm at the finish. This 25% decrease in speed over the entire duration of the experimental cuts was not observed to have any effect on the results.

In the orthogonal machining of single crystal copper discs, the cutting forces were found to be very sensitive to crystallographic orientation and to vary in a repeatable and consistent manner (see Figures 2.15 to 2.17, Table 2.5). Within one complete revolution of the disc, the force pattern displayed is repeated four times or every one-fourth revolution as the crystallography presented to the tool is repeated.

Shear angle was also found to vary with crystallographic orientation in a repeatable and consistent manner. The pattern is shown in Figure 2.18. Note that the shear angle varies inversely to the cutting force, as expected. As the shear angle increases, the cutting forces decrease and visa versa. Thus, as the disc is continuously reoriented, minimum forces are associated with maximum shear angles.

Table 2.5. Shear Angle and Dynamic Shear Stress Data as a Function of Orientation for Single Crystal Copper With 29.3° Back Rake Angle

Position	Relative Orientation	Shear Angle	Dynamic Shear Stress kgf mm^{-2} (psi)
1	36.61°	12.33°	34.9 (49600)
2	51.86	22.84	40.5 (57600)
3	67.12	17.83	43.0 (61100)
4	91.52	31.37	30.2 (43000)
5	125.08	14.59	39.6 (56400)
6	140.34	18.66	34.2 (48600)
7	155.59	16.05	35.0 (49700)
8	164.74	33.80	29.8 (42400)
9	222.74	14.59	36.1 (51400)
10	234.91	22.84	36.0 (51200)
11	253.22	15.14	33.5 (47700)
12	262.37	25.67	27.3 (38800)
13	311.18	11.96	32.5 (46300)
14	323.39	20.04	35.6 (50600)
15	338.64	14.59	33.0 (46900)

ORIGINAL PAGE IS
OF POOR QUALITY

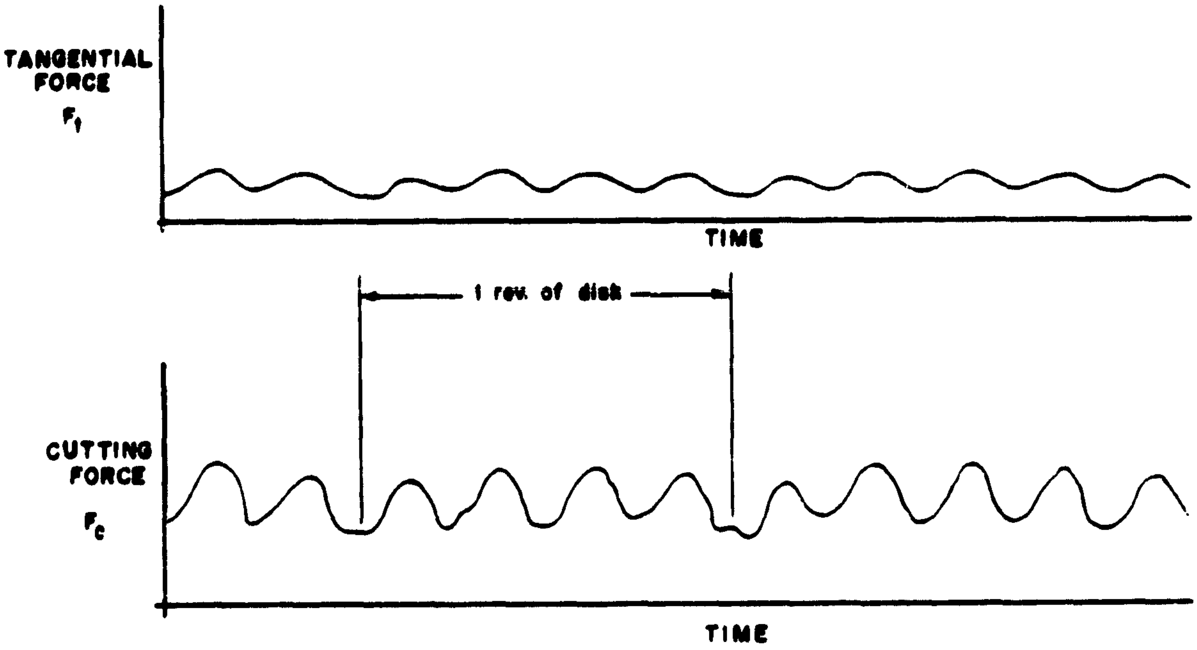

Figure 2.15. Force Traces for the Vertical Cutting Force, F_c and the Horizontal Cutting Force, F_t, for a Tool With a Back Rake Angle of 19.3°, Orthogonal Cutting, Copper Single Crystal Feed = .0025 Inches per Revolution

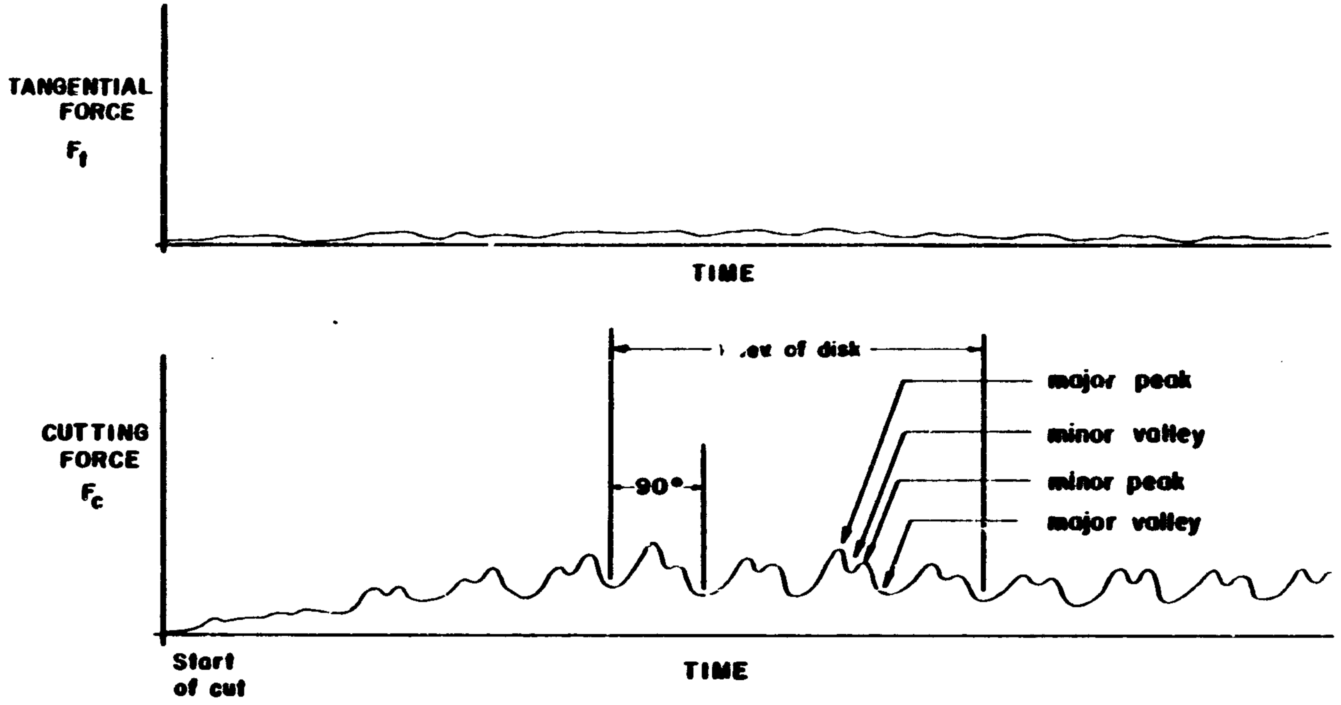

Figure 2.16. Force Traces for the Vertical Cutting Force, F_c, and the Horizontal Cutting Force, F_t, for a Tool With a Back Rake Angle of 29.3°, Orthogonal Cutting, Copper Single Crystal at a Feed of .0025 Inches per Revolution.

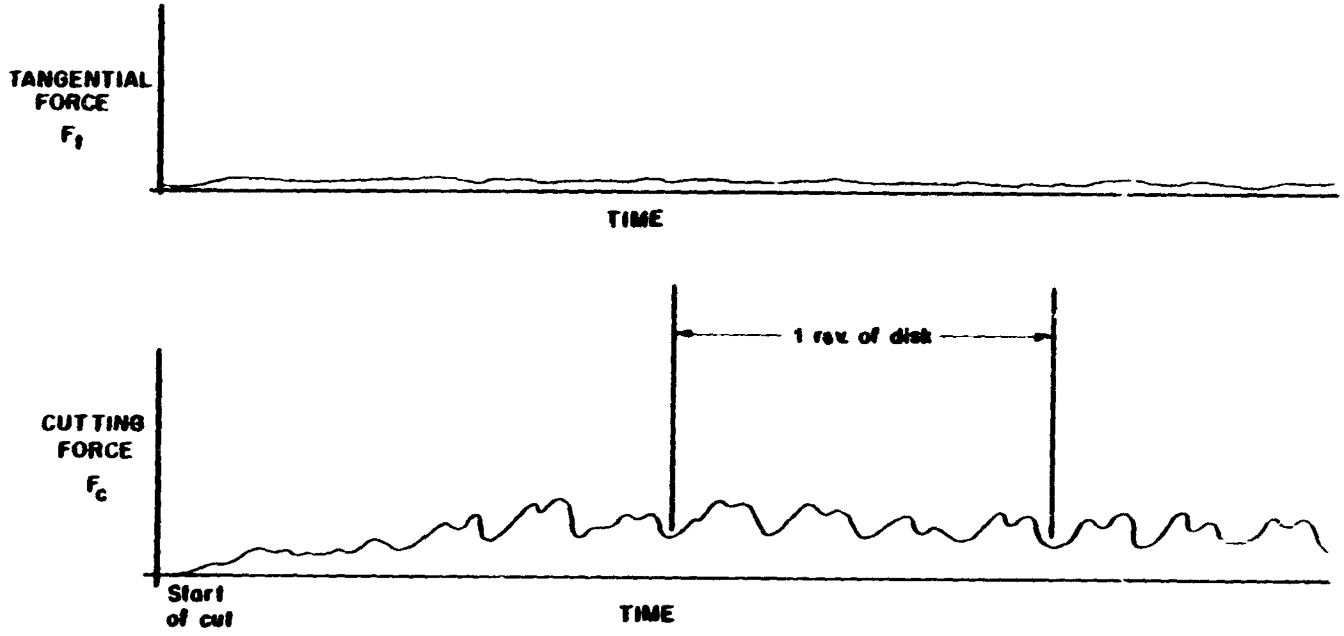

Figure 2.17. Force Traces for the Vertical Cutting Force, F_c, and Horizontal Cutting Force, F_t, for a Tool With a 39.6° Back Rake Angle, Orthogonal Cutting, Copper Single Crystal at Feed = .0025 Inches per Revolution

ORIGINAL PAGE IS
OF POOR QUALITY

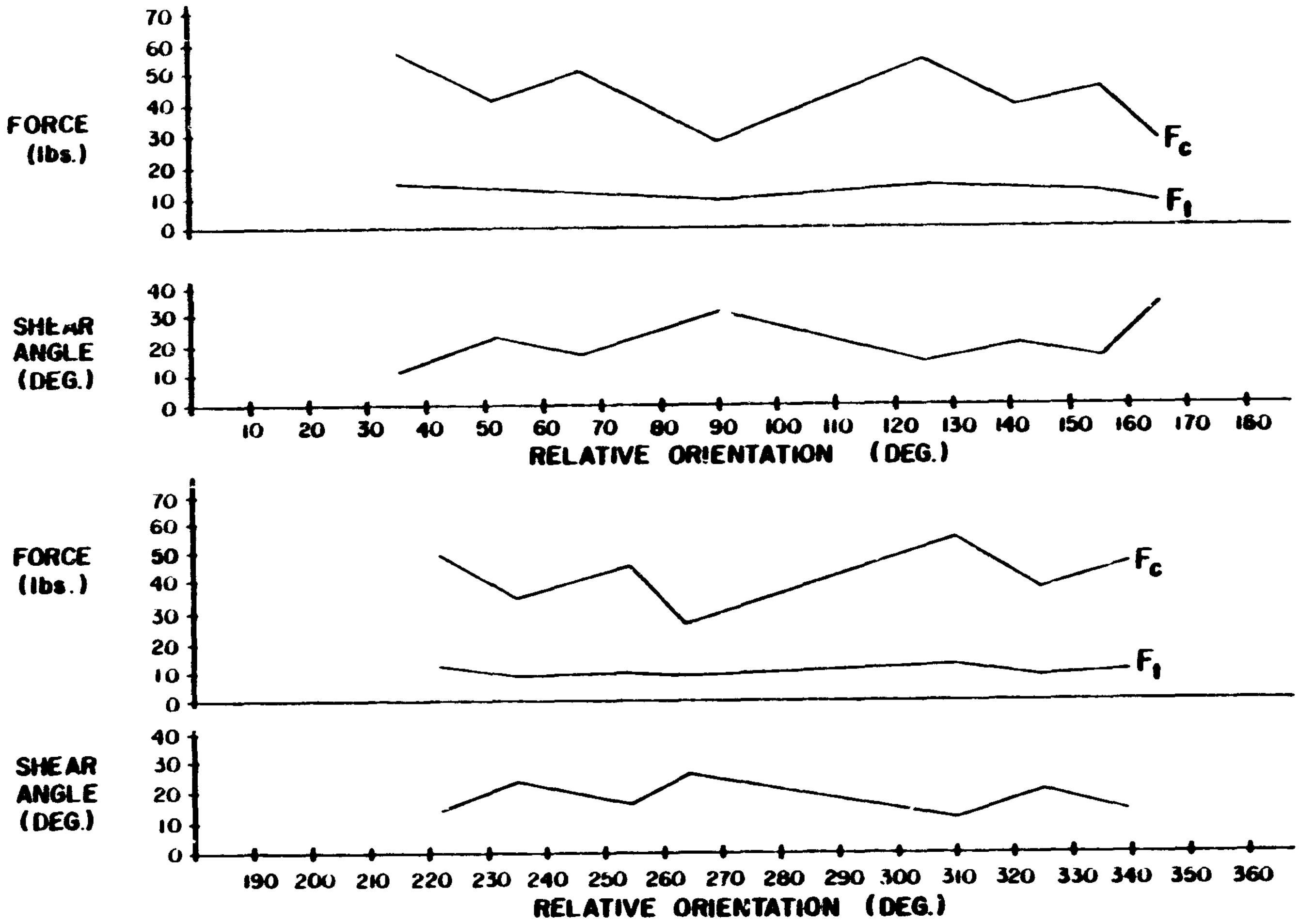

Figure 2.18. Inverse Relationship Between Cutting Forces and Shear Angle in Copper

Careful observation of the cutting force variations in Figures 2.15 to 2.17 shows that for large rake angles, within each quarter revolution, the primary cutting force, F_H, was observed to have a major peak, major valley, as well as a minor peak and valley. Thus within the same 90° rotation, the shear angle starts at a maximum value (major peak), falls to a minor valley, increases to a minor peak and decreases to a minimum value (major valley). The minor peaks tend to fade out as the rake angle is increased so that for small rake angles, only major peaks and valleys are observed and the average force, F_H, is increased. This is an extremely important observation and indicates the sensitivity of the process to material crystallography. It was also observed that as the rake angle increased, the magnitude difference, i.e., the distance from the maximum F_H peak to minimum valley, decreased. This goes along with a general observation in cutting, i.e., cutting forces decrease for larger positive rake angles. However, as the peak to valley distance decreased, minor peaks and valleys appeared. This information is totally new and no doubt would have gone undiscovered had the experiment not been performed in this manner. This could be a reaffirmation of multiple slip systems operating for large back rake angle tools, as observed by Horne(52), who used large rake tools ($\alpha = 40°$), because when the back rake angle was decreased, the minor peaks and valleys tend to fade out (Figure 2.15).

Unfortunately, from the experiments performed, there appears to be no obvious relationship between shear direction and crystallography. The effect of stacking fault energy on shear angle has been examined previously by Black(32) but in polycrystals. It was found that varying the SFE of a material does influence the shear angle but that the effect was not great.

Recent single crystal experiments by Ueda and Iwata(55) on β-brass have been performed in the scanning electron microscope. Experiments were performed on (001) and (101) plates 1 mm thick, 5 mm wide and 20 mm thick with 0° and 20° back rake diamond tools. Several cutting directions (on non-specific Miller Indices) were chosen for each orientation with cutting direction directly influencing chip type (i.e., continuous or discontinuous).

The shear angle, component cutting forces and shear stress were found to be orientation dependent. However, no systematic variations of these quantities were observed. In addition, the coincidence of maximum force and minimum shear angle was clearly observed for (001) β-brass but not in the (101) orientation. The (001) orientation also showed marked periodicity within a period of 90° as has copper(43, 44) with the minimum shear stress occurring with a (010) cutting direction.

Summary of Single Crystal Machining Results

Single crystal machining experiments have added much to our understanding of the chip forming processes. To summarize the more important points:

1. The shear process in chip formation process is intermittent with the shear fronts forming a lamella structure in the chip.
2. Lamellae periodicity is found to decrease with increasing speed and depth of cut and to be material dependent.
3. Shear direction is very sensitive to crystallographic orientation.
4. Cutting forces are sensitive to crystallographic orientation and act in opposition to the shear direction with maximum forces coinciding with minimum shear angle.
5. For fcc metals the most favorable cutting orientation (lowest force) is having the (111) plane inclined approximately parallel to the direction of shear.
6. No simple relationship between shear direction and crystallography was found.
7. The constancy of dynamic shear stress with orientation cannot be proven for all materials and appears to be true only for high Stacking Fault Energy materials.

Introduction to In-Situ Testing

The SEM is currently recognized as a good analytical tool for extracting "static" quantitative information about the structural parameters of solids(56). However, visualization of dynamic events is of vital importance to the proper formulation of mathematical models of those events(57) as well as the qualitative formulation of the event. The SEM, due to its high degree of freedom in specimen translation and its large optical working distance is a prime candidate for performing dynamic (in-situ) experiments with direct observation and recording of deformation processes on T. V. video tapes.

To date in-situ experiments have been performed on a variety of materials ranging from metals to ceramics to textiles. Several modes of deformation have also been investigated - friction and wear(58, 59), tensile testing(60, 61), creep(62), and metal cutting(57, 63, 64, 65, 66). In each case the dynamic, in-situ studies provided more quantitative information as well as greater insights into the mode of deformation being studied.

In-Situ Tensile Testing

Most of the early in-situ stress/strain work was carried out for textiles and textile fibers(56). Dingley (67) designed and constructed a tensile straining stage in which extension and load (up to 10 kg) could simultaneously be measured to facilitate the study of the deformation mechanisms involved. Joy and Newbury(60) later used this same type stage in a Stereoscan Mk.1 fitted with selected area channelling facilities and T. V. scan in order to study the tensile deformation on the specimens strained on the tensile stage. Manual straining or constant strain rate tests could be run with the stage continuously monitored applied load and engineering strain.

The minimum selected probe size was ten microns, the beam divergence $3X10^{-3}$ radians and the beam current $5X10^{-9}$ amps. The minimum selected probe size was capable of being varied by adjusting a third lens in the SEM without changing the beam divergence or probe size. Electropolished or chemically polished specimens of tin, lead, aluminum and copper of minimum 99.9% purity were used. All tests were carried out at variable temperatures with a constant strain rate of $1X10^{-3}$/sec.

At low temperatures the effects of deformation on the microstructure are the appearance of slip bands and the development of surface topography. The slip bands are equally spaced with an initial spacing of about twenty microns which decreases with increasing strain to about five microns. Multiple slip was observed on many grains prior to failure. The selected area channelling pattern technique demonstrated that the pattern contrast decreases with increasing deformation and that the width of the fine lines in the channelling pattern increases with increasing deformation. In tensile deformation at elevated temperatures, all materials tested became more ductile as the grain size decreased and those below ten microns approached superplasticity. The deformation produced similar rotations, but considerable grain boundary sliding was observed in the fine grain materials with the total pattern rotation composed of both grain and lattice rotation. Dynamic recrystallization was also observed during the deformation of large grained samples, but not with small grained samples.

Further tensile tests were performed by Lashmore, et. al.(61) who developed tensile specimens which were particularly well suited for SEM applications in that the specimen can be prepared in the form of a narrow strip with parallel edges and a reasonably uniform thickness. In tension, this type of specimen will exhibit uniform uniaxial stresses. The method of preparation uses a combination of photofabrication and conventional twin jet electropolishing and allows specimen preparation without mechanical preparation which is quite desirable.

The application of tensile loads where the strain rate is quite low and the temperature high by Pond, et. al., (62) has paved the way for in-situ creep studies. The tensile specimens were cut from 99.99% pure polycrystalline aluminum sheet and annealed for two hours at 350°C to ensure the thermal stability of the microstructure. An Al-Mg-Si alloy was also investigated. This in-situ revealed the following:

a. The sliding is intermittent and variable in a particular boundary.

b. The activation energy observed for sliding at times appeared to be that for grain boundary diffusion and in some other measurements corresponds to bulk diffusion.

c. Both solutes and precipitates impede sliding but the solutes impede crystal deformation far more than the sliding process.

d. The grain strain is frequently a function of the sliding strain.

e. Sliding is often accompanied by migration.

f. Low angle grain boundaries do not slide extensively.

These observations were then used to verify a dislocation model for grain boundary behavior during high temperature creep.

In-Situ Friction and Wear Studies

A few dynamic friction and wear studies have been attempted. An apparatus for in-situ friction measurement was developed for use in a SEM 5G electron microscope(58).

A specimen holder was devised which allows rotational movement of the foil specimen in the beam optical axis. Friction tracks can then be produced in well-defined crystallographic direction. The displacement in the tribometer is produced by two inversely synchronized pitch motors. These motors are fixed on the microscope table with a gear reducer and automatic magnetic clutch. For the tribometer, a maximum torque of 40 Nm is given by a shielded galvanometer. The system was also instrumented to measure forces. This sytem requires thick foil (>4500 Å) for reproducible results. Friction tracks were obtained at speeds as slow as 0.3 m/s. It was interesting to observe that the coefficient of friction remained almost zero until evidence of dislocations appeared on the screen.

The subsequent dynamic wear study(59, 60) was performed at the Lewis Research Center in Cleveland, using a pin and disc apparatus (Figure 2.19). A disc specimen is mounted on an adapter to the rotary specimen feed through. The surface of the disc is inclined 70° with respect to the incident beam allowing the disc-pin interface to be viewed from the near side. A variable speed electric motor and gear train provides for disc rotation from 0.001 to 5.0 rpm in either direction (clockwise or counter-clockwise). Thus, either the prow or wake of the rider disc contact can be viewed. Forces can also be monitored on an oscillograph and the deformation video-taped. In this study the

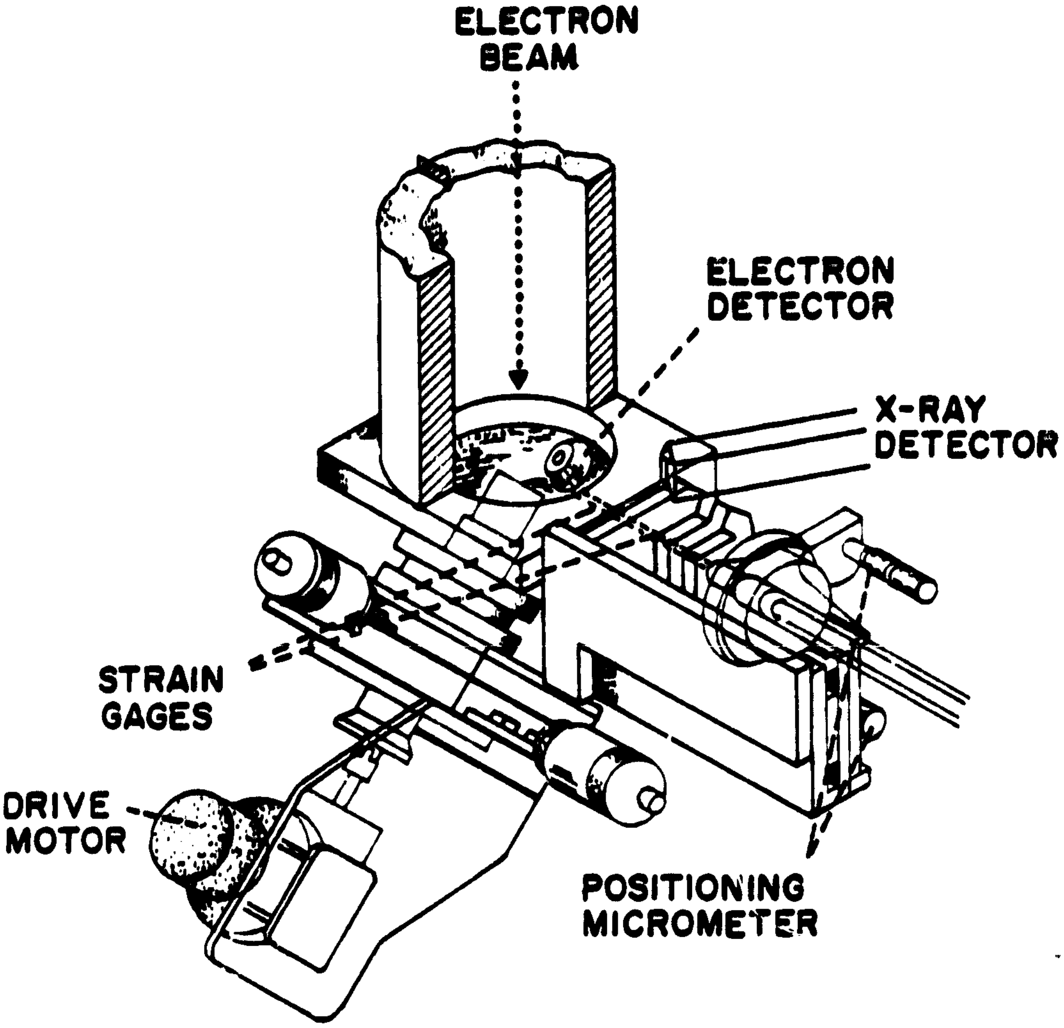

Figure 2.19. Detailed Drawing of Friction Apparatus Mounted on Scanning Electron Microscope

wear behavior of pure tungsten carbide was characterized by both fracture and plastic flow. Visual evidence suggests that during sliding, fracture is initiated by plastic deformation of the tungsten carbide. Cemented carbides were found to wear in a similar fashion but accelerated as the cobalt binder is etched away. The friction and wear of cermets was found to be related to the cementing properties as opposed to changes in its mechanical properties since the worn particles have approximately the same composition as the bulk materials.

In-Situ SEM Metal Cutting

The physical evidence gathered to support the essential elements of the dislocation models like those proposed by Black are post mortem in nature in that the microscopy studies were carried out on the chips following machining. To ascertain the true dynamic nature of cutting, high magnification (up to 10,000x) in-situ cutting in the SEM is required.

The first such study(57, 63, 64) was performed in a JEOL JSM-U3 Scanning Electron Microscope (Figure 2.20). This instrument has a sturdy goniometer which accepts the specimen stage in a dovetail (Figure 2.21). The cutting stage attaches to the stage dovetail. The cutting tool, "T", made of hardened tool steel, is rigidly attached to the stage while the workpiece, "W", mounted on the dovetail

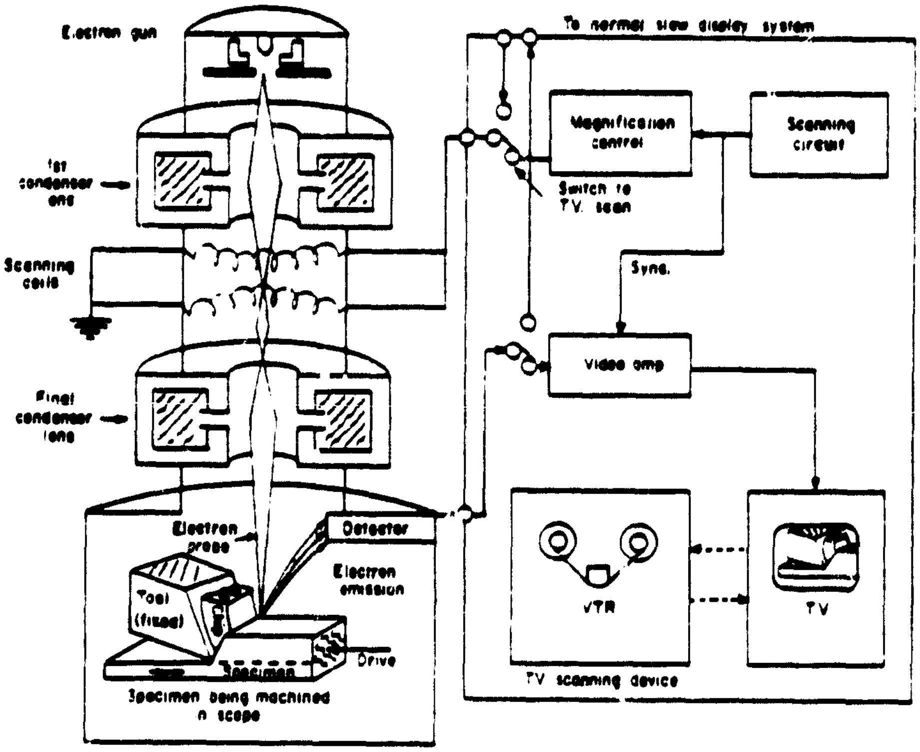

Figure 2.20. Schematic Diagram of Method of Dynamic Recording of the In-Situ Cutting Operation Wherein the Output from the SEM is recorded on a Video Tape Recorder (VTR) as the Cut Proceeds

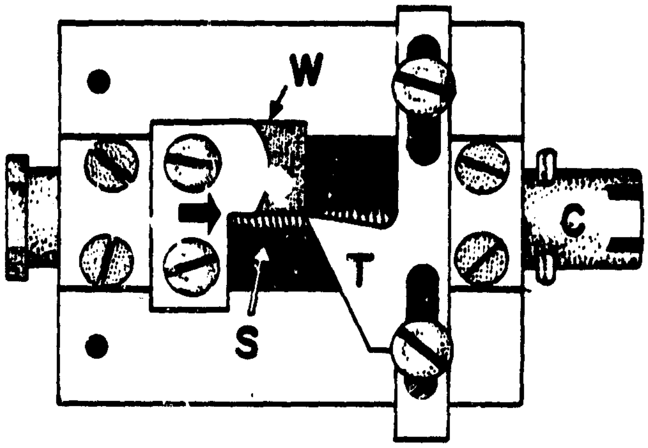

Figure 2.21. Metal Cutting Deformation Stage Used for In-Situ Cutting T = Cutting Tool; W = Workpiece, C = Connector for Drive Rod That Operates Lead Screw (S) Which Advances the Workpiece in the Direction of the Arrows into the Tool, Thereby Producing a Chip

side, is driven against the rigidly fixed tool by an accurately guides screw, "S", with pitch of forty threads per inch. A 0.625 inch length of cut and depths of up to 0.005 inches are possible in a steel specimen of 0.040 inch thickness.

This setup utilizes a motor, "M", which is external to the SEM (Figures 2.22 and 2.23). Translation of the specimen past the tool is done through the specimen pre-evacuation air lock chamber seal, "A", which permits the sue of the large, reversible gear head motor to be mounted externally, eliminating problems of electrical interference within the SEM or vacuum system. The motor is rigidly attached to the external end of the specimen rod, "R", and drives the specimen by a pin and spline arrangement which permits considerable misalignment without binding. Further, the motor is suspended from the column by a spring system, "S_p", in order to minimize seal wear due to the weight of the motor and minimize vibration problems during operation. A video tape recorder was used to record the cutting process at magnifications up to 5000X.

The dynamic observation of the micromorphology demonstrated that post mortem type studies were representative of the cutting process in that the process does occur heterogeneously. It was also found that interrupting the cut by stopping the drive motor causes a gradual cessation of the

ORIGINAL PAGE IS
OF POOR QUALITY

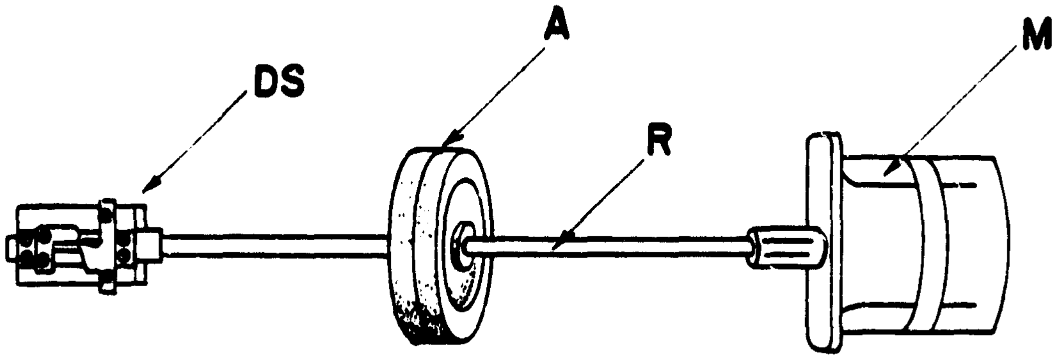

Figure 2.22. Deformation Stage (DS) With Rod (R) Connected to the Motor (M) and the Stage Through the Airlock Seal Plate (A). Motor Reversible so Work Can be Withdrawn From Cut

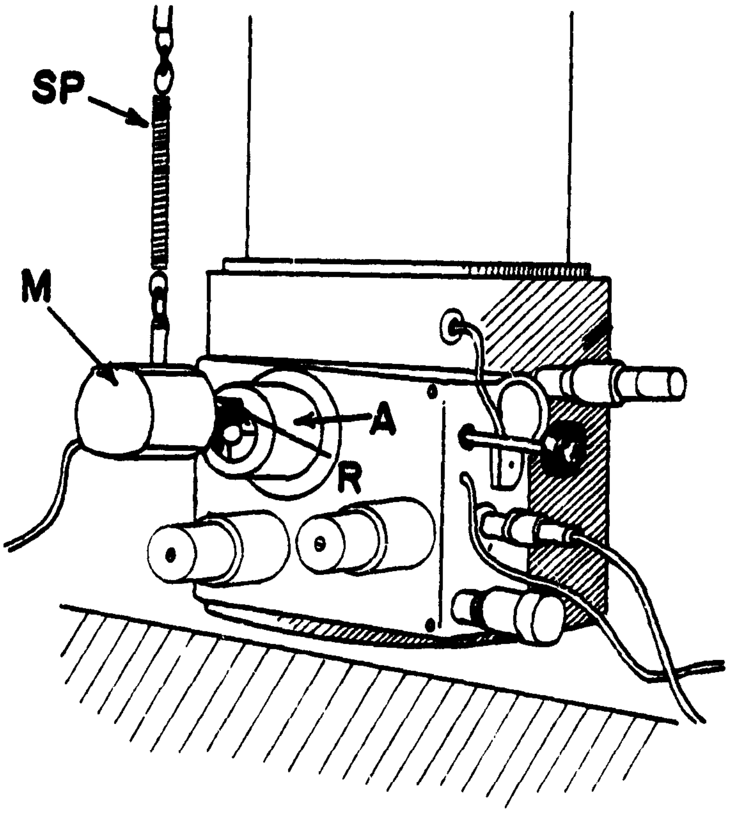

Figure 2.23. Deformation Stage in Place (Not Visible) With Airlock Plate in Place and Motor Suspended by Spring (Sp) from the Column of a JSM-U3 SEM. Because of its Stage and Specimen Insertion Design, the U3 is Uniquely Suited for Deformation Studies of This Nature

heterogeneous plastic flow but the deceleration produced no variations in the morphology. The shear fronts were also found to be formed discretely and discontinuously in time, in that at any instant several may occur, and they do so at regular intervals in the region ahead of the cut. The shear fronts were observed to propagate towards the lateral free surfaces (sides and top of the chi . The expulsion of second phase particles in front of the tool during the cut was interpreted as demonstrating that there is compression deformation ahead of the cut. This first in-situ cutting experiment was thus able to provide insight into the cutting process and was the seed for further work in the area. These observations were all made on the free surfaces, where plane stress conditions exist and can only be assumed to represent internal deformation, where plane strain conditions exist.

Dynamic cutting tests in the SEM were also performed by Iwata and Udea(65, 66). They performed two separate studies - one involving crack nucleation and its propagation in discontinuous chip formation(65) and the other on the effect of lead on the crack behavior of leaded free machining steel(66).

A synchronous motor was mounted which drives a cutting shaft, where the cutting shaft moves the workpiece into the tool to perform an orthogonal cut. In the second study involving the effect of lead on crack behavior, a heater near the plate-like workpiece was capable of generating bulk workpiece temperatures as high as 800° C. A thermocouple was used to continuously monitor workpiece temperature. In addition, a dynamometer has been mated with the cutting shaft to measure forces. Forces were monitored and the chip formation process monitored and recorded on video tape.

In an attempt to study crack nucleation and propagation a 60-40 brass of the composition shown in Table 2.6 was machined at the conditions shown in Table 2.7 and examined dynamically at magnifications of up to 5000X.

Examination of the slip line field in the initial stage of the discontinuous chip formation shows a plastic deformation region around the cutting edge. Also, crack nucleation is observed to occur on the machined surface at a finite distance (a few ten μm) from the cutting edge and the nucleation appears to be associated with the cavitation that occurs around the point where the machined surface separates from the flank of the tool. Iwata and Udea observed that this crack then grows along the shear band as the local effective strain increases ahead of the tool with velocity of propagation increasing. When the crack tip reaches around halfway between the cutting edge and free surface, a high strain concentration occurs in the shear band and propagates rapidly. The cutting force in the experiment continues to increase as the crack propagates until the crack grows to about one-half of the final fracture length where it then decreases to about 40% of the maximum. Furthermore, it was verified that the fracture of a discontinuous chip of the type of brass examined

Table 2.6. Chemical Compositions of the Material (wt%)

Element	Cu	Pb	Fe	Sn	Zn
% Weight	59.65	2.50	0.53	0.41	Bal.

Table 2.7. Cutting Conditions

Tool material:	High speed steel SKH 9
Rake angle:	+11 degrees (test 1), +9 degrees (test 2)
Depth of cut:	88 µm (test 1), 76 µm (test 2)
Width of cut:	1025 µm (test 1), 745 µm (test 2)
Cutting speed:	0.19 mm/min

is caused by a shear-type crack due to an extreme plastic strain concentration.

In the second study, they investigated the dynamic behavior of manganese sulphide (MnS) and MnS-Pb inclusions and the effects of these inclusions on the machining of leaded and unleaded resulfurized steels at various bulk workpiece temperatures. Material specifications are shown in Table 2.8 while the experimental conditions are given in Table 2.9. An analysis of the behavior of various free machining inclusions during the deformation process led to the following conclusions by Iwata and Udea:

a. Both globular MnS and MnS-Pb inclusions show similar behavior, having less deformation than the matrix. As a result, voids form and grow in the plastic deformation zone at all temperatures tested (up to 800° C).

b. Severe hydrostatic compressive stresses and high temperatures in the shear band area cause voids around globular MnS inclusions to reweld.

c. Rewelding is prevented in the case of globular MnS-Pb due to the lead which surrounds the MnS inclusion. This results in crack formation accompanying melted or softened lead in the shear band.

d. The chip-type is transformed from continuous (Type I) to discontinuous (Type II) due to the void formation and its growth around globular inclusions and the reduction or the matrix ductility in the blue brittleness temperature range for the steels (both leaded and non-leaded resulfurized).

e. Non-leaded resulfurized steels show continuous chips with an increase in temperature due to the recovery of matrix ductility and the rewelding of voids.

f. Leaded, resulfurized steel has discontinuous chips due to crack formation and propagation due to MnS-Pb inclusions.

Table 2.8. Chemical Compositions of the Free Machining Steels (wt%)

Work Materials (types of inclusions)	C	Si	Mn	P	S	Pb	ΣN	ΣO
Resulfurized Steel A (globular MnS)	0.070	0.010	1.130	0.046	0.207	-----	0.0017	0.026
Resulfurized Steel B (long ellipsoidal MnS)	0.080	0.008	0.880	0.100	0.259	-----	0.0040	0.024
Leaded Resulfurized Steel C (globular MnS-Pb, MnS, Pb)	0.100	0.010	1.050	0.042	0.240	0.130	0.0025	0.026

Table 2.9. Cutting Test Conditions

Tool Material	High Speed Steel SKH-9
Rake Angle	+20, +24 degrees
Depth of Cut	Variable (0.08-0.25 mm)
Width of Cut	Variable (0.80-1.30 mm)
Cutting Speeds	0.15, 0.20, 1.50 mm/min
Test Temperature	Variable (25-800°C)

g. Long ellipsoidal MnS inclusions and Pb inclusions have less effect on the chip disposability than globular MnS and MnS-Pb inclusions since both types do not accompany any void formation.

Hazra, Caffarelli, and Ramalingam(68) also performed in-situ experiments to determine the behavior of Type I MnS inclusions in free machining steels. Their experiments were performed on AISI 1213 steel (with 0.07% C, 1.09% Mn, 0.01% Si, 0.32% S, 0.08% P, 0.005% Al, and 0.005% N by weight) with globular MnS inclusions possessing elliptical morphology and revealing different results (or at least different interpretations) than Udea and Iwata. Hazra, et. al. also found that manganese sulphide inclusions caused decohesion and cavitation. However, their in-situ results revealed that the MnS particles also undergo cleavage fracture during machining as the shear front passes by. In addition, large local plastic strains may cause the inclusion to be ejected at low speeds. This is due to the nondeforming nature of the MnS particles at room temperature. In addition, this study showed that the fracture of inclusions was not sufficient to account for the superior machinability of resulferized steels and that it is necessary to take their thermal dissipation capabilities into account.

Thus, in-situ SEM cutting experiments provide useful insights available by no other means. It opens up a new way to observe the metal-cutting process.

CHAPTER III

DESIGN CONSIDERATIONS FOR DYNAMIC IN-SITU CUTTING EXPERIMENTS

The scanning electron microscope (SEM) is currently recognized as a good analytical tool for extracting "static" quantitative information on metals. However, visualization of dynamic events is of vital importance to the extraction of qualitative and quantitative information that can be used in the formulation of models of plastic deformation. The SEM, with its high degree of freedom in specimen translation and its large optical working distance, is a prime candidate for performing dynamic, in-situ experiments with direct observation and recording of the deformation process.

Hearle, et. al.(69) lists 15 factors which limit the quality of an SEM image (see Table 3.1). It is instructive to classify these degradation factors into one of four categories as follows:

1. Those which are avoided (or at least minimized) by good SEM design and maintenance.
2. Those which are "unavoidable".
3. Factors dealing with the specimen.
4. Other factors which may be controlled (or minimized) through proper in-situ design.

and are denoted in Table 3.1. The first three categories are common to both static and dynamic viewing in the SEM while category 4 highlights those which differentiate the static experiment from the dynamic experiment. It is here that particular care must be taken to insure a minimum of image degradation. In addition, other physical and mechanical considerations must be incorporated. The totality of these considerations will influence the design of the cutting stage, drive units and chamber seals.

Noise, vibration, and distortion from internal fields are major design considerations for dynamic experiments and impose unique constraints on the entire design philosophy. Smooth-running motors should be selected to minimize noise and vibration. Due to spatial limitations in the chamber of the microscope as well as the possibility of creating internal fields, motor(s) should generally be located external to the chamber with drive shafts running through air-tight seals to power the cutter. To minimize noise and vibration in the stage, motors can be externally mounted on a pedestal connected with universal joints to the stage.

There are additional physical considerations for effective dynamic testing. In instances where the tool moves relative to the workpiece as in turning, the relative motion of tool and workpiece must be interchanged such that the tool is stationary and the workpiece moves past the tool. Otherwise, it would be necessary to refocus the electron beam to follow the cutting action, thereby making it impossible to

Table 3.1. Factors Limiting Quality of an SEM Image(69)

(3)	Spot size + penetration and spread in specimen
(2)	Spherical Aberration
(1)	Distortion, anisotropic distortion
(1)	Astigmatism, anisotropic astigmatism
(2)	Space-charge distortion
(2)	Diffraction
(1)	Departure from symmetry
(1)	Distortion by external fields
(1)	Scan faults
(1)	Other design or operational faults
(4)	Distortion by internal fields, e.g., charging on specimen
(3)	Uncontrolled emission due to specimen charging
(4)	Noise
(4)	Vibration
(3)	Specimen damage

(1)	Avoided by good design and maintenance
(2)	"Unavoidable"
(3)	Specimen related factors
(4)	Important design issues which differentiate static from dynamic experiments

produce high clarity video tapes of the deformation process. For these same reasons it is necessary to design the in-situ cutting apparatus with extreme rigidity and close tolerances in mind. This reduces the inherent elastic deflections and misalignments which can cause the deformation "zone" to move and make the visual record difficult to follow and understand. In a related matter, the cutting apparatus should be tailored to an individual stage and microscope to limit deflections and movement from a sloppy fit.

When the motors are located outside the chamber, it is necessary to run input drive shafts into the chamber to connect to the in-situ device. These shafts as well as connectors for dynamometers and other instrumentation should pass through an air-tight seal and should themselves be air-tight. O-ring seals are generally sufficient for achieving the necssary vacuum.

Low cutting speed is critical for obtaining high clarity video tapes. High speeds are not permissible due to considerations of the scan rate on the SEM. This poses an upper bound on the speed, which is further lowered by our ability to view and comprehend the process dynamically. Experience has shown speeds of 5/16 inch/min. and slower to be acceptable.

While dynamic in-situ cutting experiments require more care and planning than the static, all of the additional problems associated with them are solvable engineering problems.

CHAPTER IV

DESIGN OF EQUIPMENT, INSTRUMENTATION AND TOOLING

Equipment

The in-situ device developed for the orthogonal machining of disks consists of two main subsystems. The first subsystem is a miniature lathe which performs the actual motions necessary for cutting and is mounted inside the SEM chamber for high magnitude viewing. The second subsystem is the drive which has the two gearmotors that power the miniature in-situ lathe mounted on a pedestal external to the microscope. Drive shafts which pass through an air-tight seal connect the two subsystems. The placement of the drive motors outside the microscope is necessitated by internal space limitations, vibrations, and magnetic field interference imposed by motors. In addition, placing the motors internally would require that they be sealed to prevent electrical shorts and this would be extremely difficult.

The primary consideration for the cutting stage is that the tool remains stationary. Thus, the work piece must rotate and feed. In order to do this, the in-situ lathe (shown in Figure 4.1) has an upper half (U) and lower half (L) which, when bolted together, form a track which

C-2

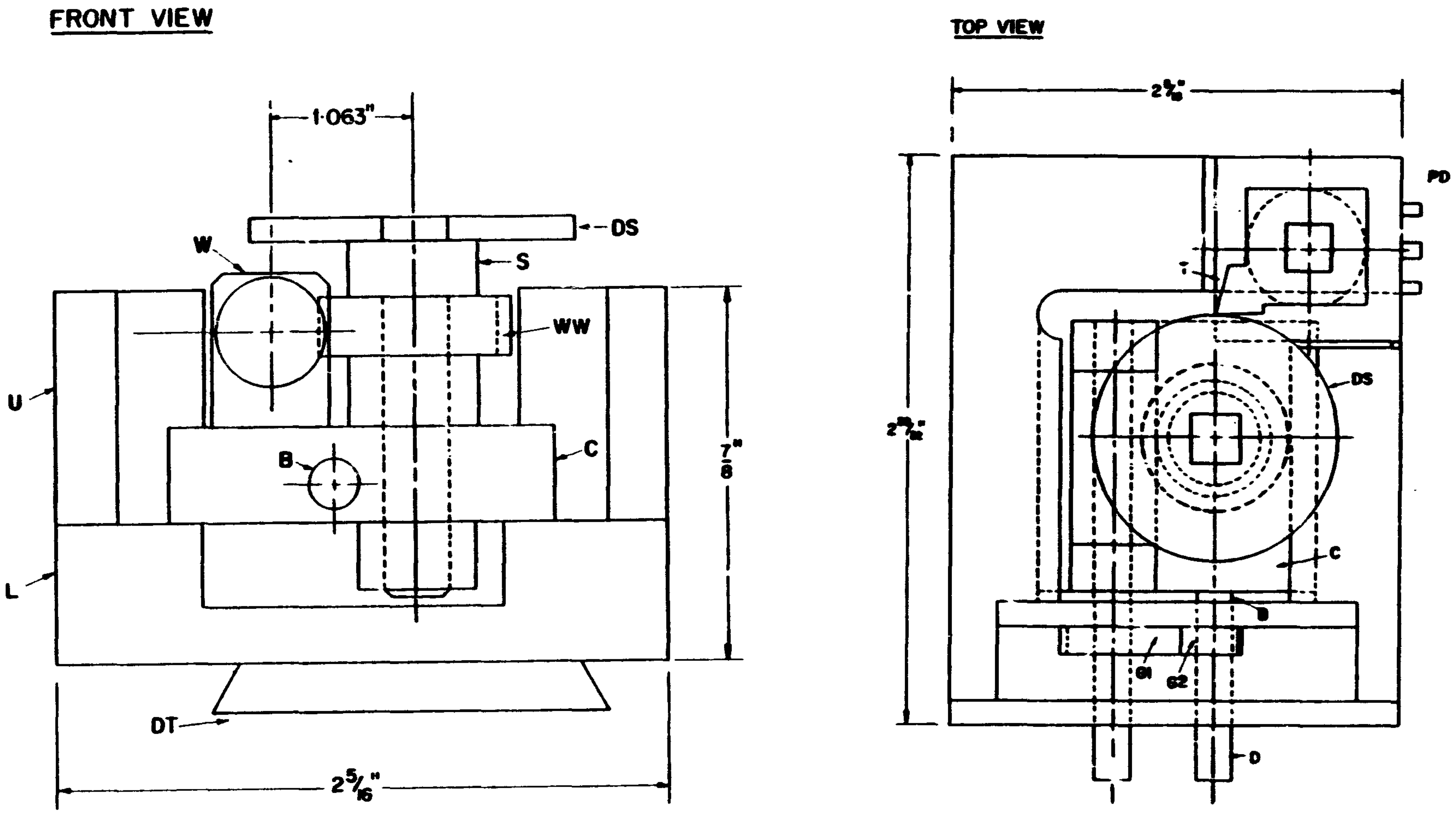

Figure 4.1. In-Situ Lathe

allows a carriage (C) to translate linearly in a highly constrained manner. The carriage is actuated by a 40NF bolt (B) threaded into the undercarriage and supported by the main frame. The bolt is rotated by an incoming driveshaft (D) after being geared down 3:1 by two small brass gears (G1, G2). The disk specimen (DS) is seated and fastens atop a rotating shaft (S) which is supported by a sturdy arm (A). Rotations of the specimen is accomplished by attachment of a drive shaft to the worm (W) and worm wheel (WW) combination which rotates the shaft. In addition, the top of the shaft has been milled square to mate with specimens that have been broached with a square hole. Thus, there is no slippage of the disk and it is capable of translation as well as rotation with respect to the cutting tool (T).

All cutting tools are made from an air hardenable low carbon steel and sit atop a piezoelectric dynamometer (PD) which is rigidly attached to the lower base. The entire assembly is able to fit into the standard JEOL JSM-U3 stage with the dovetail (DT) on the in-situ lathe corresponding directly to that on a standard specimen holder. Figure 4.2 shows the in-situ lathe assembled and installed in the main stage of the SEM.

The second subsystem consists of the means of powering and controlling the inputs to the in-situ lathe (see Figure 4.3). Both motors are 1/15 hp Daytons capable of 12 rpm. The rotational motor (RM) connects directly to

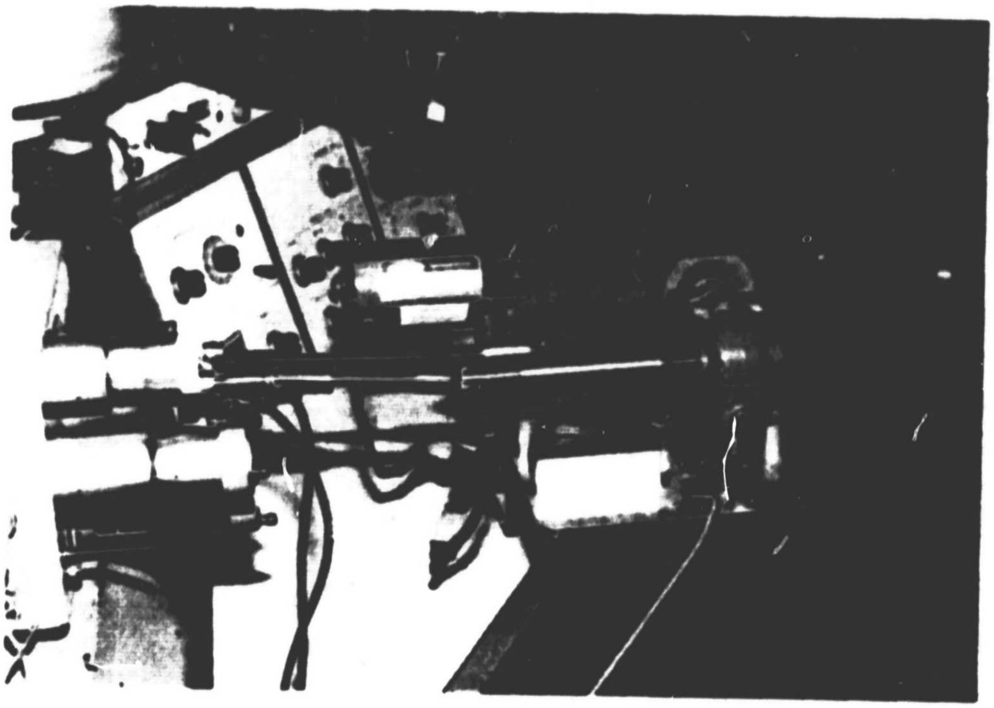

Figure 4.2. In-Situ Lathe Installed in SEM Stage

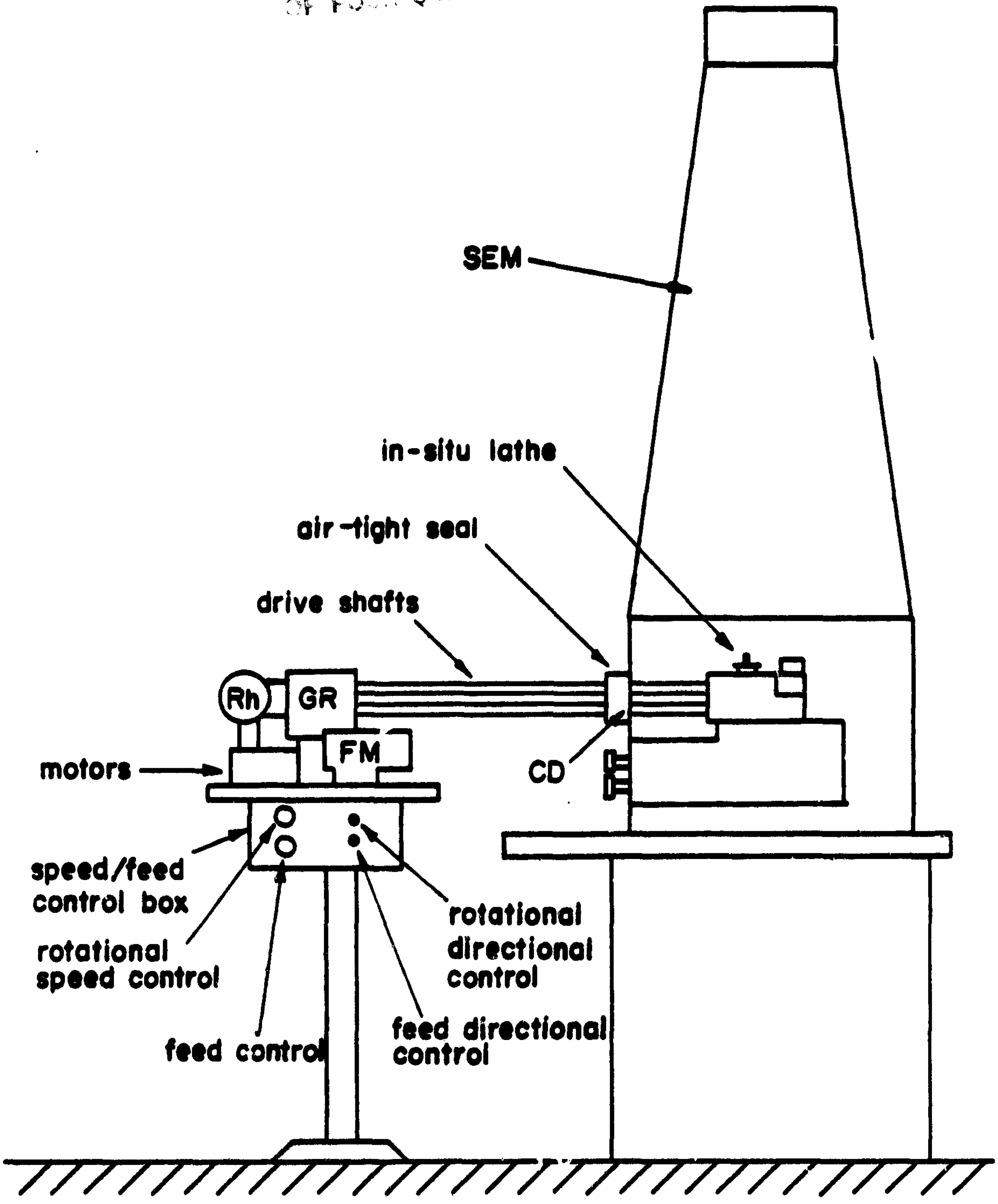

Figure 4.3. Set-up for In-Situ Machining

the cutting device while the feed motor (FM) is geared down by 5:1 through a Dayton gear reducer (GR). A control box regulates the speed and direction of the motors allowing for varied cutting speeds and depths of cut.

The two subsystems are connected by shafts which run through air-tight seals (S) which are built into the specimen exchange chamber door (CD) as shown in Figure 4.3. The entire assembly including motors and shafts are supported on a pedestal outside the microscope as shown in Figures 4.3 and 4.4. This design allows one person to control both the cutting action and the microscope.

Materials

Specimens in the form of disks were sliced from cylinders of high purity (99.9995%) (001) axis zone refined single crystals using an EDM wire cutter. Single crystal copper specimens were 1¼ inches in diameter with thicknesses ranging from .080 inches to .105 inches while the aluminum has 1 inch diameter with thicknesses from .050 inch to .065 inch.

Before cutting, the surface of the specimen exposed to the SEM high energy beam was mechanically polished on a Struers Autopolishing machine using the following procedure:

1. 240 grit paper
2. 320 grit paper
3. 400 grit paper

ORIGINAL PAGE IS
OF POOR QUALITY

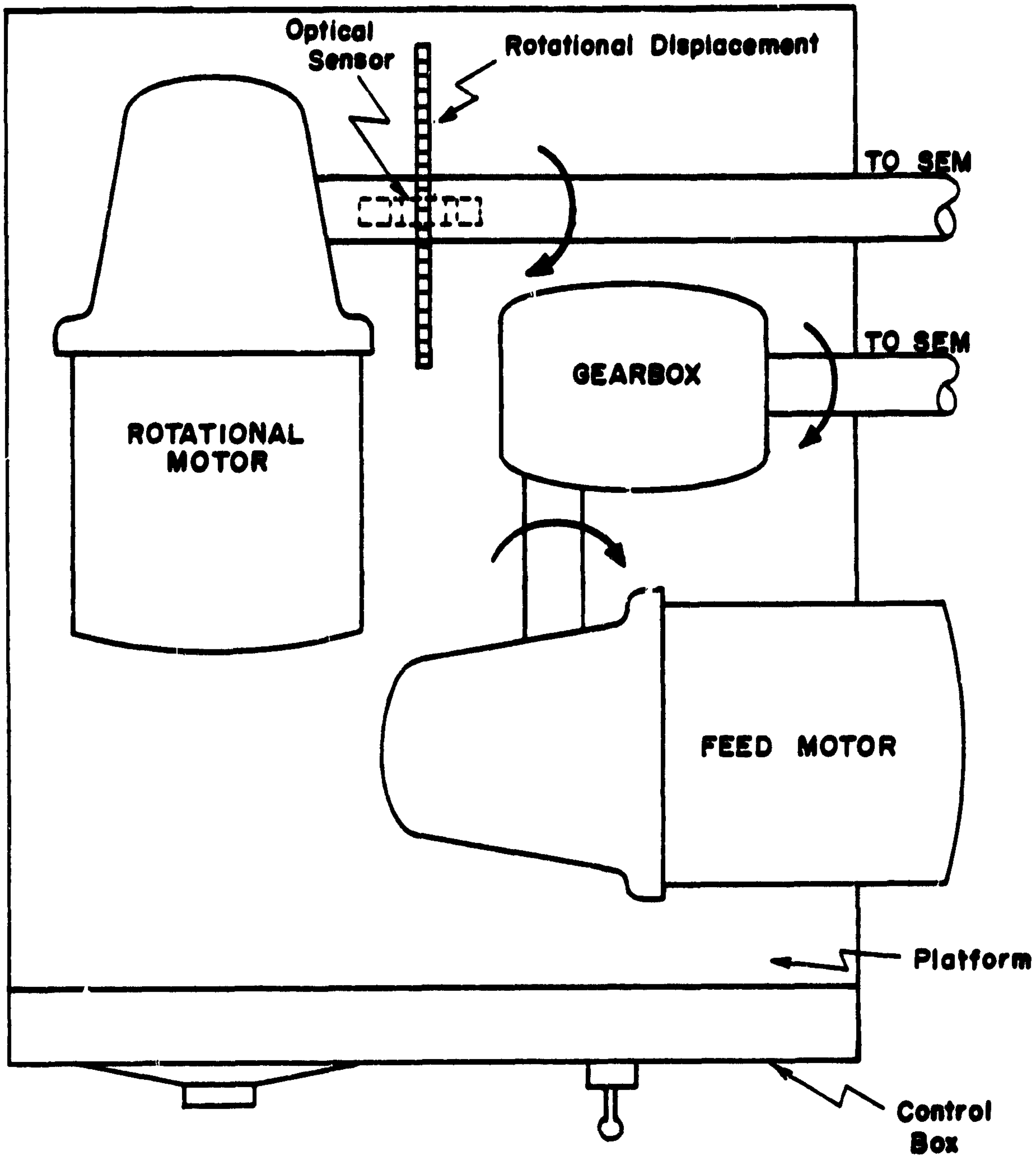

Figure 4.4. Top View of In-Situ Platform

4. 600 grit paper
5. 3 micro paste with polishing cloth
6. 1 micron paste with polishing cloth
7. 0.05 micron Alumina powder with micro cloth

thus creating a virtually scratch-free mirror finish.

After polishing, Laue Back Reflection methods were used to determine the crystallographic orientation of each specimen. Exposure for 13 minutes to 30 KV, and 20 Mamp was required for each exposure and orientation determined using a Greninger graph and 20 interval Wulff Net.

In addition, the workpiece is drilled and broached (½ inch square) for mounting on a square spindle in order to eliminate any slippage as shown in Figure 4.5.

In addition, experiments were performed on 1½ inch diameter specimens of polycrystaline TPE copper, which was rolled from 0.125 inch to 0.065 inches to achieve a hardness of 50 HRC and thus reduce sidespread. Disks of similar size were made of 2024 T351 aluminum for the measurement of shear velocity. All polycrystalline specimens received the same polish as the single crystals.

Instrumentation

The overall objective of this system is to enable one to observe and measure the cutting process dynamically; to wit:

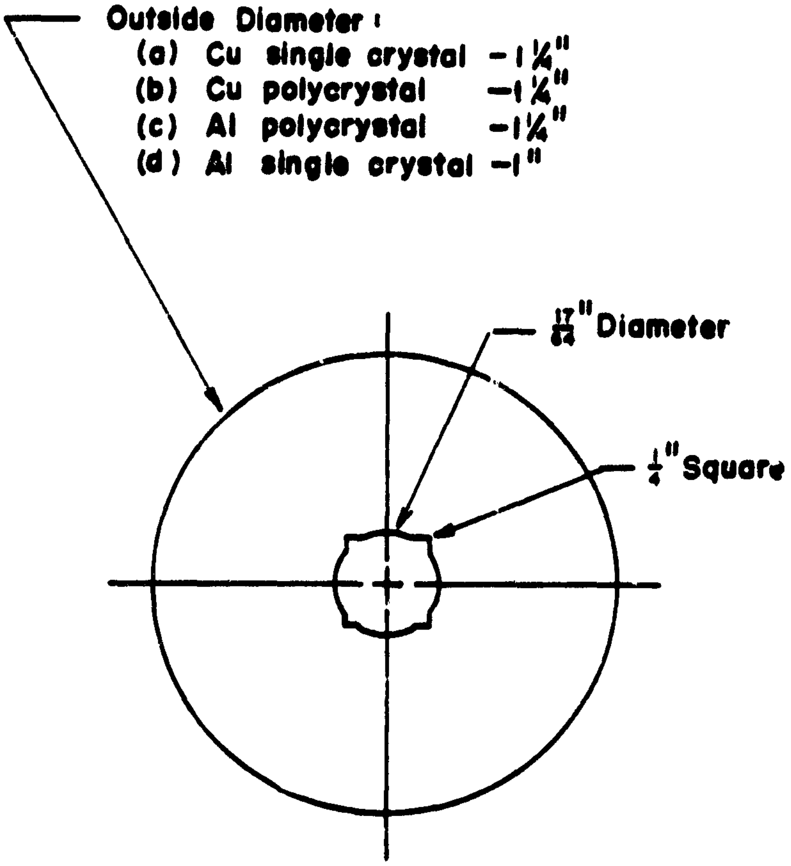

Figure 4.5. Specimen Geometry for In-Situ Cutting Experiments

1. High magnification and resolution of the shear and compression deformation for observing the shear angle of the process is absolutely necessary.
2. Two orthogonal force components should be monitored at all times.
3. The orientation (rotational position of the disk with respect to the tool tip) should be known at all times.
4. There should be a permanent record of the deformation process, cutting forces and orientation (criteria 1, 2, 3).
5. The permanent record should be synchronized for items 1 to 3.
6. The force and orientation should be of sufficient resolution and updated frequently to accurately reflect rapid changes in the cutting process.

The instrumentation designed and constructed reflects all of these considerations and is shown schematically in Figure 4.6.

High magnification and resolution of the cutting process is achieved by performing the cut in a scanning electron microscope (SEM). A Japanese Electron Optical Microscope (JEOL), type JSM U3 is used. It has built into it an image collection system which sends a video signal (V), to a timer (T), which numbers every frame (60 per second) and collects the video signal. Cutting forces are sensed

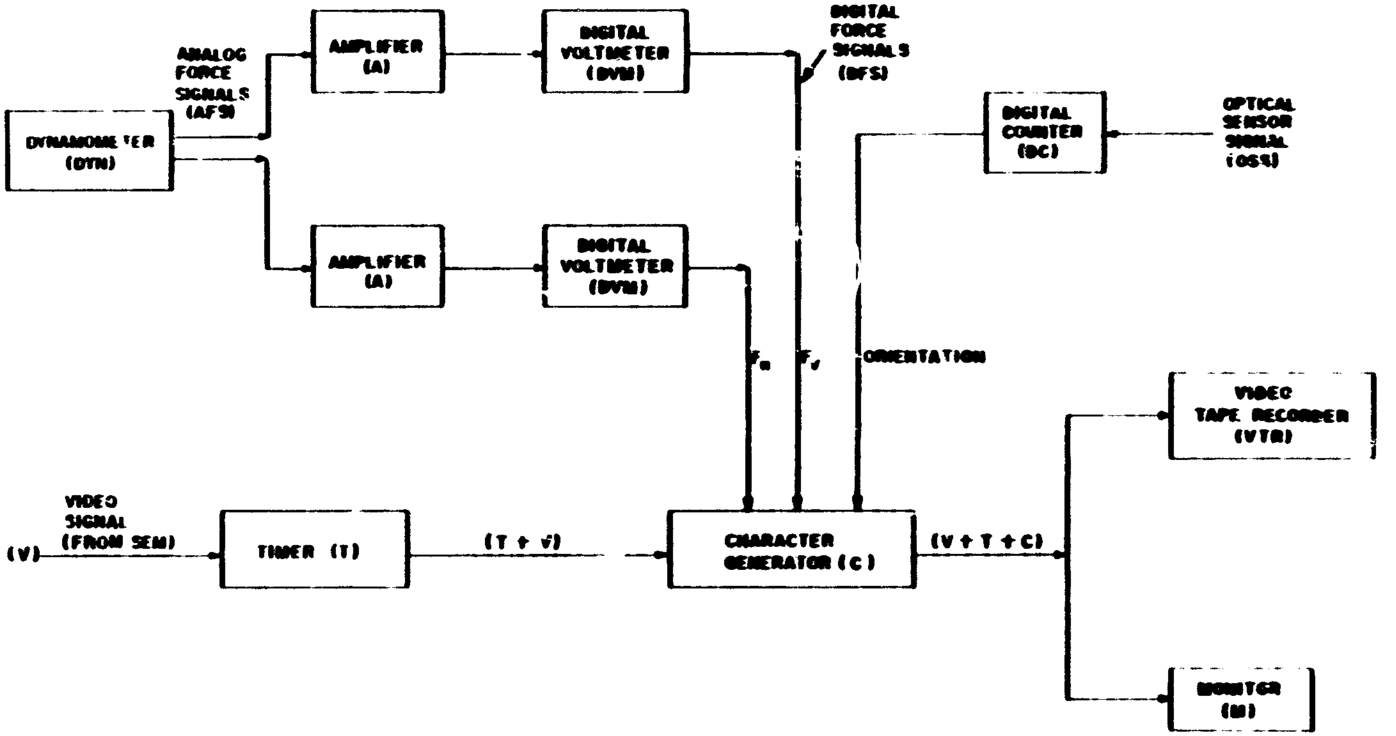

Figure 4.6. Overview of Instrumentation for In-Situ Machining

by use of a Kistler Type 9251 Piezoelectric dynamometer (DYN) which sends analog force signals (AFS) to be amplified (A) and converted to a digital signal (DFS) by a digital voltmeter (DVM). This same procedure is used for both orthogonal force signals.

The position of the disk is monitored by using an optical sensor to measure the position of the drive shaft after it leaves the gearmotor external to the microscope. A ¼ inch slot is milled every 5° around a 4 inch diameter disk (see Figure 4.7). Every time the slot coincides with the H13B optical sensor, one degree is added to the digital counter (DC) since the worm-worm wheel is geared down by a 5:1 ratio. Thus, the specimen rotates once for every five revolutions by the drive shaft.

This signal for the orientation as well as the digital force signals are input into a character generator (C). Here they are synchronized and combined with the timer and video signal (T+V). The force and positional information is updated every 1/20 of a second. The combined signal (V+T+C) is in turn fed into a TV monitor for observation as well as a video tape recorder for a hard copy. Thus, the permanent record contains the visual record of the deformation from which the shear angle can be measured as well as superimposed digital measurement of cutting forces (two), orientation of specimen, time (actually a frame counter) and a test designation number such that a frame by

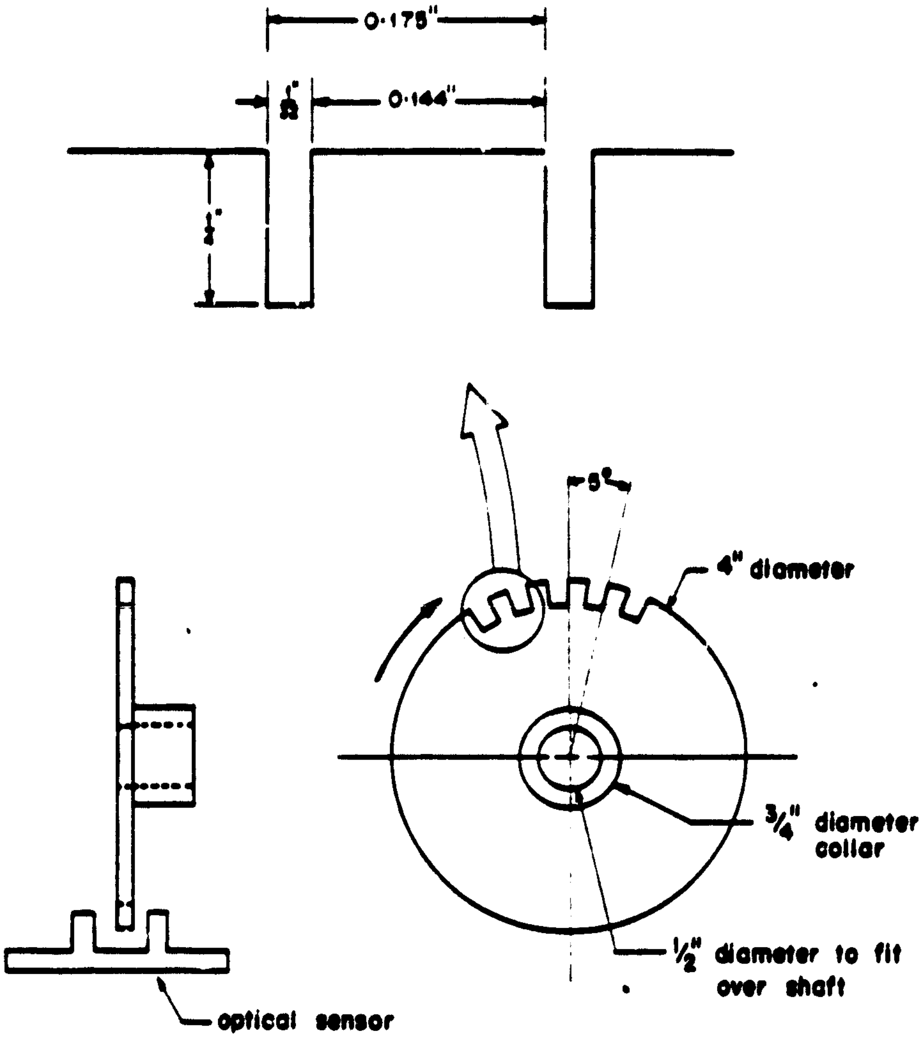

Figure 4.7. Position Measurement Device

frame analysis can be performed and quantitative as well as qualitative information extracted as shown in Figure 4.8.

Tooling

All cutting tools were made from O1 oil hardening steel. Square holes were broached (see Figure 4.9) to allow the tools to be rigidly mounted on a square post atop the piezoelectric dynamometer. Tool angles (back rake and clearance angles) were then rough milled. The tools with prescribed geometry were heated to approximately 1490°F and rapid quenched in oil. Tempering at 400°F followed after which the rake and clearance faces of the tool were surface ground. This procedure produced tools of precise geometry and approximately 62 HRC. The rake face was then honed and hand polished to a mirror finish of 1 micron. Care was also taken to insure a very sharp cutting edge for all experiments.

To insure orthogonal cutting conditions, the tip of the tool was maintained along the centerline of the disk specimen as shown in Figure 4.10 for all tool geometries used in the cutting experiments. Table 4.1 lists these geometries.

In addition to the standard orthogonal tools, restricted contact tools were made with 20 degree back rake angle. The method of restricting the contact length is illustrated in Figure 4.9

ORIGINAL PAGE IS
OF POOR QUALITY

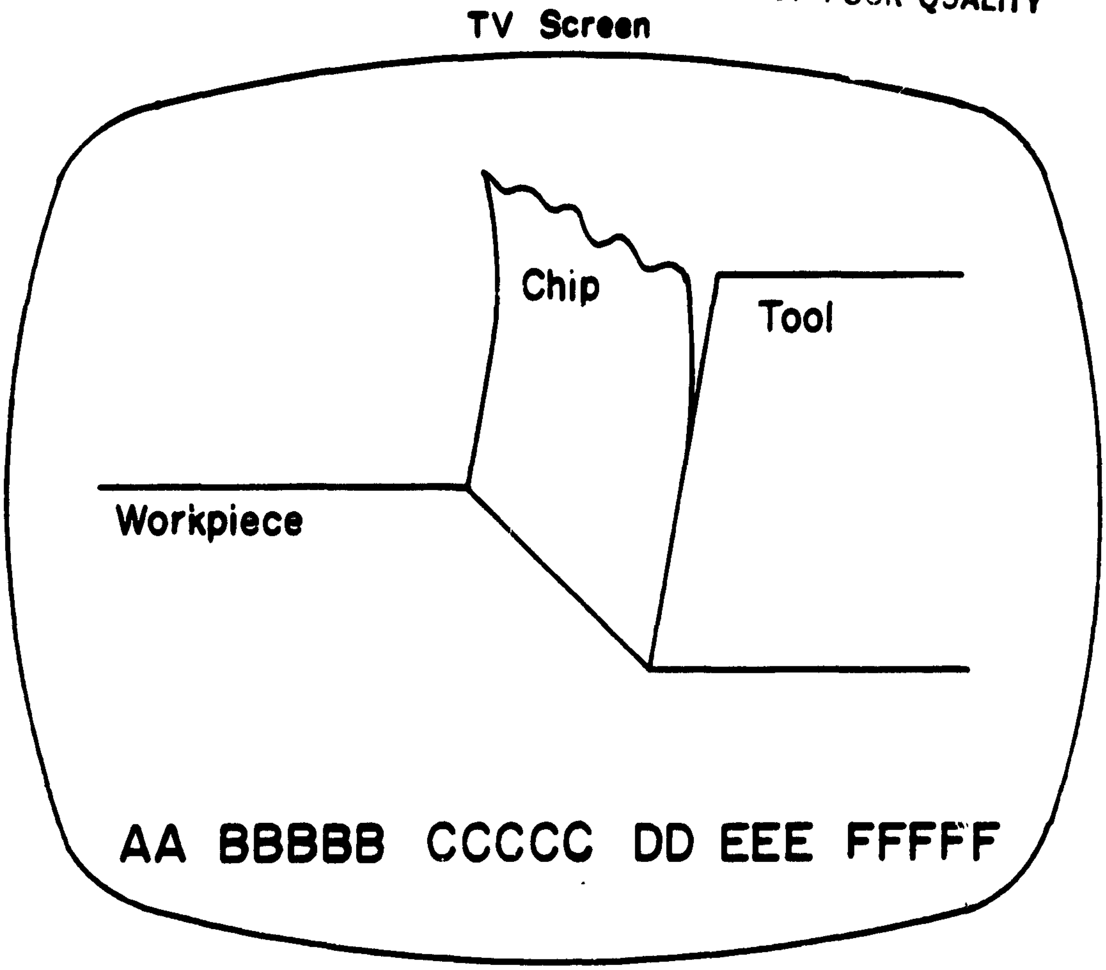

Figure 4.8. Information From a Single Video Frame as Displayed on TV Monitor; AA: Test Number, BBBBB: Horizontal Force, CCCCC: Vertical Force, DD: Number of Disk Revolutions, EEE: Disk Orientation Within Revolution DD, FFFFF: Clock. See Figures 7.4 through 7.9 for Photographs of Actual Cutting Experiments

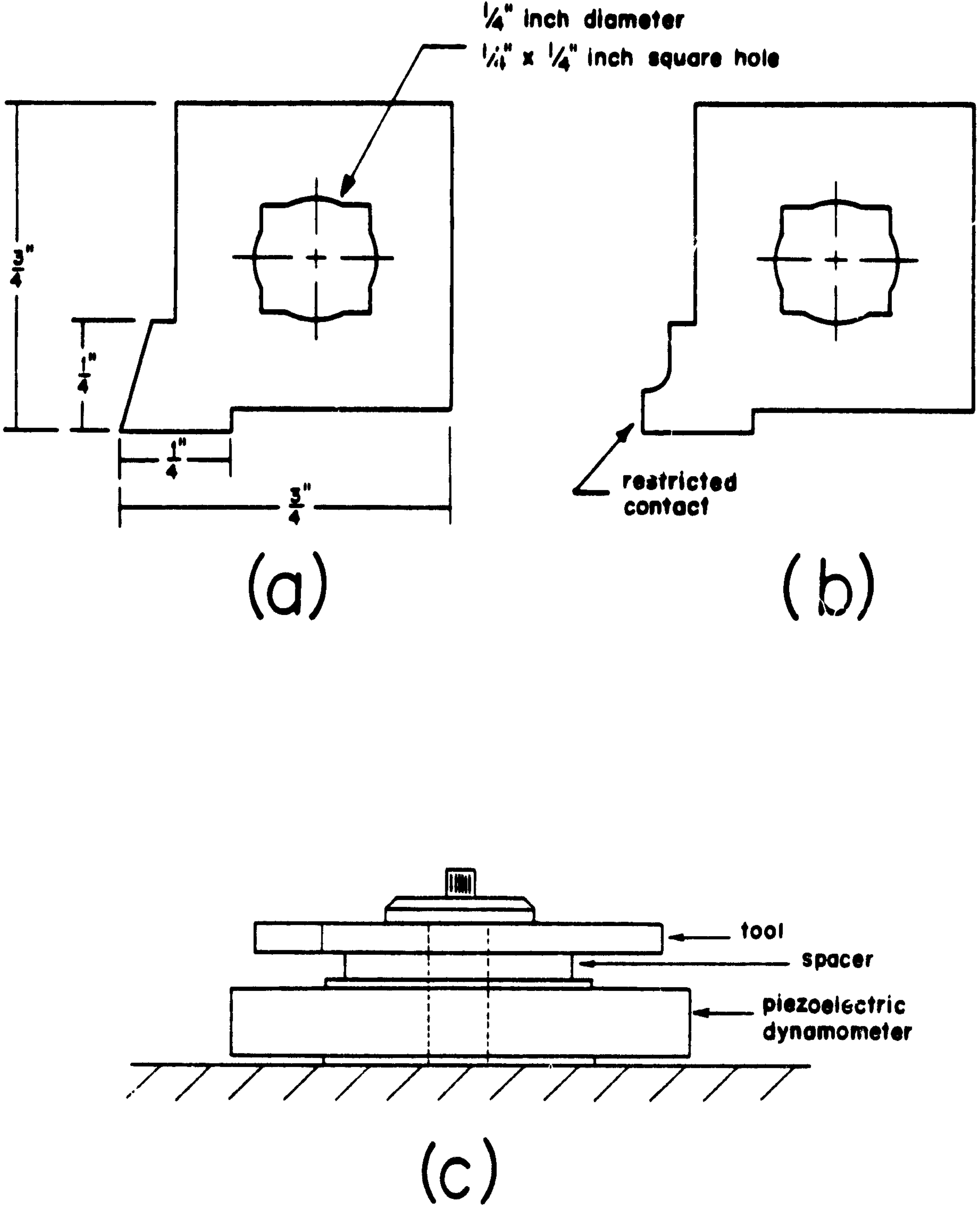

Figure 4.9. In-Situ Tooling

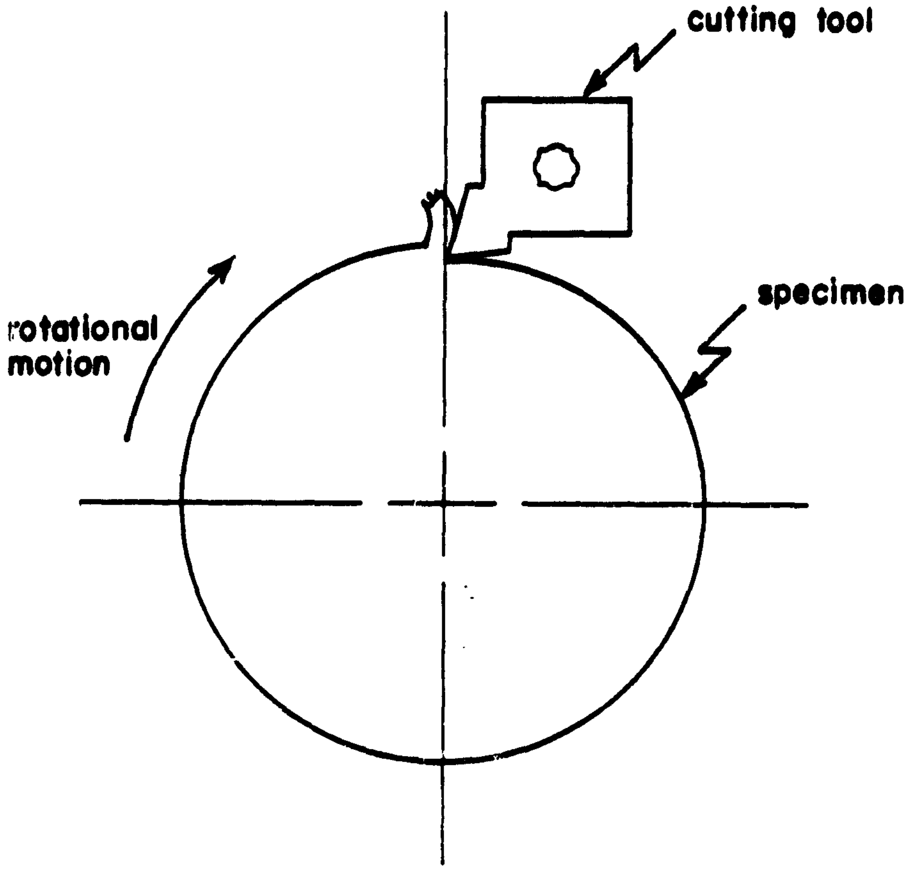

Figure 4.10. Alignment of Tool and Workpiece for Orthogonal Conditions

Table 4.1. In-situ Cutting Tool Geometries

TOOL	BACK RAKE	CLEARANCE	CONTACT LENGTH
1	0°	6°	unrestricted
2	10	6	"
3	20	6	"
4	20	6	0.022 in.
5	20	6	0.011 in.
6	40	4	unrestricted
7	50	4	"

CHAPTER V

ENERGY MODEL FOR METAL CUTTING

The Nature of the Tool Chip Contact

As discussed in the Literature Review (Chapter II), a variety of mechanics models have been developed for shear angle prediction. It can be seen from Figure 2.5 that these approaches typically are not accurate for a wide range of materials and conditions. These failings are due to a variety of reasons including erroneous assumptions with regard to secondary shearing and friction on the rake face and its distribution over the contact length.

Typically, the distribution of stresses on the rake face is assumed to be uniform for both normal and shear stresses, as shown in Figure 5.1. This infers that sliding friction occurs over the entire tool-chip contact length. Recent studies(70, 71) have verified that the contact region on the tool consists of two zones (see Figure 5.2). One region (labelled I) is a zone located immediately above the cutting edge where seizure (or "full sticking friction") is present. Seizure has been defined by Wright, et. al. (70) as a solid phase weld between the primary atomic bonds of the tool and the atomically clean surface of the workpiece. The last layer of material in the chip is therefore

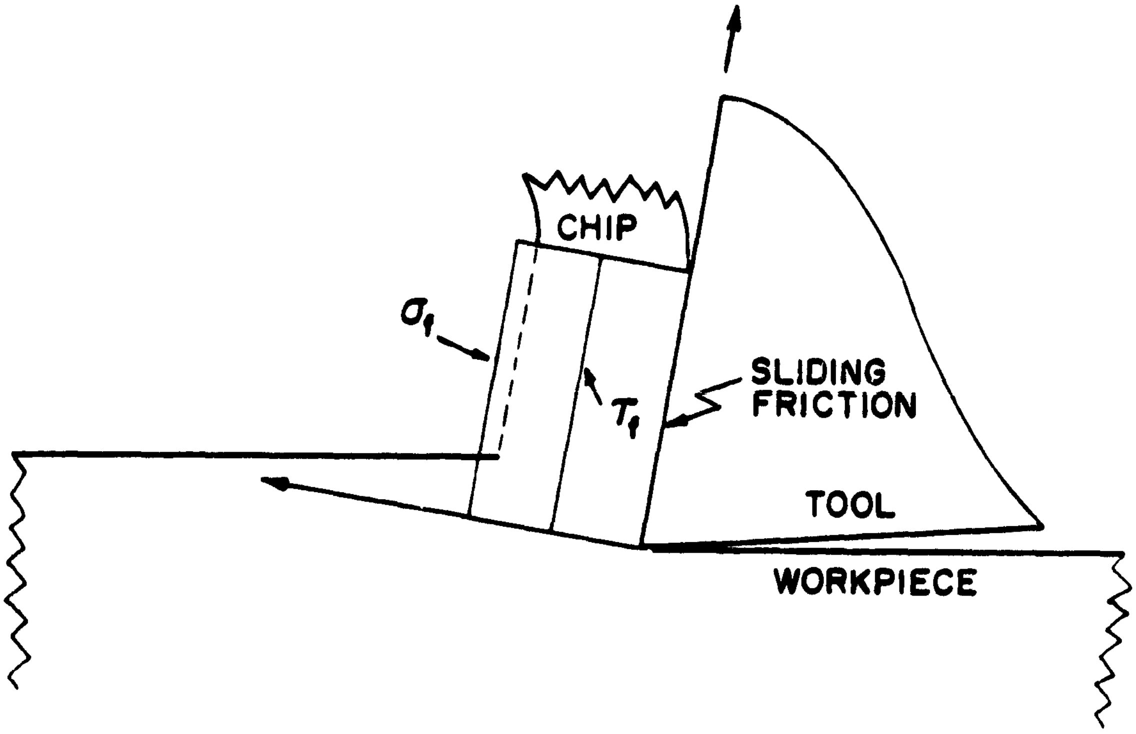

Figure 5.1. Uniform Stresses Developed on the Rake Face During Cutting

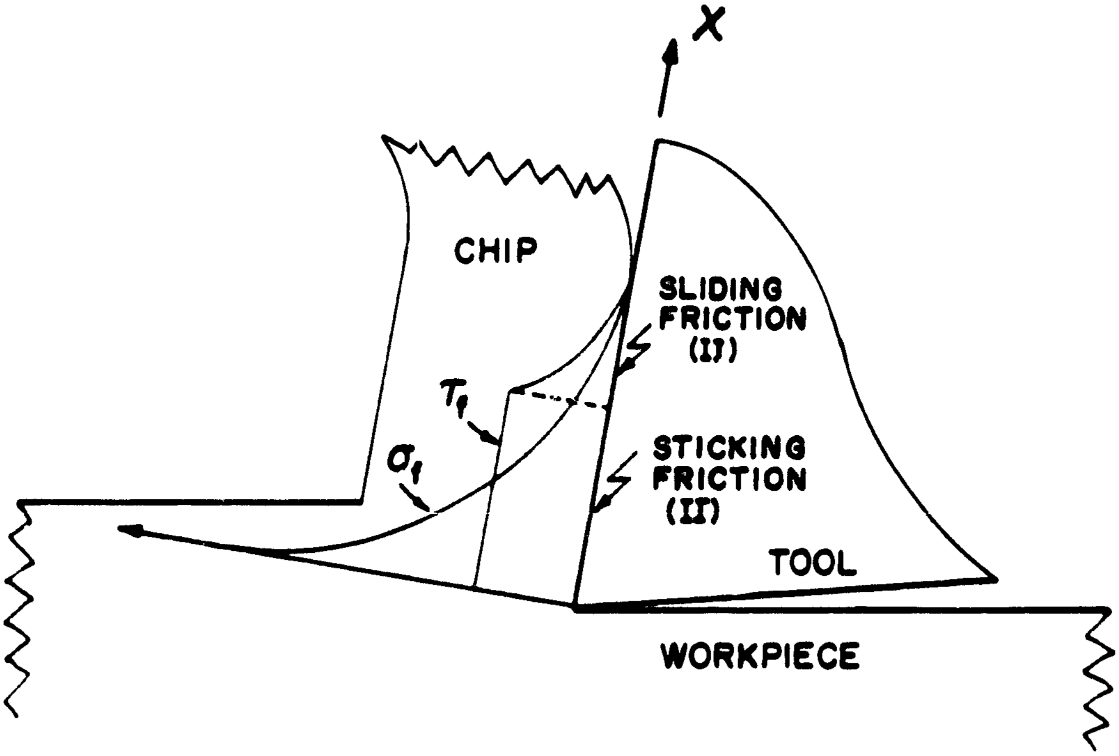

Figure 5.2. Non-Uniform Stresses on the Rake Face With Two Zones for Friction(71)

stationary against the tool with subsequent layers having relative motion in shear, thereby creating a velocity gradient. If weaker secondary bonds exist at the tool-chip interface, then there will be relative motion between the chip and tool, or sliding friction. This is the case in zone II which lies beyond the seizure zone. Although work material frequently adheres to the tool during machining, it is difficult to determine if the adhesion takes place over all or part of contact area. The use of transparent saphire tools(69) to machine lead, aluminum and copper materials have shown two distinct regions: 1) One region where there was adhesion with material transfer to the tool, and 2) A second region where no transfer took place. In addition, the underside of the chip had two distinct regions. The area in contact with zone I is featureless, indicating intimate contact, while zone II has an impression of transferred material on the tool. Thus, direct observation of the chip and tool-chip contact region reveals two distinct zones.

Stress Distributions on the Rake Face

As originally modelled by Merchant(3) both the shear and normal stresses are uniformly distributed (see Figure 5.1) on the rake face. Zorev's model (see Figure 5.2) recognized the existence of seizure and modelled the normal stress, σ_f, to be a power function written as

$$\sigma_f = \sigma_{max} x^n \qquad (5.1)$$

where σ_{max} is the maximum normal stress on the rake face, x the distance from the point where the chip leaves the tool and n the power describing the stress distribution (72). The shear stress has assumed to remain constant over the seizure length ℓ_s and decrease according to

$$\tau_f = \mu \sigma_f = \mu \sigma_{max} (\frac{x}{\ell})^n \qquad (5.2)$$

over the sliding friction distance ℓ_f, where μ is the sliding coefficient of friction.

Experimentally, stress distributions on the rake face have been found by photoelastic (73, 74) and split-tool techniques (75, 76). While the various studies do not agree on the exact profile of the stress distributions or their mathematical form, one important point is clear in each study. The normal and shear stresses are not uniformly distributed on the rake face. In addition, all studies have shown a distribution for the shear stress very close to Zorev's with a uniform region (zone I - seizure) and nonlinear decreasing portion (zone II - sliding friction). Where disagreement occurs is in the form of the normal stress distribution. All researchers show it to decrease from a maximum to minimum where the chip leaves the rake face. However, some authors show it to decrease continually while others show it to have a uniform portion shortly after the cutting edge. Despite this disagreement, Zorev's model of secondary shear appears reasonable.

Generalized Energy Model for Metal Cutting

The generalized energy method developed here uses the basic framework of those developed previously(20, 21, 22) by partitioning the energy in the cutting into two parts - that due to shear, $\dot{W}_s$, and that due to secondary shearing and friction, $\dot{W}_f$. However, a generalized stress model for the rake face as developed by Zorev will be utilized(71). Figure 5.3 shows the stress distribution on the rake face under conditions of seizure and sliding where, redefining the origin to be the tool tip, the normal stress, σ_f, may be expressed as

$$\sigma_f = \sigma_{max} \left(\frac{x}{\ell}\right)^n \tag{5.3}$$

where σ_{max} and n retain the same meaning as before and ℓ is total contact length. The shear stress may be partitioned as follows

$$\tau_r = \begin{cases} \mu\, \sigma_{max} \left(\frac{x}{\ell}\right)^n & 0 \leq x \leq \ell_f \\ \tau_f & \ell_f \leq x \leq \ell \end{cases} \tag{5.4}$$

Integrating Equation 5.3, the normal force on the rake face may be found as

$$F = \int_0^{\ell} \tau_r b_2 dx \tag{5.5}$$

$$= \int_0^{\ell_f} t_r b_2 dx + \int_{\ell_f}^{\ell} \tau_r b_2 dx \tag{5.6}$$

$$= \int_0^{\ell_f} \mu\sigma_{max} \left(\frac{x}{\ell}\right)^n b_2 dx + \int_{\ell_f}^{\ell} \tau_f b_2 dx \tag{5.7}$$

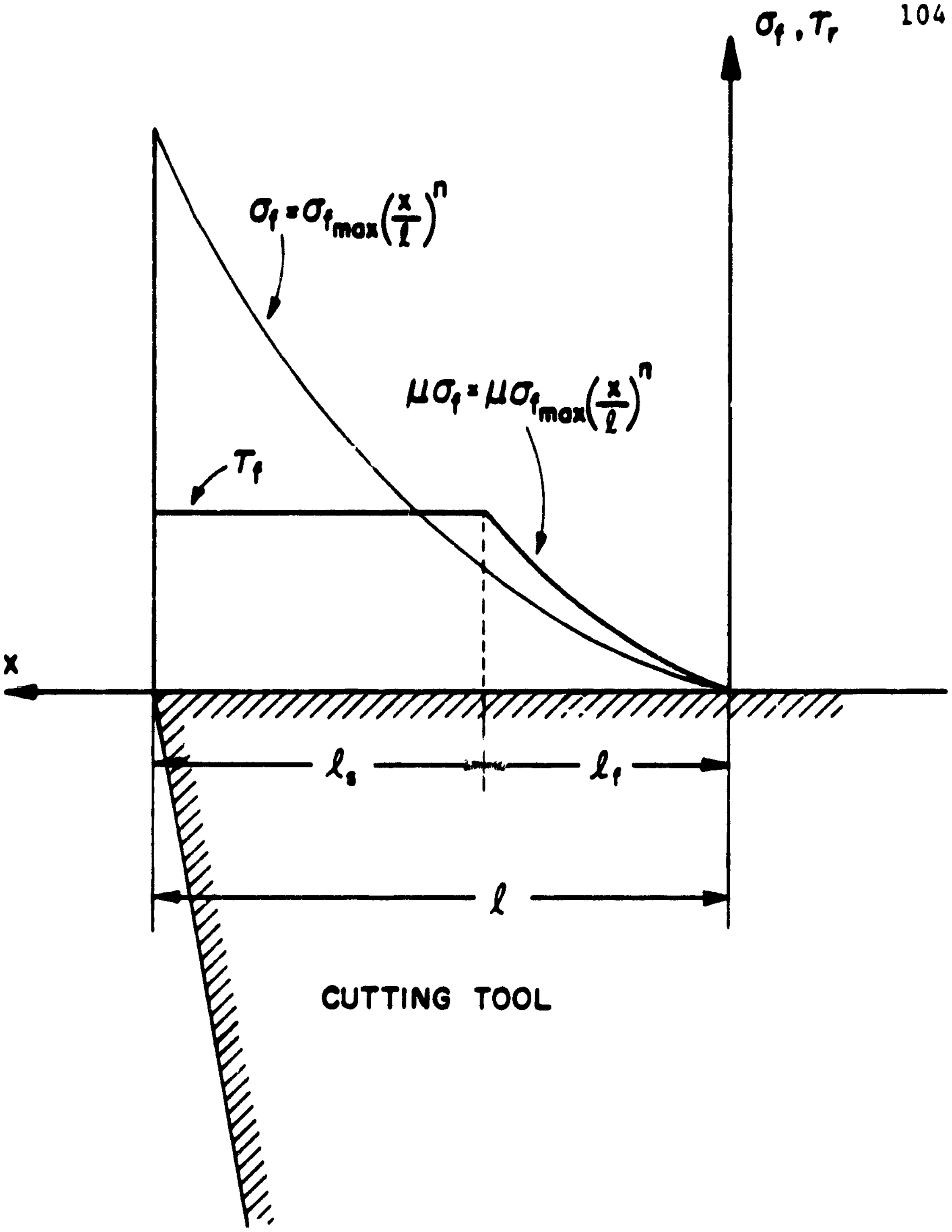

Figure 5.3. Model for Stress Distributions on the Rake Face in Metal Cutting

Similarly, the friction force, F, may be found as

$$= \frac{\mu\sigma_{max} b_2\, x^{1+n}}{(1+n)\ell^n}\Bigg|_{o}^{\ell_f} + \tau_f b_2 x\Bigg|_{\ell_f}^{\ell} \tag{5.8}$$

$$= \frac{\mu\sigma_{max} b_2 \ell_f^{\,1+n}}{(1+n)\ell^n} + \tau_f b_2(\ell - \ell_f) \tag{5.9}$$

$$= \frac{\tau_f b_2 \ell_f}{(1+n)} + \tau_f b_2 \ell_s \tag{5.10}$$

$$= \tau_f b_2 \left(\frac{1}{1+n}\ell_f + \ell_s\right) \tag{5.11}$$

The energy rates may now be partitioned. The shear energy rate may be written as

$$\dot{W}_s = F_s V \tag{5.12}$$

$$= \left(\frac{\tau_s b_1 t_1}{\sin\phi}\right)\left(\frac{V\cos(\alpha)}{\cos(\phi-\alpha)}\right) \tag{5.13}$$

$$= \frac{\tau_s b_1 t_1 V\cos\alpha}{\sin\phi\,\cos(\phi-\alpha)} \tag{5.14}$$

The friction/secondary shear energy rate may be analogously written as the product of friction force times the chip velocity. Using the friction as derived in Equation (5.16)

$$\dot{W}_f = FV_v \tag{5.15}$$

$$= \left(\tau_f b_2\left(\ell_s + \frac{1}{1+n}\ell_f\right)\right)\left(\frac{V\sin\phi}{\cos(\phi-\alpha)}\right) \tag{5.16}$$

Summing the energy rates, the total work rate, $\dot{W}$, may be written as

$$W = \dot{W}_s + \dot{W}_f \tag{5.17}$$

$$= \frac{\tau_s b_1 t_1 \cos\alpha}{\sin\phi\cos(\phi-\alpha)} + \frac{\tau_f b_2 V(\ell_s + \frac{1}{1+n})\ell_f \sin\phi}{\cos(\phi-\alpha)} \qquad (5.18)$$

Assuming that the process will accommodate the deformation geometry to consume the least energy, the optimal shear angle may be found which yields the minimum energy rate. A closed form solution cannot be found for this general expression for $\dot{W}$, so a computer search procedure must be instituted. However, a closed form solution of equation (5.18) can be found for a common special case in machining. When there is zero back rake angle ($\alpha=0$), the problem simplifies considerably as follows

$$\dot{W}_s\Big|_{\alpha=0} = \frac{\tau_s b_1 t_1 V}{\sin\phi\,\cos\phi} \qquad (5.19)$$

$$W_f\Big|_{\alpha=0} = \tau_f b_2(\ell_s + \frac{1}{1+n}\,\ell_f)\; V_{\tan\phi} \qquad (5.20)$$

which allows the energy rate to be rewritten as

$$\dot{W} = \frac{\tau_s b_1 t_1 V}{\sin\phi\,\cos\phi} + \tau_f b_2(\ell_s + \frac{1}{1+n}\ell_f)\; V_{\tan\phi} \qquad (5.21)$$

The shear angle to give minimum energy may therefore be found by finding $d\dot{W}/d\phi$ as follows:

$$\frac{d\dot{W}}{d} = \frac{t_1 b_1 V \tau_s(-\sin^2\phi + \cos^2\phi)}{\sin^2\phi\,\cos^2\phi} + \tau_f b_2 V(\ell_s + \frac{1}{1+n}\ell_f)$$

$$\sec^2\phi = 0 \qquad (5.22)$$

$$= \tau_s b_1 t_1(1-\cot^2\phi) + \tau_f b_2(\ell_s + \frac{1}{1+n}\ell_f) = 0 \qquad (5.23)$$

$$\therefore\ \tau_s b_1 t_1 + \tau_f b_2(\ell_s + \frac{1}{1+n}\,\ell_f) = \tau_s b_1 t_1 \cot^2\phi \qquad (5.24)$$

$$\tan^2\phi = \frac{\tau_s b_1 t_1}{\tau_s b_1 t_1 + \tau_f b_2 (\ell_s + \frac{1}{1+n}\ell_f)} \qquad (5.25)$$

$$\phi = \tan^{-1}\left[\left(\frac{\tau_s b_1 t_1}{\tau_s b_1 t_1 + \tau_f b_2 (\ell_s + \frac{1}{1+n}\ell_f)}\right)^{1/2}\right] \qquad (5.26)$$

Thus a simple closed form solution for the shear angle exists in this case as a function of the ratio of shear force to shear and friction force as expressed in terms of material properties (τ_s. τ_r , preset cutting parameters (b_1, t_1) and measurable quantities (ℓ_s, ℓ_f, b_2).

The dynamic shear stress, τ_s, is a material property, independent of cutting speed (35). τ_f may be approximated by the yield of the material being machined (35). Values of yield strength should be used from high strain rate tests made at elevated temperatures to attempt to simulate high strain rate metal cutting conditons. Values of l_s and l_f can be measured directly from the side of the chip (35). A highly polished specimen will show flow lines in the chip with seizure demonstrating flow lines which turn and run parallel to the rake face. The distinction is clear under high magnification and resolution.

Discussion

The model derived is general and applies to single as well as polycrystals as long as orientation related properties are known. From Figure 5.4 it is clear polycrystalline materials deform such that there is a strong

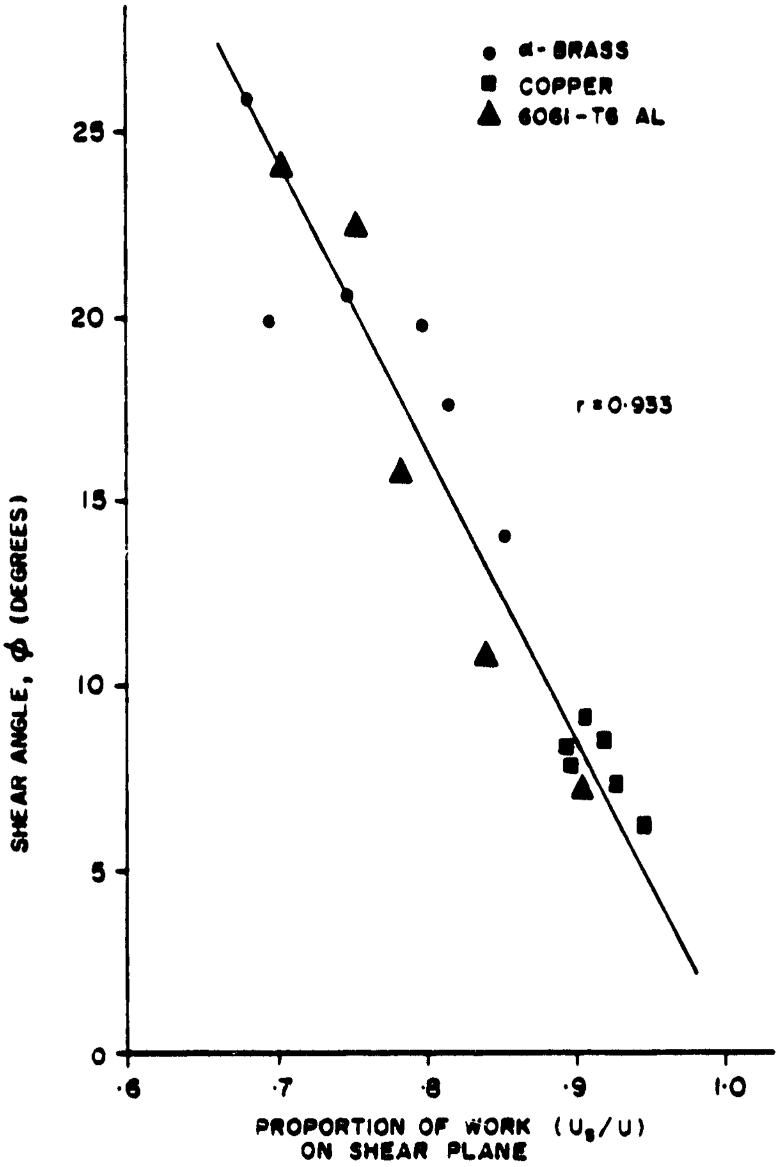

Figure 5.4. Relationship of Shear Angle to Ratio of Shear Work to Total Work for Brass, Copper and Aluminum(76)

linear relationship between shear angle and the proportion of total work done in shear as indicated by the correlation coefficient of 0.933(77). The same type of relationship holds true for various orientations of 1100 aluminum single crystals machined by Ramalingam and Hazra(19) as shown in Figure 5.5. An even more interesting result is shown when the crycrystalline brass, copper and 6061-T6 aluminum results are plotted along with the 1100 single crystal results of various orientation (see Figure 5.6). The results show a very strong linear correlation between shear angle and the proportion of the total work expended on the shear plane based on a total of 126 data points for all materials. Thus it appears that the distribution of energy between the primary shear plane and the secondary shear plane uniquely determines the shear angle regardless of material or crystallographic orientation although orientation surely changes the relative amount of energy expended in primary shear as shown in Figure 5.4. Therefore, the generalized energy method developed should apply equally as well to single crystals as it does to polycrystals given that the proper orientation dependent input data is available. In addition, the energy method developed is appealing in that it partitions the energy in an effort to find the optimal deformation geometry which minimizes the total energy.

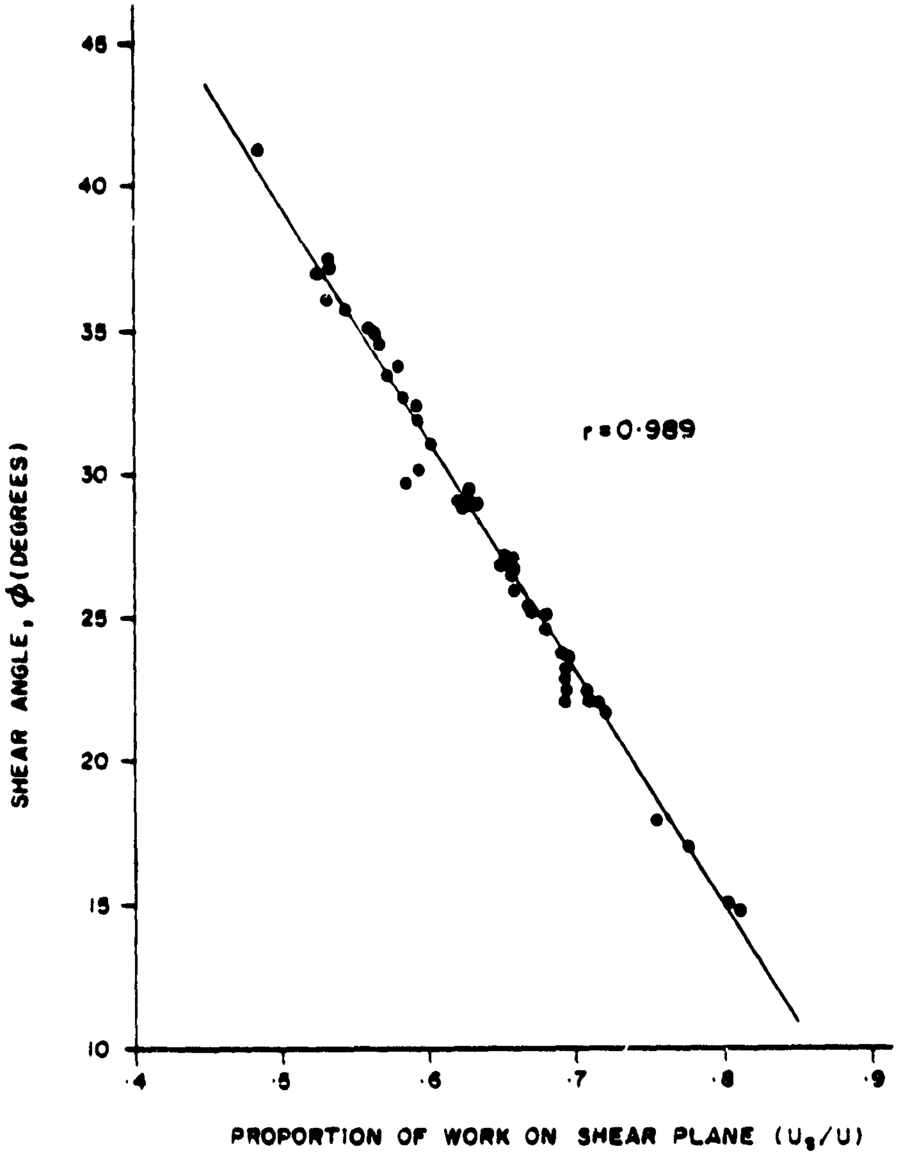

Figure 5.5. Relationship of Shear Angle to Ratio of Shear Work to Total Work for Orientations of Single Crystal 1100 Aluminum(19)

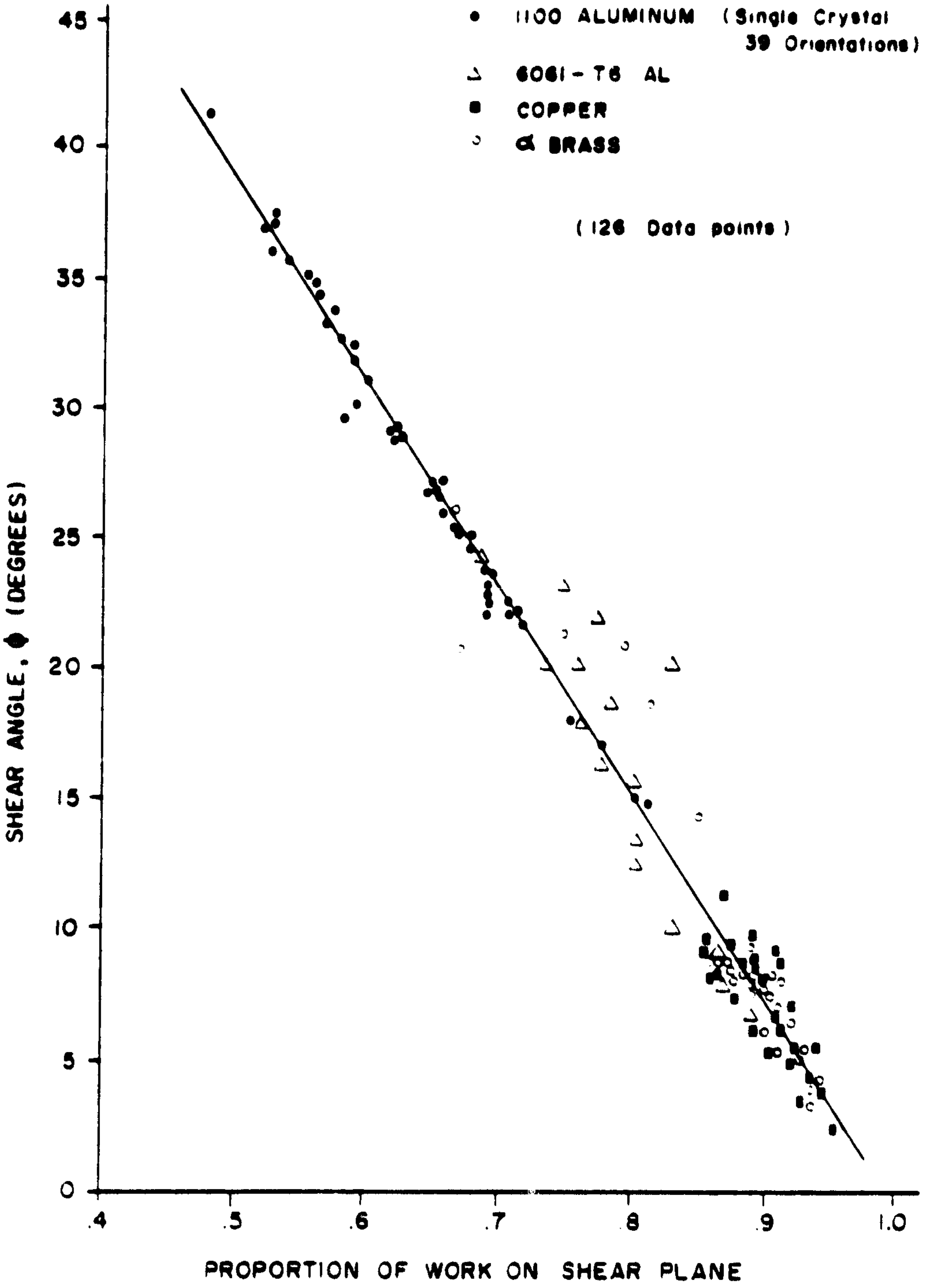

Figure 5.6. Combined Relationship Between Shear Angle and Proportion of Work Expended on Shear Plane (19, 76).

An important point to be noted is that the compression deformation ahead of the tool will produce slip on favorable (111) <110> slip systems. Despite this, the shear angle does not correspond to a specific crystallographic slip system and thus necessitates a deviation from standard single crystal plasticity approaches.

Modified Energy Model

Recent experimental work by Horne (70) has shown zone I to really be composed of two distinct portions. One portion close to the tool tip does not exhibit seizure, while the remainder of zone I displays adhesion. This gives form to a stress distribution as shown in Figure 5.7 where the large normal stresses near the tool tip reduce the shear stress required to cause flow over the region ℓ_{s_1}. As the normal stress decreases, the shear stress increases as a power function to τ_f (i.e., sticking friction) over the length ℓ_{s_2} and decreases as a power function over the remaining distance ℓ_f of the contact length. Thus the shear stress distribution may be written as

$$\tau_r = \begin{cases} \mu\sigma_{max}\left(\frac{x}{\ell}\right)^n & 0 \leq x \leq \ell_f \\ \tau_f & \ell_f \leq x \leq \ell_i \\ \tau_f \left(\frac{\ell - n}{\ell_{s_1}}\right)^n & \ell_i \leq x \leq \ell \end{cases} \tag{5.27}$$

ORIGINAL PAGE IS
OF POOR QUALITY

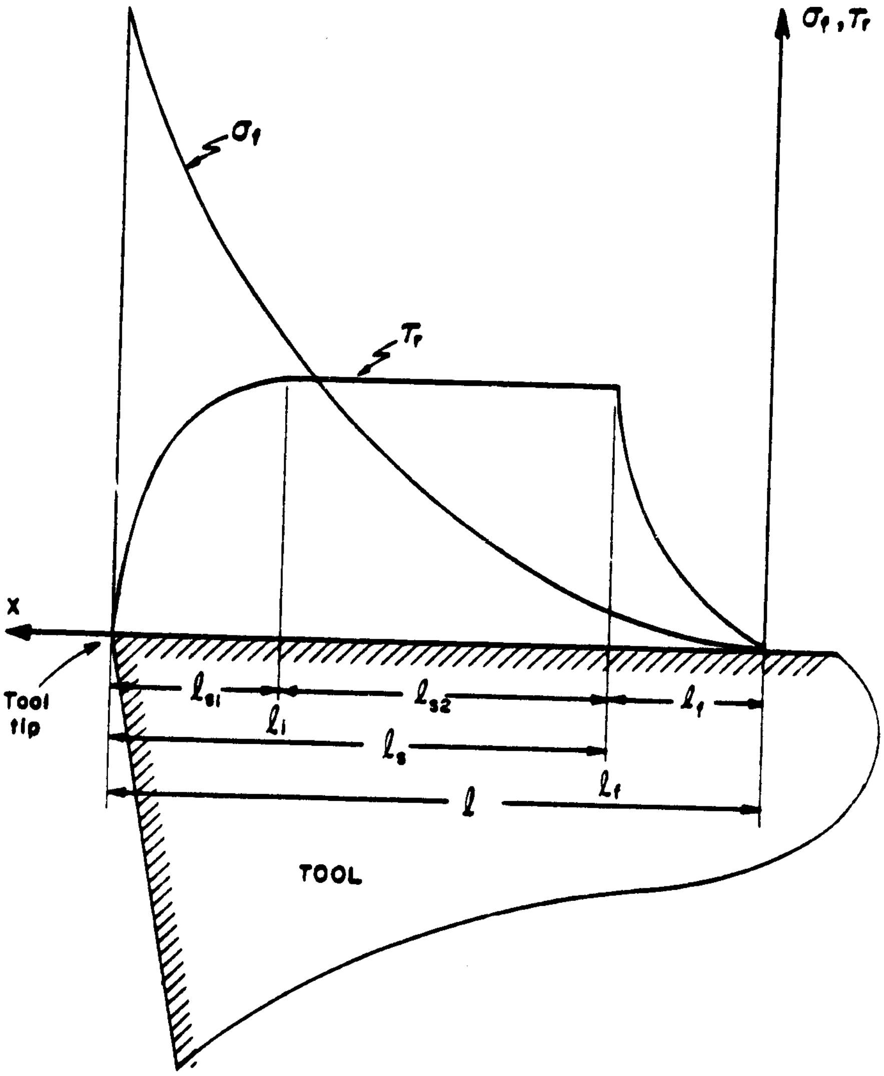

Figure 5.7. Modified Stress Distributions on the Rake Face

which is similar to Zorev's development with the exception of the initial portion of the distribution. Similar to the two zone shear model, the friction force, F, may be found by integrating the shear stress over area of contact on the rake force as

$$F = \tau_f b_2 \left(\frac{1}{1+m}\ell_{s_1} + \ell_{s_2} + \frac{1}{1+n}\ell_f\right) \tag{5.28}$$

The rake energy rate can be analogously written as

$$\dot{W} = \frac{{}_s b_1 t_1 V\cos}{\sin\phi\cos(\phi-\alpha)} + \frac{{}_f b_2 \left(\frac{1}{1+m} s_1 + s_2 + \frac{1}{1+n} f\right) V\sin}{\cos(\phi-\alpha)} \tag{5.29}$$

which for the case of zero back rake yields

$$\phi = \tan^{-1}\left[\left(\frac{\tau_s b_1 t_1}{\tau_s b_1 t_1 + \tau_f b_2\left(\frac{1}{1+m}\ell_{s_1} + \ell_{s_2} + \frac{1}{1+n}\ell_f\right)}\right)^{1/2}\right] \tag{5.30}$$

Three Dimensional Response Surface for the Workrate in Metal Cutting

Regardless of which model for the shear stress distribution on the rake face one considers, there are three classes of variables (inputs) which control the work spent in metal cutting. They are:

1. Material properties (i.e., τ_s, τ_f)
2. Process parameters (i.e., V, b_1, t_1)
3. Geometry of deformation (i.e., ϕ, α)

The dynamic shear stress (τ_s) and friction shear stress (τ_f) are material dependent. The speed (V), depth of cut (t_1), width of cut (b_1), and tool geometry (α) are set by the operator. However, the back rake angle does constrain the deformation process. With the exception of the bulk workpiece material, it is the only constraint on the plastic deformation in chip formation. It therefore may be classified along with the shear angle as defining the geometry of metal cutting. In fact, they solely define the shear strain in chip formation. Viewing the energy rate as a function of shear angle and back rake angle yields a 3-dimensional concave response surface or energy envelope, as shown in Figure 5.8.

The nature of the response surface is clarified by selecting an example taken from the work of Wright and Schmidt (21) for free machining steel, with the conditions and properties listed in Table 5.1. Figure 5.9 displays the work rate as a function of shear angle for various tool geometries. From this figure it is clear that larger positive rake angles take less energy and shear at larger angles, indicating that a larger proportion of work is done on the rake face. These observations from the model are easily verified in practice. In addition, the form of the workrate curves shows negative rake tools to have distinct points of minimum energy and to be highly sensitive to changes in shear angle. Large positive rake angles, however, have an energy rate which is fairly insensitive to changes in shear direction. Thus, slight changes in the workrate as in varying friction and secondary

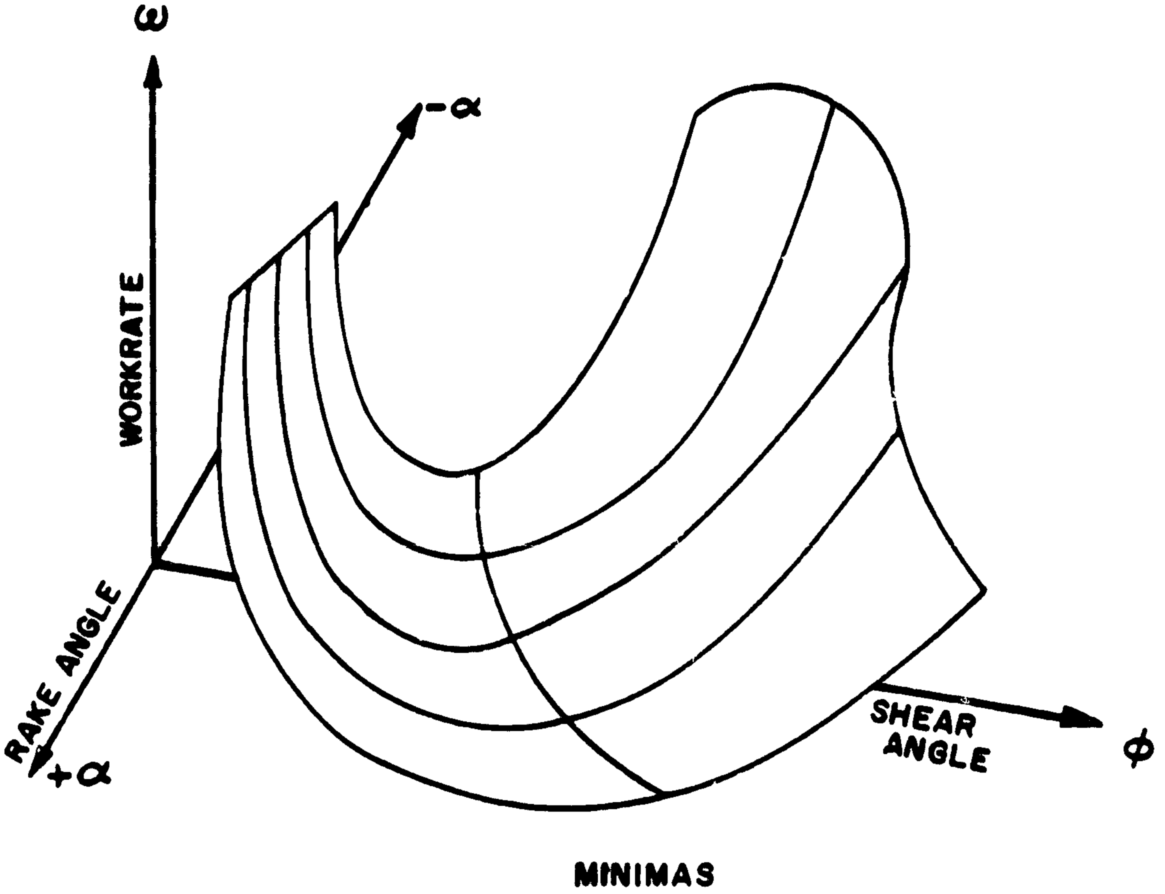

Figure 5.8. Three Dimensional Response Surface for the Workrate in Metal Cutting

Table 5.1. Data Utilized for Energy Envelope Calculations(69)

Properties	
Dynamic Shear Stress, τ_s	560 N/mm^2
Friction Shear Stress, τ_f	195 N/mm^2
Tooling	
Back rake angle, α	0 degrees
Contact length, ℓ	1·57 mm
Material	carbide
Cutting Parameters	
Speed, V	150 m/min
Depth of Cut, t_1	0·2 mm
Power Function	
Coefficient, n	1

ORIGINAL PAGE IS
OF POOR QUALITY

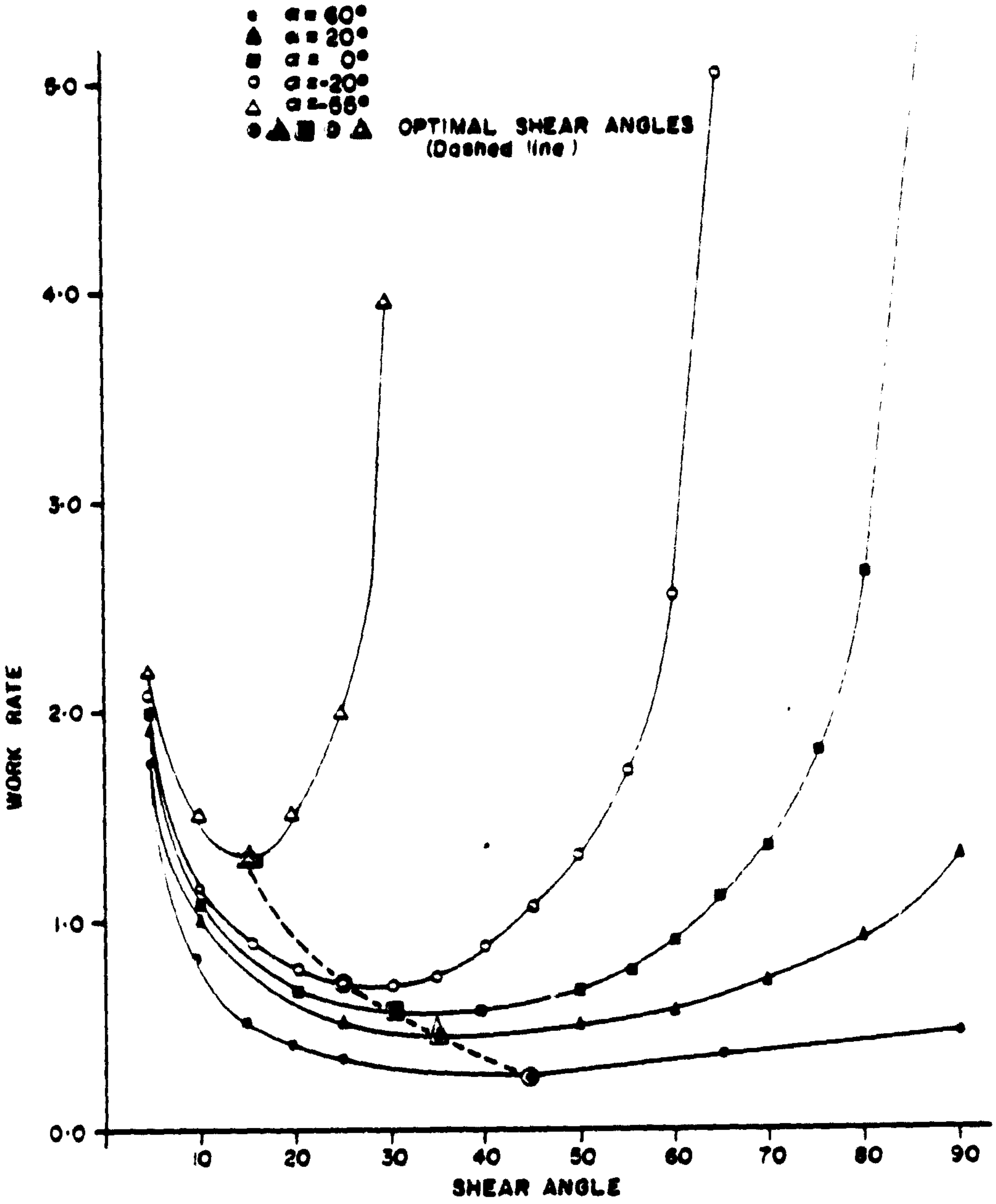

Figure 5.9. Workrate as a Function of Shear Angle for Various Tool Geometries(69)

shear conditions, or second phase particles which alter the dynamic shear stress, can radically effect the shear angle. Therefore, cutting experiments to verify shear angle relationships (which are typically run with positive back rake angles) are very difficult even under highly controlled conditions. However, the concept of a three-dimensional energy envelope does explain at least qualitatively the chip formation process and with adequate information, can form the basis of a good quantitative model.

CHAPTER VI

MEASUREMENT OF SHEAR VELOCITY

The chip formation process is a complex one where material is compressed ahead of the tool before it is sheared on a virtually flat, thin plane, defined by the shear angle, ϕ. After shearing, the chip slides along the rake face of the tool which is inclined at an angle, α, from the vertical. Thus, the material enters the shearing process at some cutting speed, V, and shears with velocity V_s which is inclined from the horizontal by the shear angle, ϕ. After shearing, the chip rides over the tool (vertical inclination of α) with a chip velocity V_c. This is shown in Figure 6.1 and is known as the Velocity Traingle where the shear and chip velocity are geometrically defined as

$$V_c = \frac{\sin \phi}{\cos (\phi - \alpha)} V \qquad (6.1)$$

$$V_s = \frac{\cos \alpha}{\cos (\phi - \alpha)} V \qquad (6.2)$$

in accordance with Merchant's assumptions as listed in Chapter II.

It is important to realize that these relationships are based on, and calculated from the shear angle which

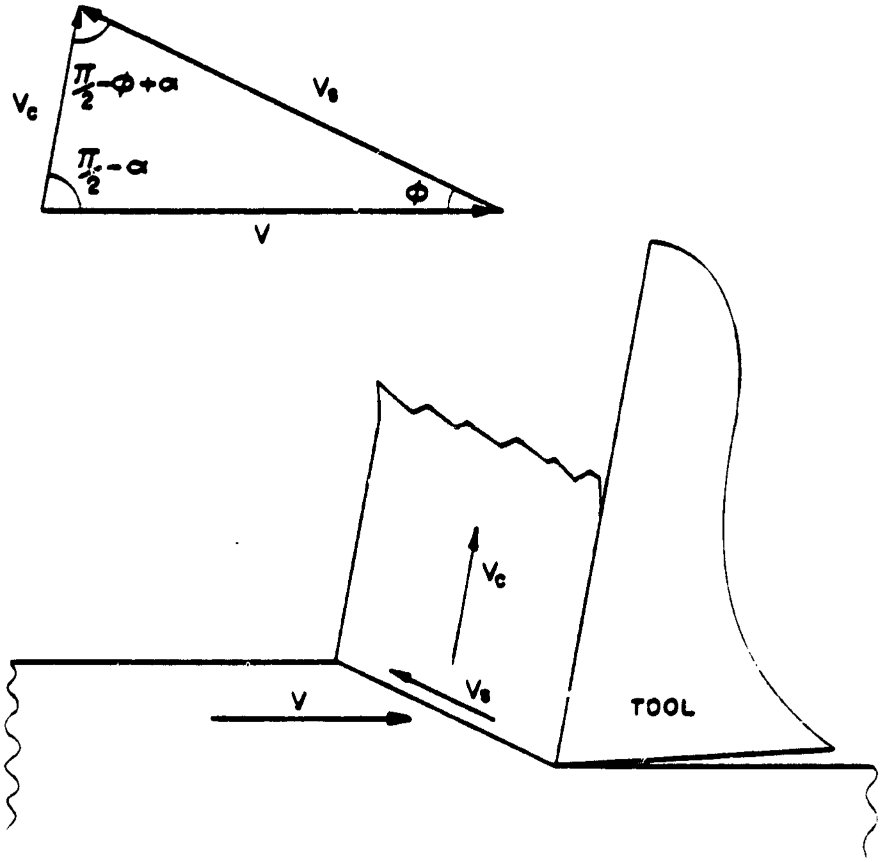

Figure 6.1. Velocity Triangle in Metal Cutting

is not directly measurable in a standard experiment. It is calculated by measuring the chip thickness and assuming that no sidespread occurs during the deformation.

The Velocity Triangle is a standard metal cutting mechanics result. It is constructed from numerous geometric assumptions of how the cutting process behaves. Thus it mirrors the most basic of the assumptions in the underlying theory. In addition, the shear and chip velocities are an integral part of any model which attempts to partition energy rates such as the ones presented in Chapter V.

However, the Velocity Triangle has never been verified. The only record of chip velocity measurement uses a weight attached to the chip with the velocity calculated by timing the weight of the chip over a known drop distance (79). No record of shear velocity measurement exists. The difficulty of measuring either quantity, particularly the shear velocity, is obvious due to the scale of the deformation and the exceptionally high strain rates of the process.

In order to perform an experiment capable of accurately measuring the shear and chip velocity and be able to compare it to the mechanics calculation, it is necessary to be able to directly measure the shear angle and to be able to view the shear front propagation in a material with an appropriate method of propagation distance and time measurement. The in-situ lathe experiments possesses each of these attributes. The recording of the deformation enables the direct measurement of the shear angle. A 2024-T36 aluminum disk was used which forms a highly discontinuous chip allowing for easy tracking of the shear front. The distance traveled by the crack can be directly measured from the screen with the appropriate scaling factor while utilizing the freeze-frame capability of the video recorder. With the time clock also displayed on each frame, the shear velocity can be measured. The chip velocity is measured analogously by following the previous shear parallel to the rake face. Figures 6.2 and 6.3 show the ease with which the shear front may be seen and thus tracked. The elapsed time between the two micrographs is 3/60 of a second. The methodology developed was used for eight tooling geometries and shown to be fairly accurate when compared to the velocities calculated from the mechanics. The average error is only 8.3 percent for the shear velocity and 9.6 percent for the chip velocity, excluding the 20 degree back rake angle tests with unrestricted and 0.022 inch contact lengths. In both cases the beginning of the formation of built-up edge was observed causing the measured chip velocity to be far less than the calculated. Full results along with measured shear angle are shown in Tables 6.1 and 6.2.

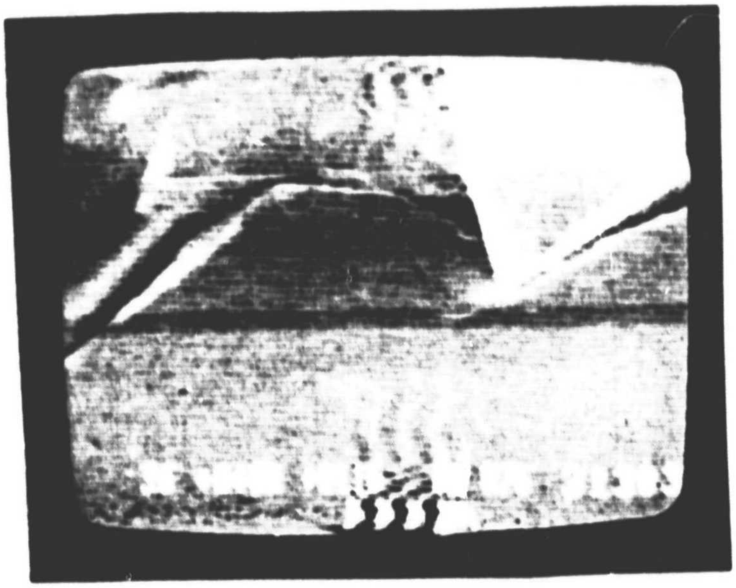

Figure 6.2. Initial Stages of Shear Front in 2024-T351 Aluminum

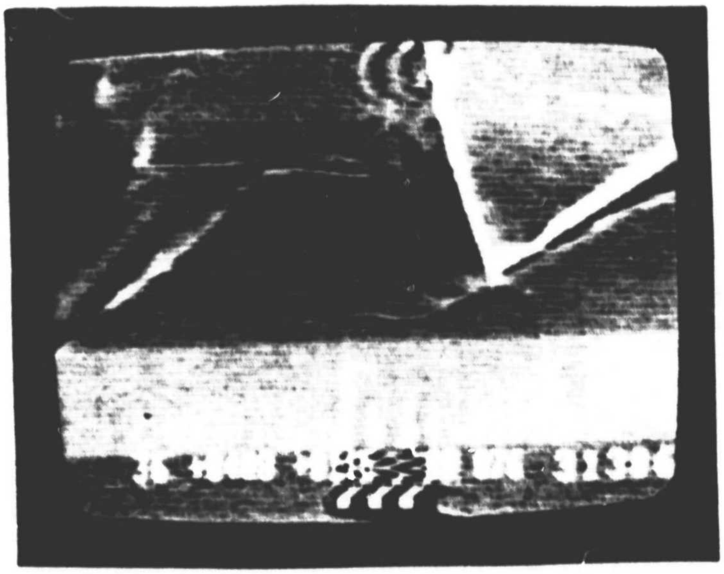

Figure 6.3. Progression of Shear Front in 2024-T351 Aluminum

Table 6.1. Results of Shear Velocity Measurement for 2024-T351 Aluminum

Tool Geometry		Shear Angle, ϕ (deg.)	V_s Measured (in./sec.)	V_s Calculated (in./sec.)	Percent Error
Back Rake (deg.)	Contact (in.)				
0		20	.0234	.0204	12.8
10		26	.0216	.0197	8.8
20		30	.0172	.0183	6.4
20	0.022	33	.0180	.0185	2.8
20	0.011	35	.0163	.0187	14.7
30		35	.0153	.0167	9.8
40		40	.0144	.0147	2.1
50		45	.0136	.0124	8.8

Table 6.2. Results of Chip Velocity Measurement for 2024-T351 Aluminum

Tool Geometry		Shear Angle, ϕ (deg.)	V_s Measured (in./sec.)	V_s Calculated (in./sec.)	Percent Error
Back Rake (deg.)	Contact (in.)				
0		20	.0072	.0070	2.8
10		26	.0084	.0087	4.2
20		30	.0069	.0097	40.6
20	.022	33	.0072	.0107	48.6
20	.011	35	.0114	.0114	00.0
30		35	.0090	.0110	22.2
40		40	.0112	.0123	9.8
50		45	.0124	.0147	18.5

The measured velocities are plotted in Figure 6.4 against the tool geometry (bake rake angle) for a constant measured input speed of 0.0192 inches/second. The correlation for both measured quantities is highly linear as expected by the mechanics (Equations 6.1 and 6.2) with correlation coefficients of -0.961 for the shear velocity and +0.891 for the chip velocity. The trend of both curves is also as expected. Larger rake tools cause the process to shear at larger shear angles, and the chip velocity should and does increase with the associated decrease in shear velocity. Based on the assumptions of orthogonal machining, it is a geometric consequence that the shear and chip velocities be equal when the rake face of the tool and hence the chip velocity direction are inclined at 45 degrees. The experimental observations show this to be approximately true.

One additional point is that the shear and chip velocities calculated are average values. The large shear velocities and short time needed for the shear front to propagate from the tip of the cutting tool to the free surface do not allow for the shear velocity to be tracked over time. However, the shear velocity was not observed to vary greatly during its propagation.

It is also clear that restricting the contact length to reduce the area over which the chip slides, reduces the frictional energy rate which increases the shear angle. The same result is true for polycrystalline copper, the results of which are shown in Table 6.3.

It is clear from this initial study that the mechanics derived by Merchant are in fact quite close to the measured results for the Velocity Triangle. This represents the first verification of Equations 6.1 and 6.2 since they were developed thirty-six years ago.

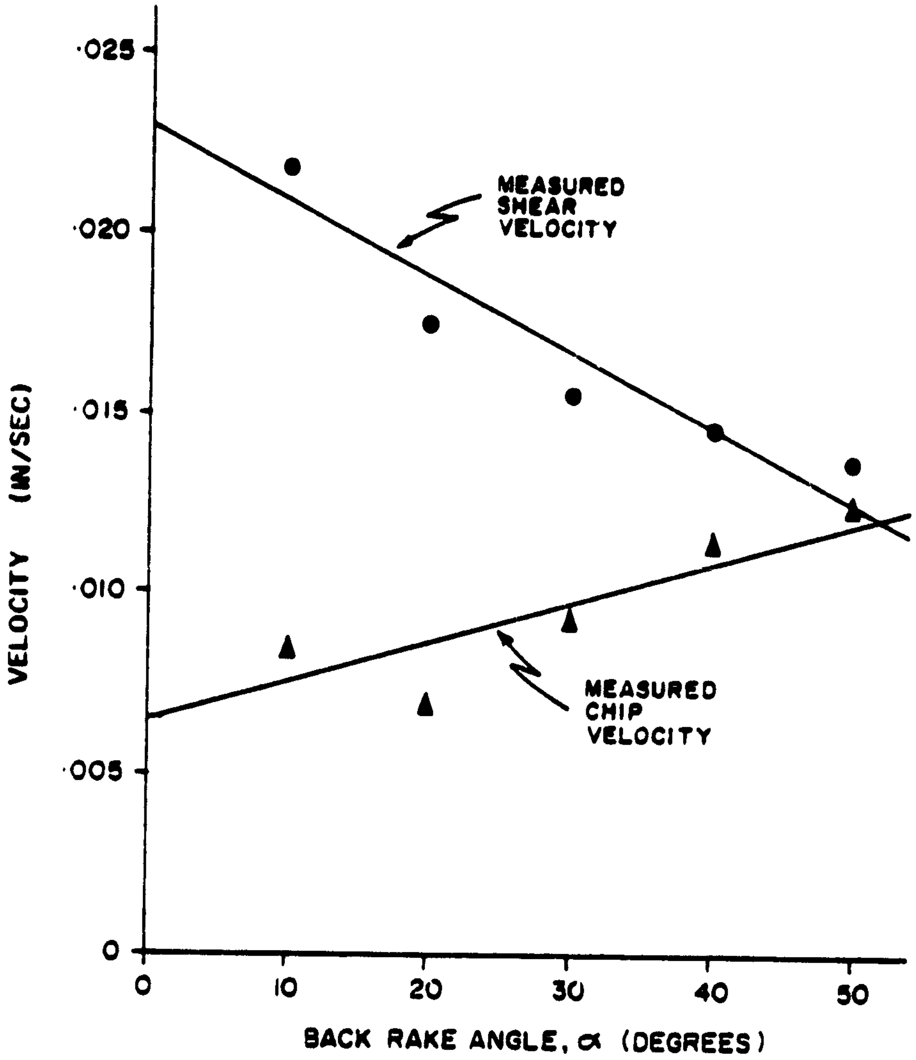

Figure 6.4. Variation of Measured Chip and Shear Velocities for 2024-T351 Aluminum With Back Rake Angle

Table 6.3. Results of Controlled Contact Polycrystalline Copper Experiments

Tool Geometry		Shear Angle, ϕ (deg.)
Back Rake (deg.)	Contact (in.)	
20	Unrestricted	8-9
20	.022	11-12
20	.011	15-17

CHAPTER VII

SINGLE CRYSTAL MACHINING RESULTS

Introduction

All previously published single crystal machining results have performed orthogonal linear cuts on a very limited number of orientations. Therefore, all previous single crystal work draws conclusions from a very limited data base. By utilizing single crystal disk specimens and machining around the periphery, an infinite number of orientations may be examined in a systamatic manner. This allows for an orderly examination of many orientations as well as an investigation of the patterns which may occur due to the crystallography.

As stated in Chapter IV, disks of single crystal (001) zone axis aluminum and copper are used. All tests were run at a nominal speed of 0.0218 inches/second for the 1½ inch diameter copper disks and 0.0175 inches/second for the 1 inch diameter aluminum disks (0.33 revolutions/minute on the disk), with a 0.0045 inch depth of cut. While leaving the cutting parameters the same, only the tool geometry was varied. The aluminum was cut with 20°, 30°, 40° and 50° back rake angles while copper was machined with back rakes of 0°, 20° and 40°. The 0° back rake on copper and back rake on copper and 20° back rake on aluminum did not, however, produce good results. In both cases, there was too much deformation and side-spread to accurately measure the shear angle or to have faith in the force measurements. Data and results for all tests performed are shown in Appendices A to D.

Results

Raw data was collected every five degrees of crystal rotation for all tests. With the video recorder stopped on a single frame, the measured component forces (F_H, F_V), shear angle (θ) and crystallographic orientation relative to the scribed "zero" were recorded. Both component forces as well as the shear angle were found to repeat in a consistent manner relative to the crystalography with the approximately sinusoidal pattern repeated every one-quarter revolution. This is to be expected since a (001) zone axis was chosen for the disk and the orientation presented to the cutting tool repeats every ninety degrees. The horizontal and vertical components are graphed in Figures 7.1 and 7.2 for a 40 degree back rake cutting tool with aluminum. Appendices E and F contain these plots for all tests run. In each case, both component forces are minimum when a <100> cutting direction is achieved. The maximum, however, does not occur when the disk is rotated 45 degrees such that the cut is parallel to a {111} <110> slip system. The maximum forces occur after another 15-20 degrees of

ORIGINAL PAGE IS
OF POOR QUALITY

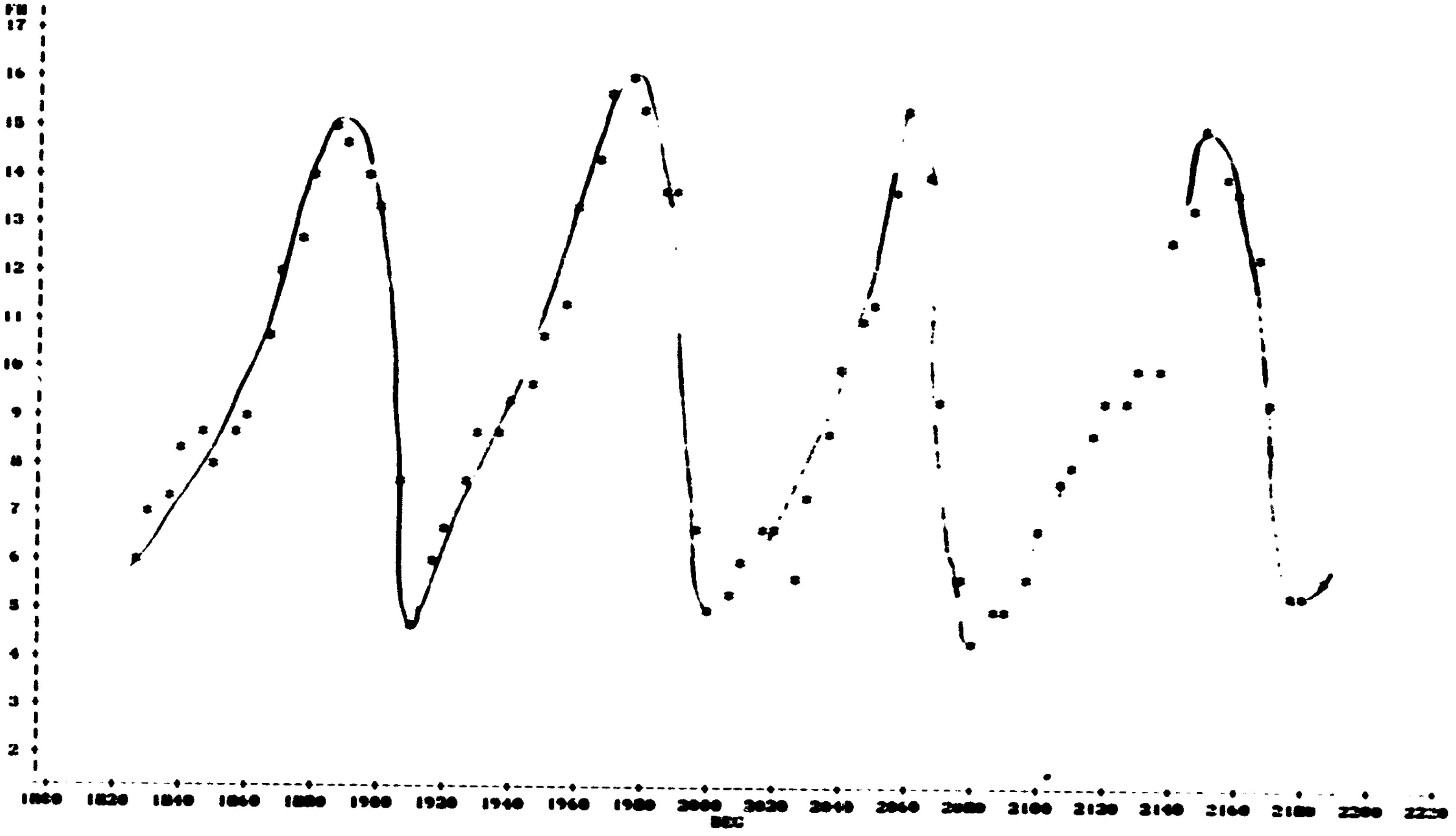

Figure 7.1. Variation of Horizontal Force With Orientation for Aluminum With 40° Tool, Test Al 56, Revolution 2

ORIGINAL PAGE IS
OF POOR QUALITY

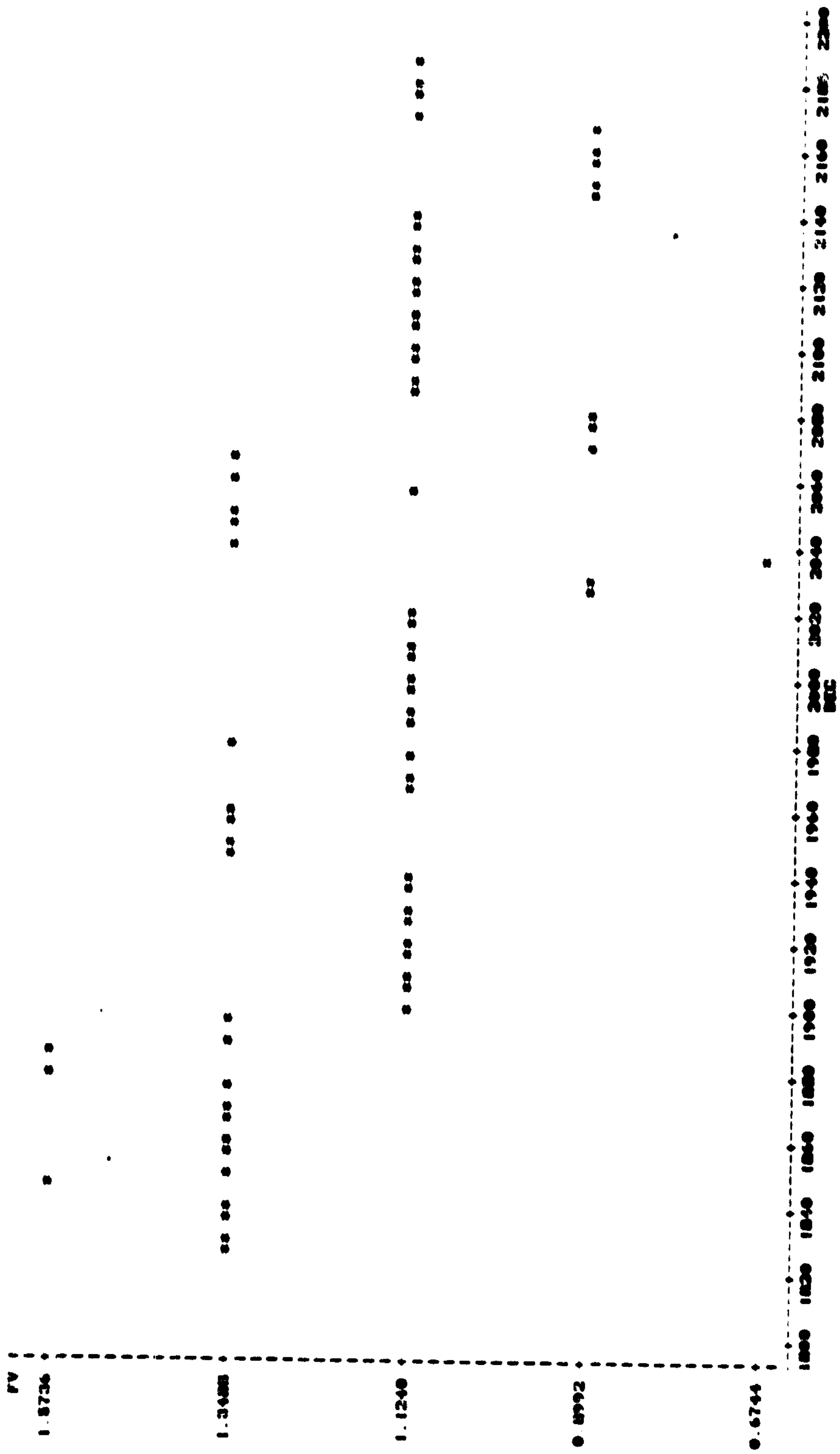

Figure 7.2. Variation of Vertical Force With Orientation for Aluminum With 40° Tool, Test Al 56, Revolution 1

rotation due to the complexity of the chip formation process. As the <110> cutting direction is approached, the forces of deformation increase, which should tend to activate additional slip systems, thus causing the offset. This offset was found in both aluminum and copper and correlates to the results found in single crystal tensile tests(37).

By the same reasoning, the shear angle has the same period as the cutting forces but achieves its maximum value during the [100] direction of cut since the (111) [110] (easy) slip system is aligned at 45 degrees to the cutting direction.

The minimum shear angle corresponds to degrees where forces are maximum and the (111) [110] slip system was rotated approximately 150 degrees past the cutting direction. This is shown in Figure 7.3, as well as Appendix G. Thus, the shear angle acts inversely to the cutting forces.

In the standard metal cutting experiment, the shear angle is calculated by measuring the thickness of the deformed chip. However, visually measuring the shear angle is far more accurate, especially when one considers that the varying shear angle is mirrored in the chip by having a continually changing chip thickness which would be virtually impossible to measure accurately and identify the exact crystallographic orientation. Figures 7.4 to 7.6 show the radical change in shear angle and accompanying

ORIGINAL PAGE IS
OF POOR QUALITY

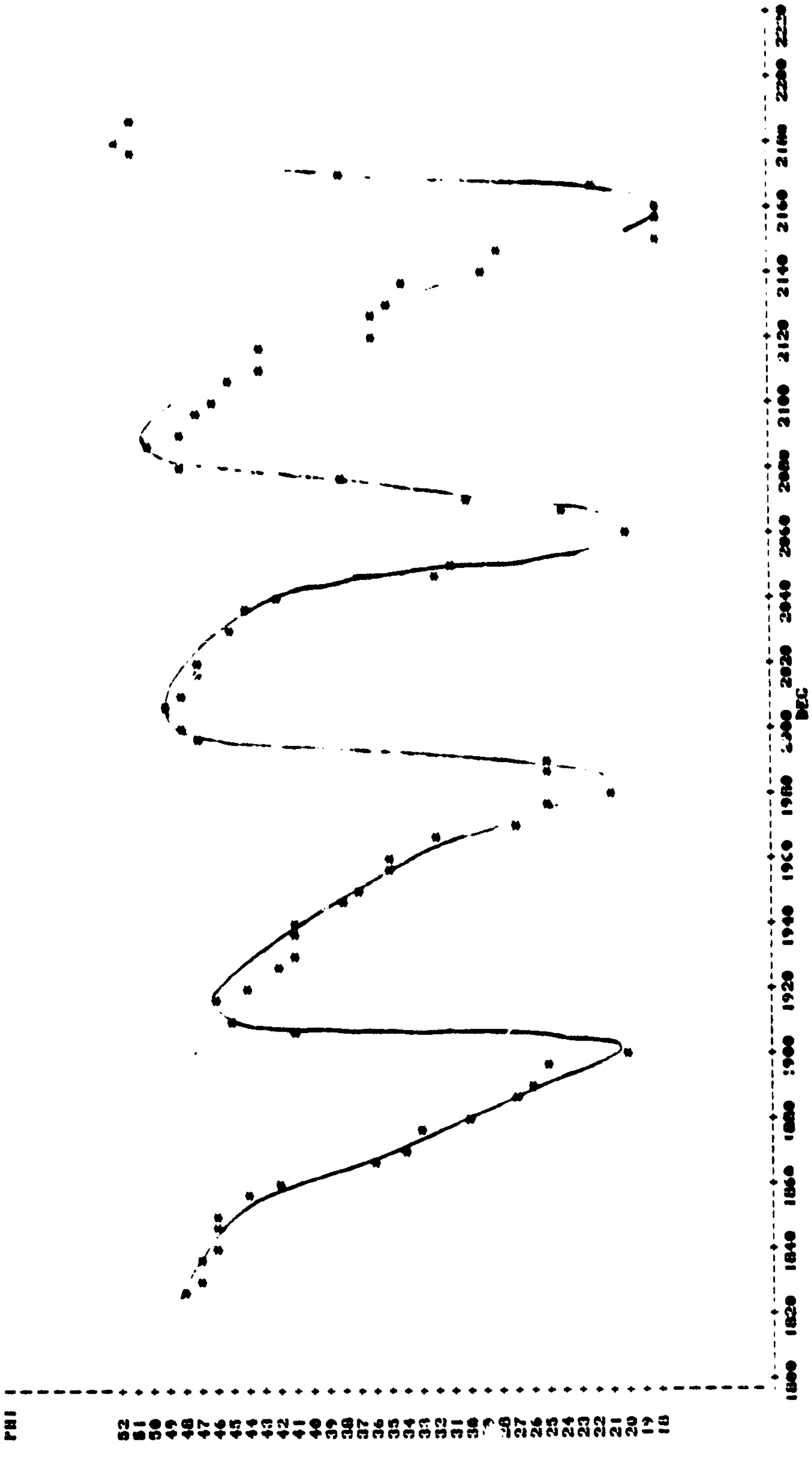

Figure 7.3. Variation of Shear Angle With Orientation for Aluminum With 40° Tool, Test Al 56, Revolution 1

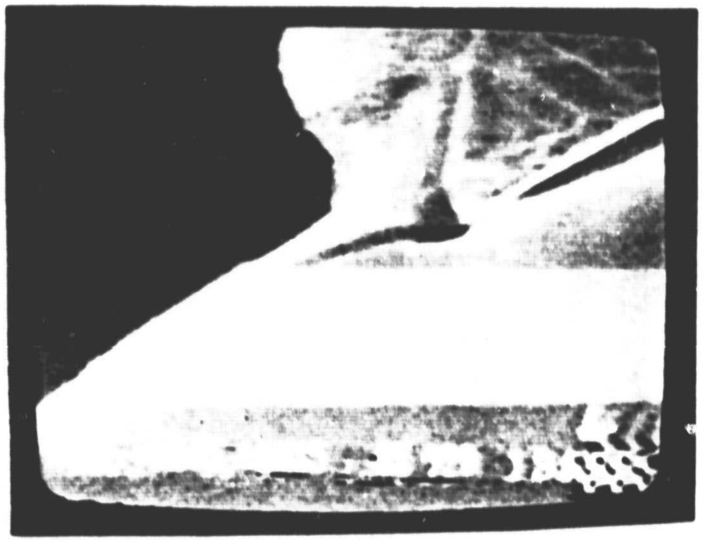

Figure 7.4. Favorable Orientation for Copper With 40° Tool

ORIGINAL PAGE
BLACK AND WHITE PHOTOGRAPH

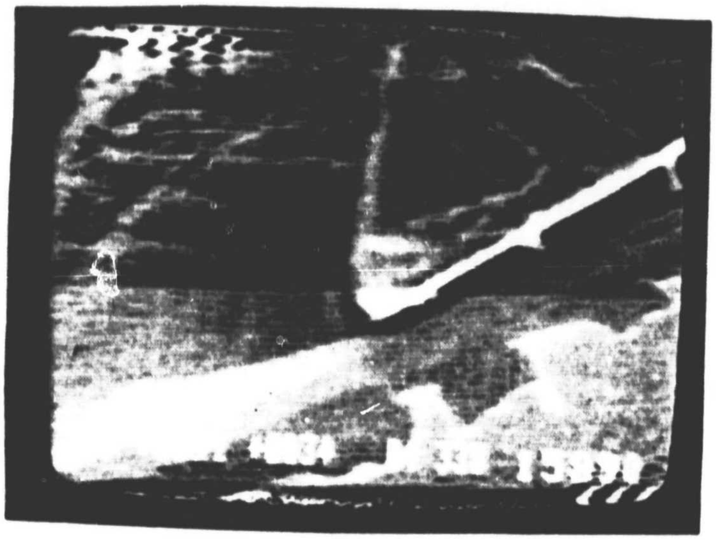

Figure 7.5. Orientation Between the Minimum and Maximum Shear Angles for Copper With 40° Tool

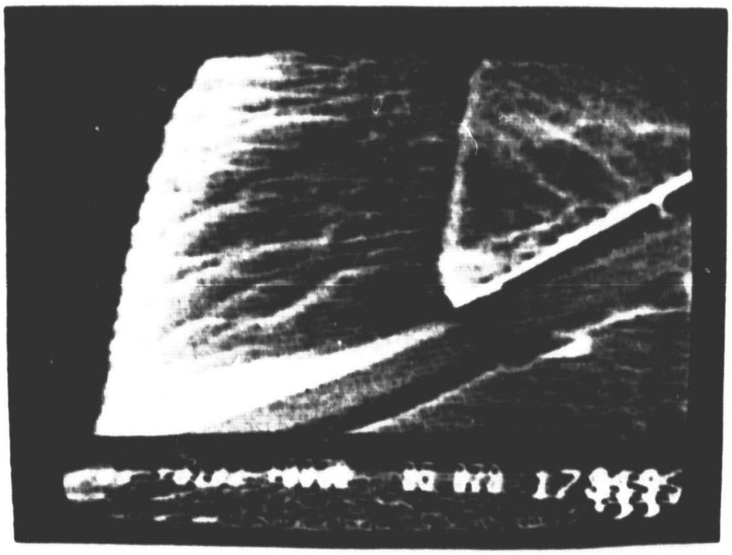

Figure 7.6. Unfavorable Orientation for Copper With 40° Tool

chip thickness for single crystal copper cut with a 40 degree back rake angle. Figure 7.4 in particular, clearly shows the rapid transition in chip thickness which results when a favorable orientation is presented to the tool. The favorable orientation results when the [100] cutting direction is approached. The same results occur when the tool geometry is changed to a 20 degree back rake angle. Figure 7.7 shows the transition in chip thickness for this case. Single crystal aluminum exhibited the same results for each tool geometry tested. Figure 7.8 shows an unfavorable orientation for a 40 degree tool. The orientation pictured in Figure 7.9 is a favorable one resulting in a large shear angle (with a 30 degree rake tool) and also displays the rapid transition from thick chip to thin chip.

As a natural consequence of the periodicity of the cutting forces and shear angle, the component forces which act on the shear plane and tool-chip interface also vary with the same period and phase as the cutting force components. Forces on the shear plane as shown in Figures 7.10 and 7.11 (and Appendices H and I) while forces on the rake face are shown in Figures 7.12 and 7.13 (and Appendices J and K). In addition the normal and shear stresses on the shear plane vary approximately sinusoidally in phase with the forces as shown in Figures 7.14 and 7.15 (and Appendices L and M).

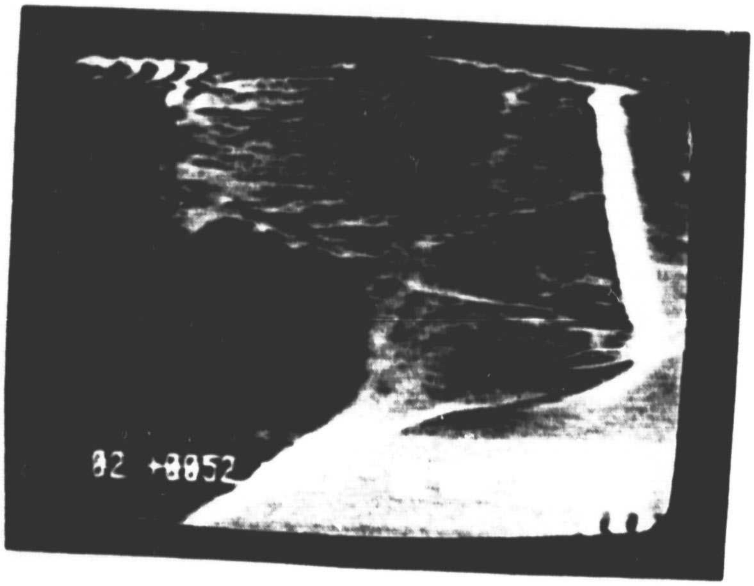

Figure 7.7. Radical Change in Chip Thickness for Copper With 20° Tool

ORIGINAL PAGE
BLACK AND WHITE PHOTOGRAPH

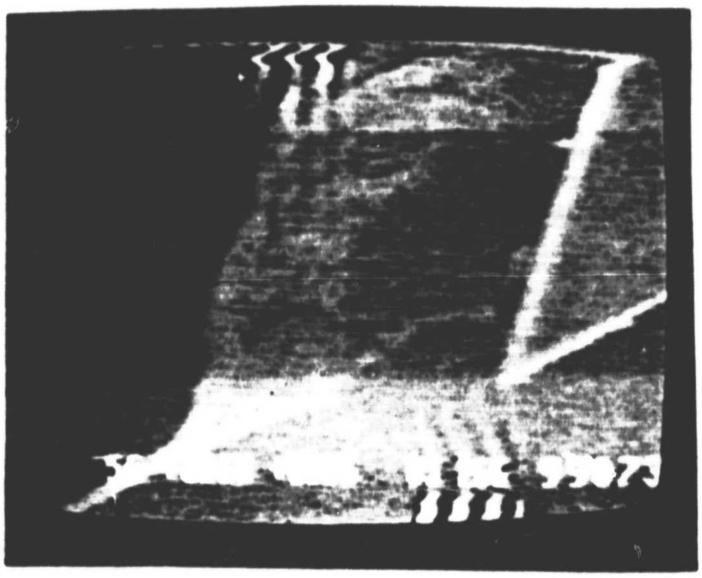

Figure 7.8. Unfavorable Orientation for Aluminum With 40° Tool

Figure 7.9. Favorable Orientation for Aluminum With 30° Tool

ORIGINAL PAGE IS
OF POOR QUALITY

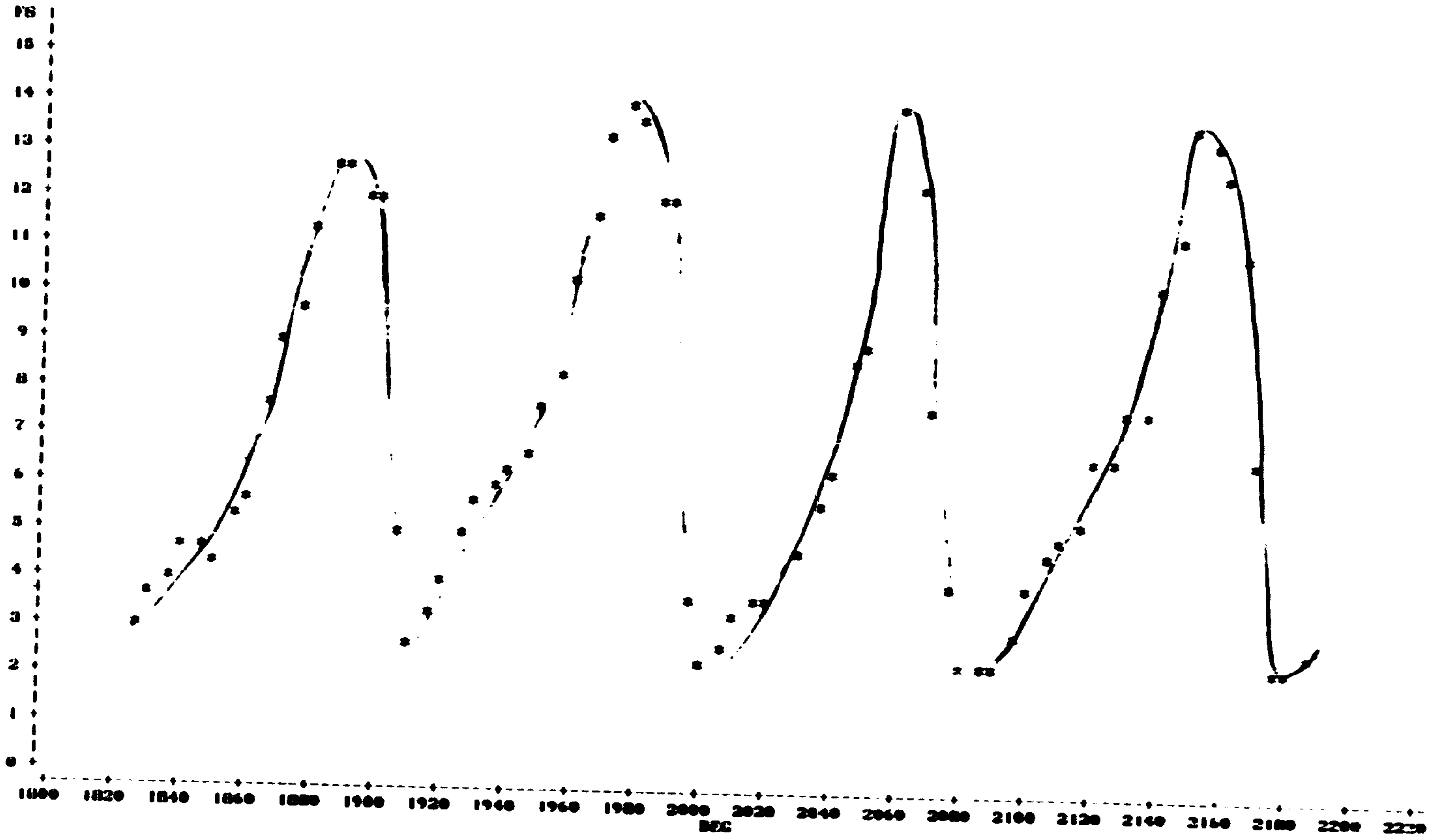

Figure 7.10. Variation of Shear Force With Orientation for Aluminum With 40° Tool, Test Al 56, Revolution 1

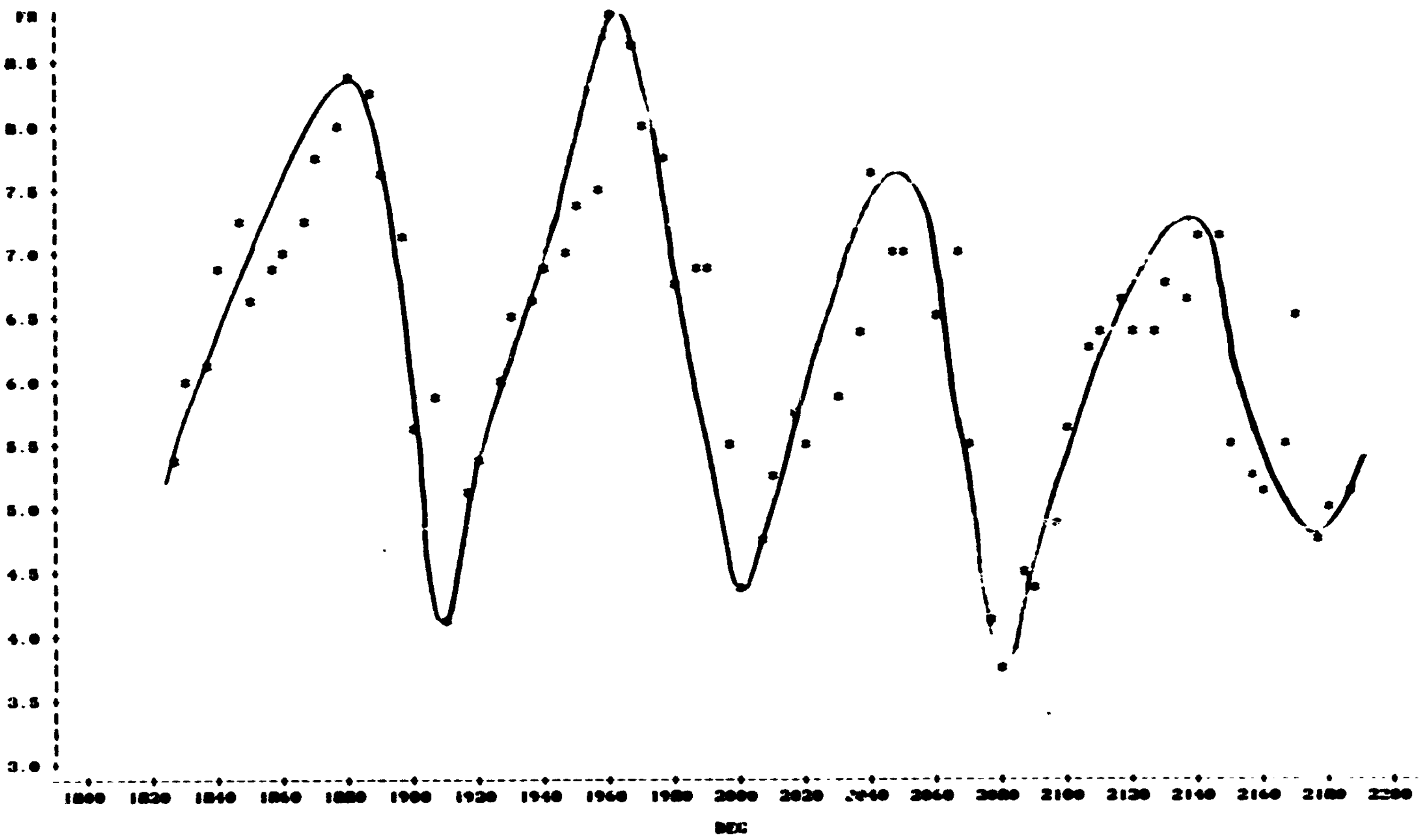

Figure 7.11. Variation of Force Normal to Shear With Orientation for Aluminum With 40° Tool, Test Al 56, Revolution 1

ORIGINAL PAGE IS
OF POOR QUALITY

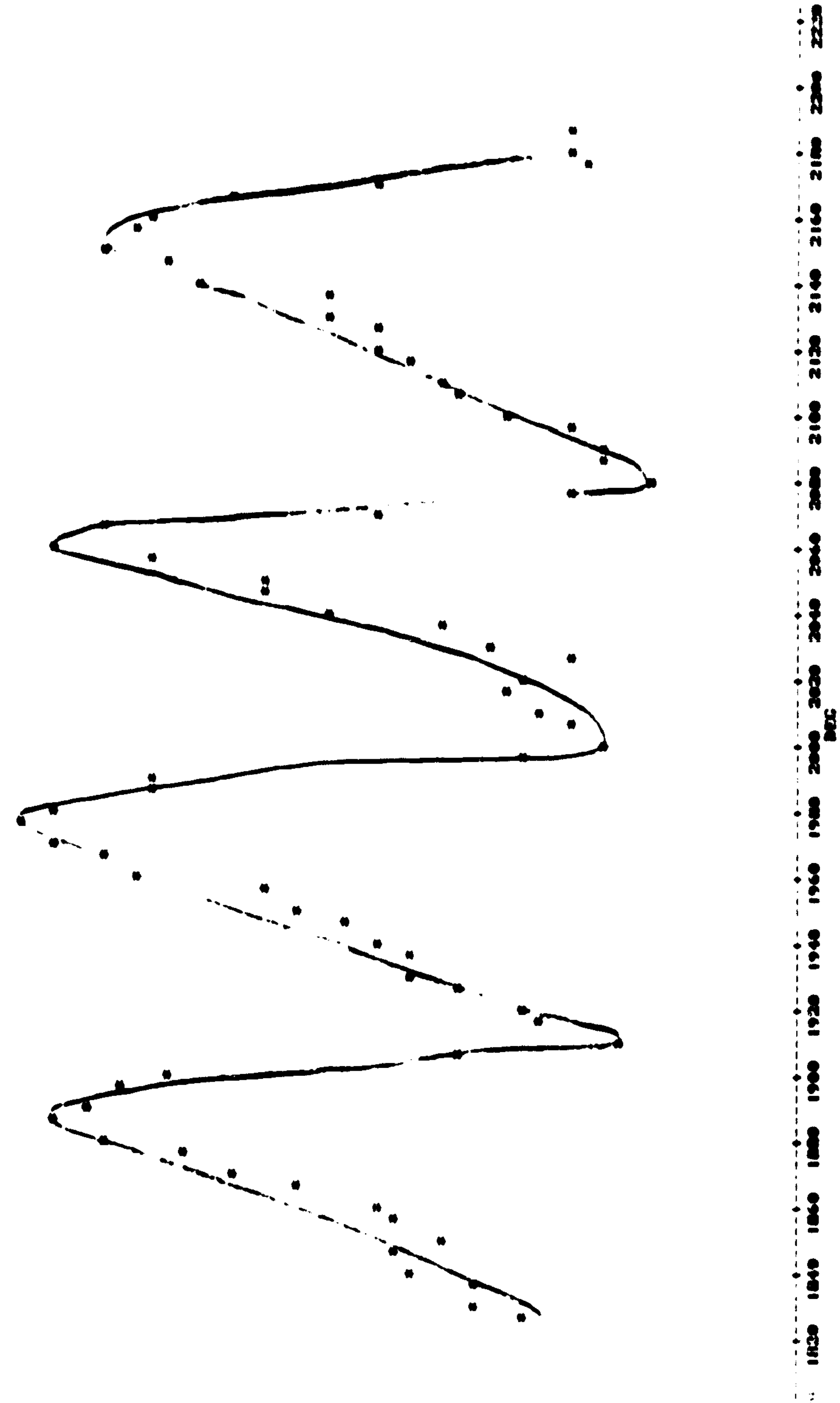

Figure 7.12. Variation of Friction Force With Orientation for Aluminum With 40° Tool, Test Al 56, Revolution 1

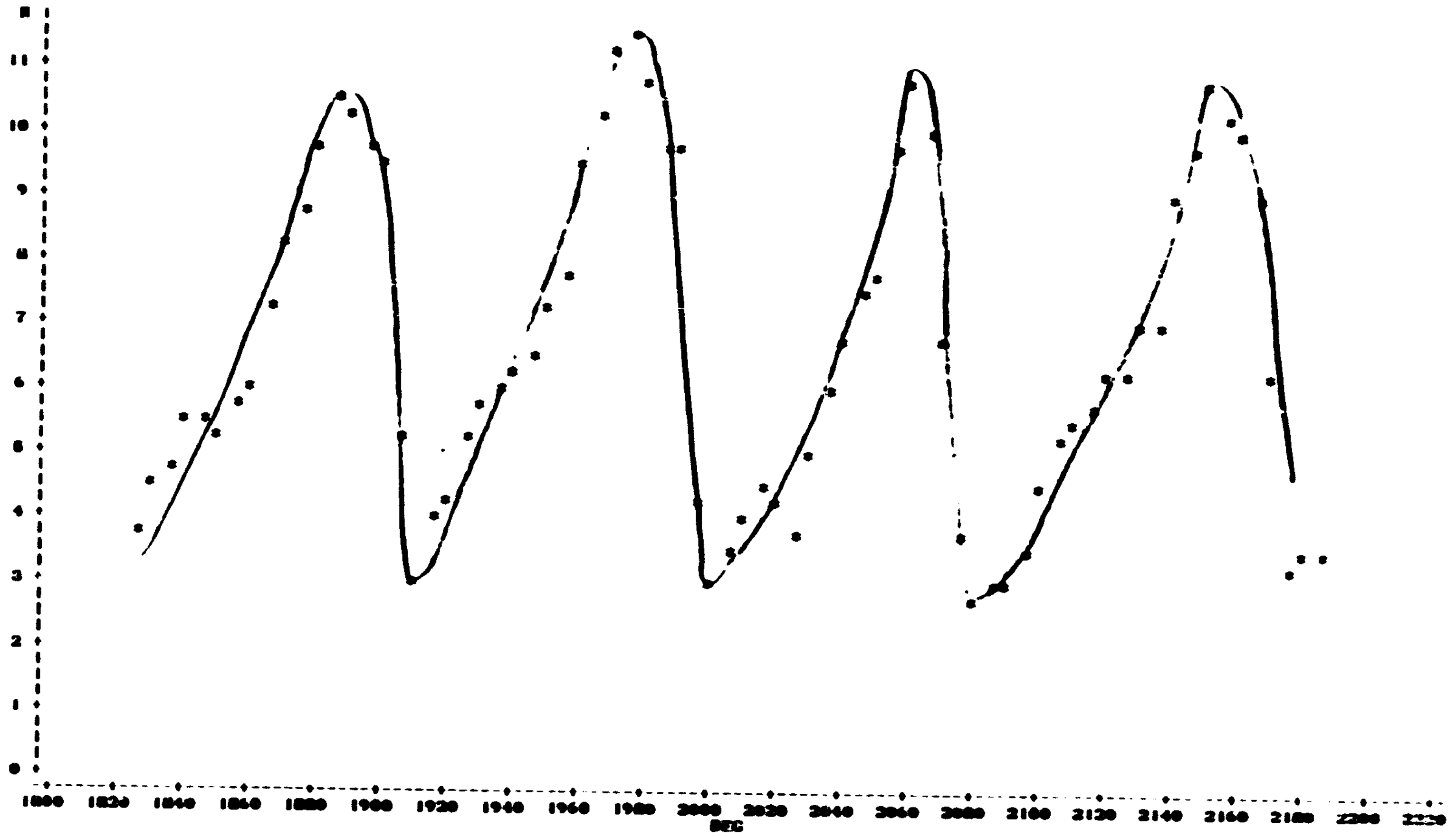

Figure 7.13. Variation of Normal to Friction Force With Orientation for Aluminum With 40° Tool, Test Al 56, Revolution 1

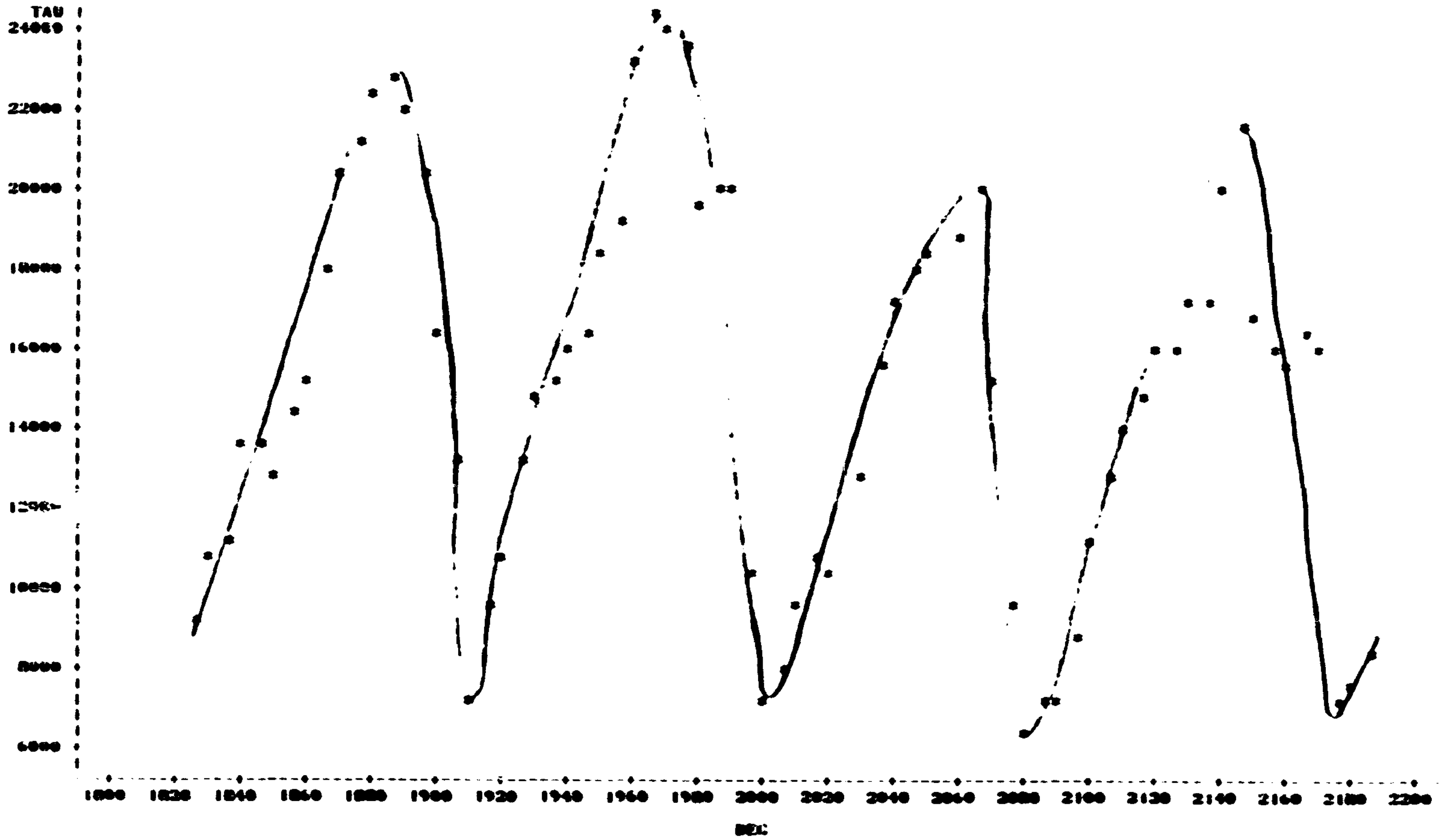

Figure 7.14. Variation of Dynamic Shear Stress With Orientation for Aluminum With 40° Tool, Test Al 56, Revolution 1

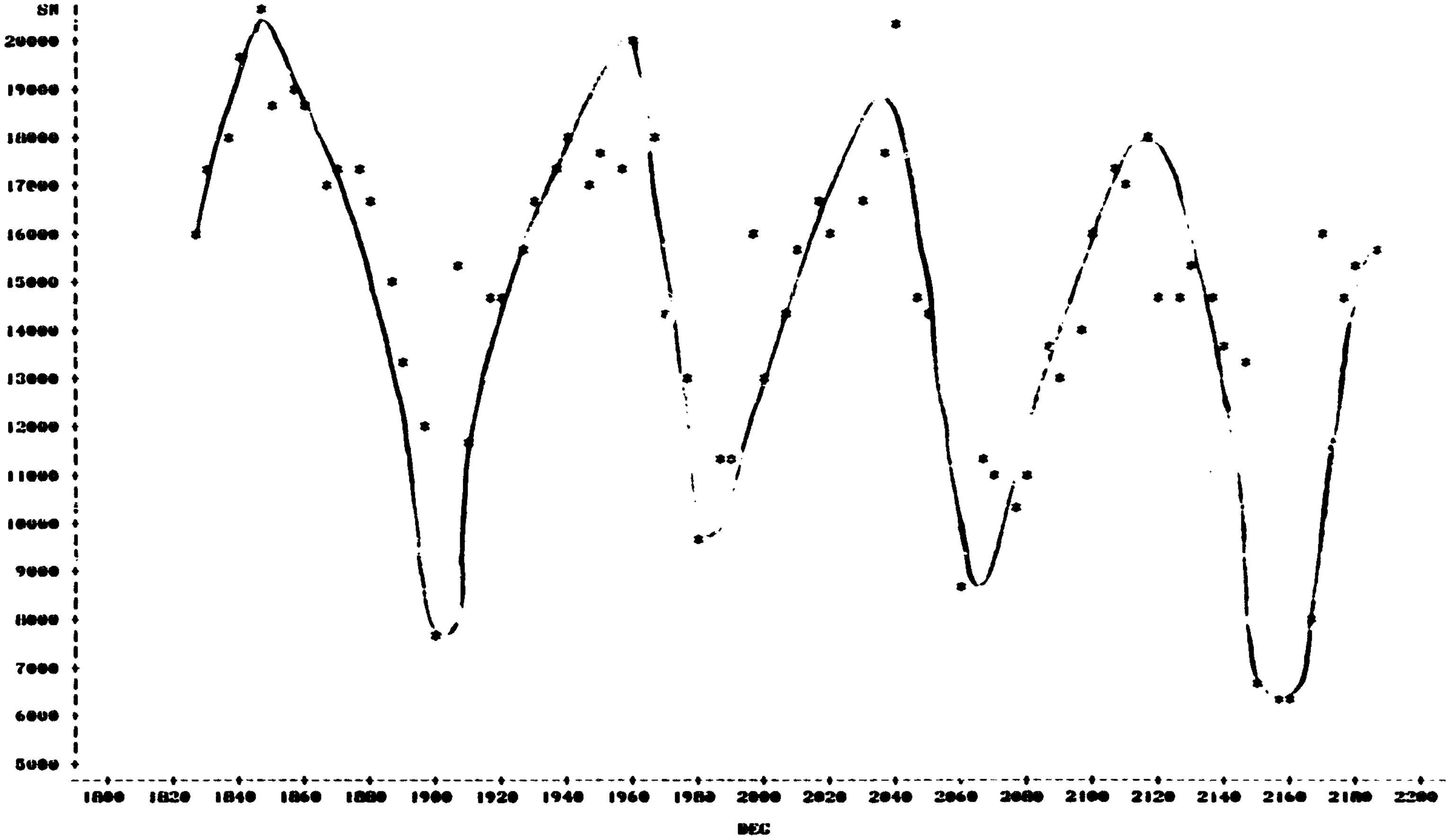

Figure 7.15. Variation of Normal Stress With Orientation for Aluminum With 40° Tool, Test Al 56, Revolution 1

Variation of the horizontal cutting force necessitates the same trend in the specific power since it is calculated directed from the horizontal force (see Figure 7.16 and Appendix N). Likewise, the proportion to total energy consumed in shear will vary with the same period and phase as the cutting forces as shown in Figure 7.17 and Appendix O.

While both the friction and normal forces on the rake face vary periodically with a minimum achieved with a [100] cutting direction, the coefficient of friction is offset from this by 45 degrees. The apparent anomaly can be explained by noticing that despite the same period and phase, the component forces change at different rates. Thus the ratio of them varies, but is 45 degrees out of phase as shown in Figure 7.18 and Appendix P. When interpreting the variation of the proportion of shear energy, it is clear that the coefficient of friction must be offset. When the proportion of energy in shear is maximum, it follows that the proportion due to friction and hence the coefficient of friction must be minimum.

While the shear strain is a function only of the shear angle, its phase is offset by approximately fourty-five degrees as shown in Figure 7.19 and Appendix Q. However, this result becomes clear when realizing the steeper the shear angle, the closer the direction of easy slip and shear plane align, thereby decreasing the necessary cross-slip and shear strain.

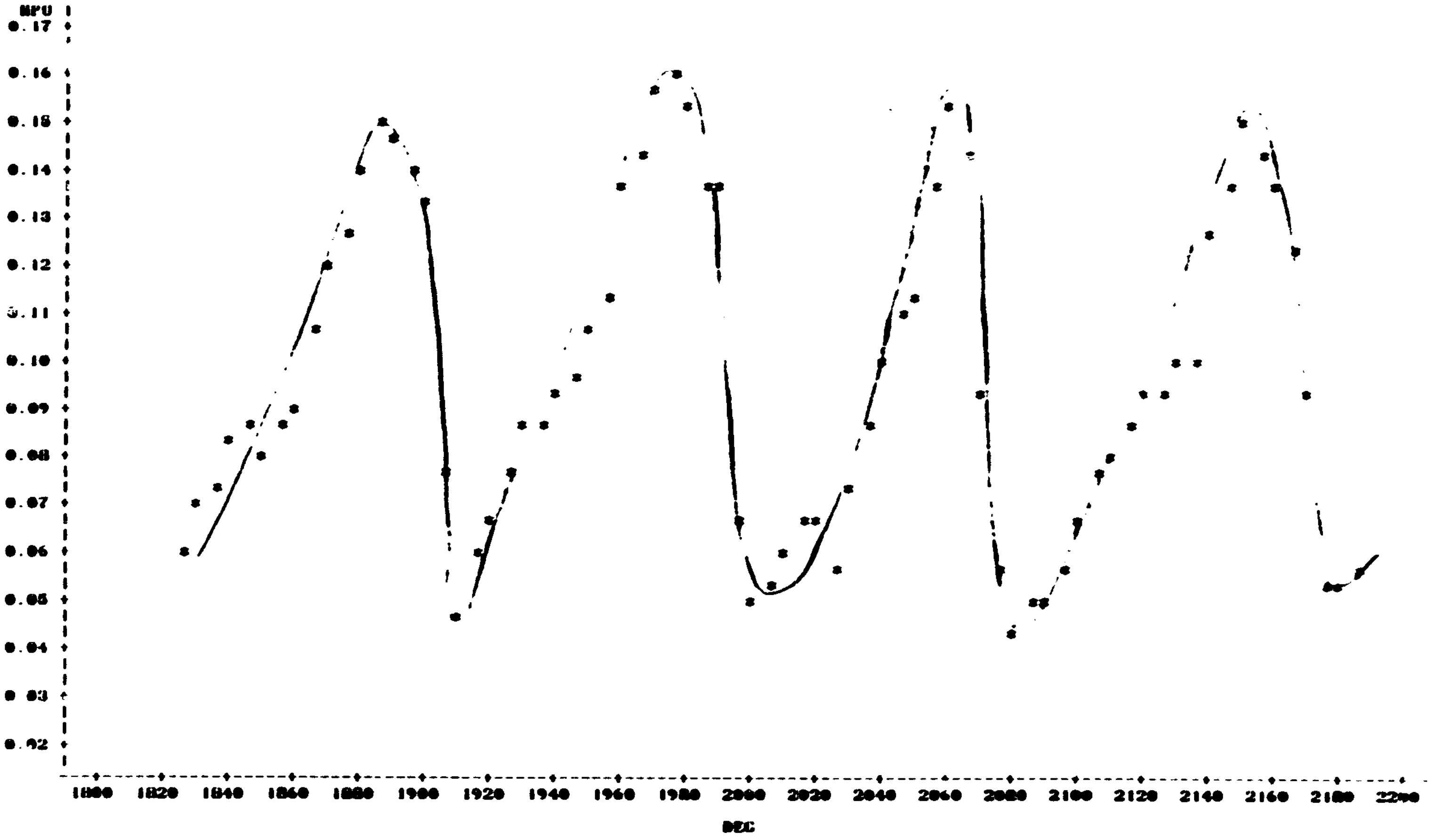

Figure 7.16. Variation of Specific Horsepower With Orientation for Aluminum With 40° Tool, Test Al 56, Revolution 1

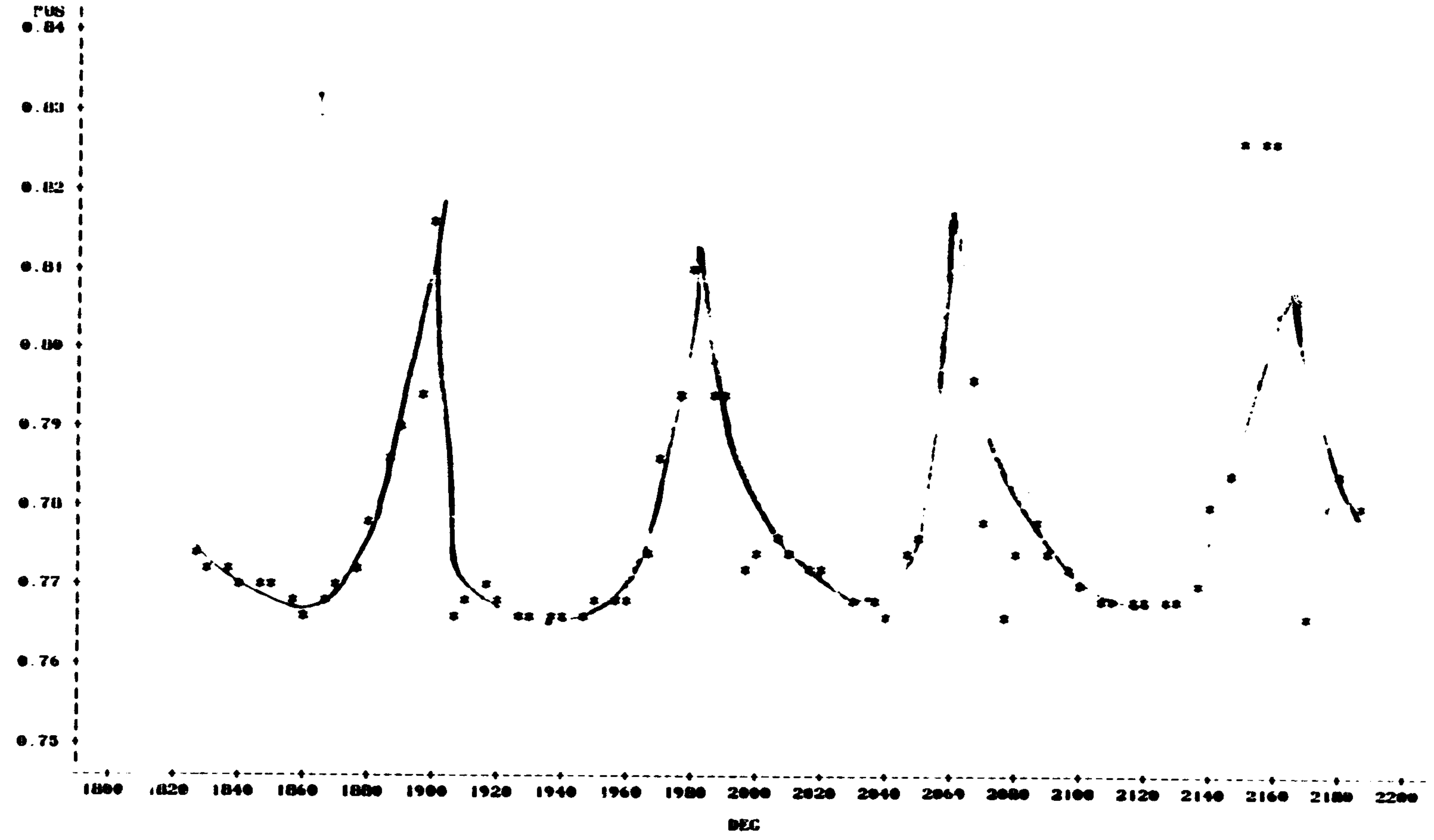

Figure 7.17. Variation of the Proportion of Shear Energy With Orientation for Aluminum With 40° Tool, Test Al 56, Revolution 1

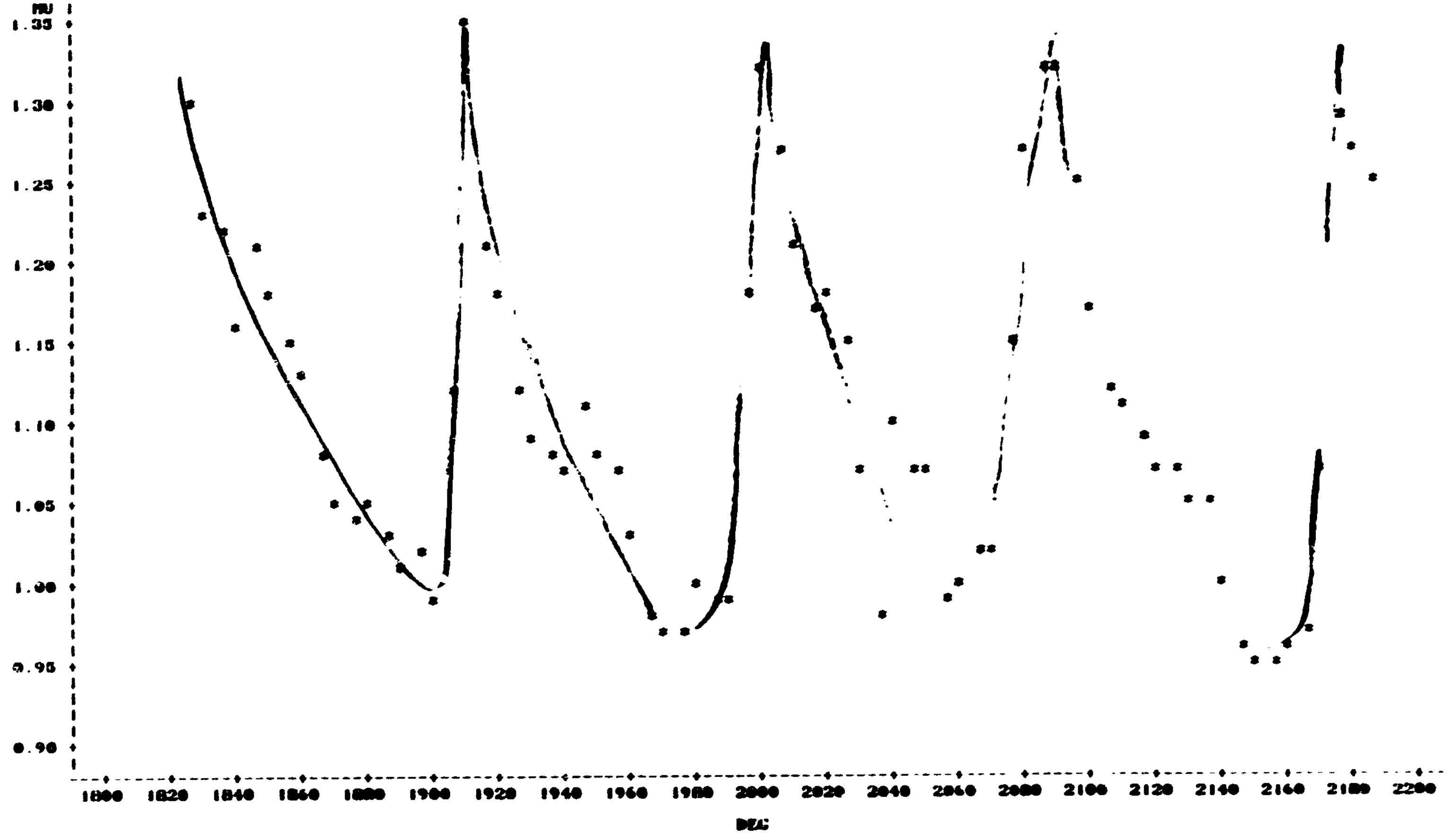

Figure 7.18. Variation of Coefficient of Friction With Orientation for Aluminum With 40° Tool, Test Al 56, Revolution 1

ORIGINAL PAGE IS
OF POOR QUALITY

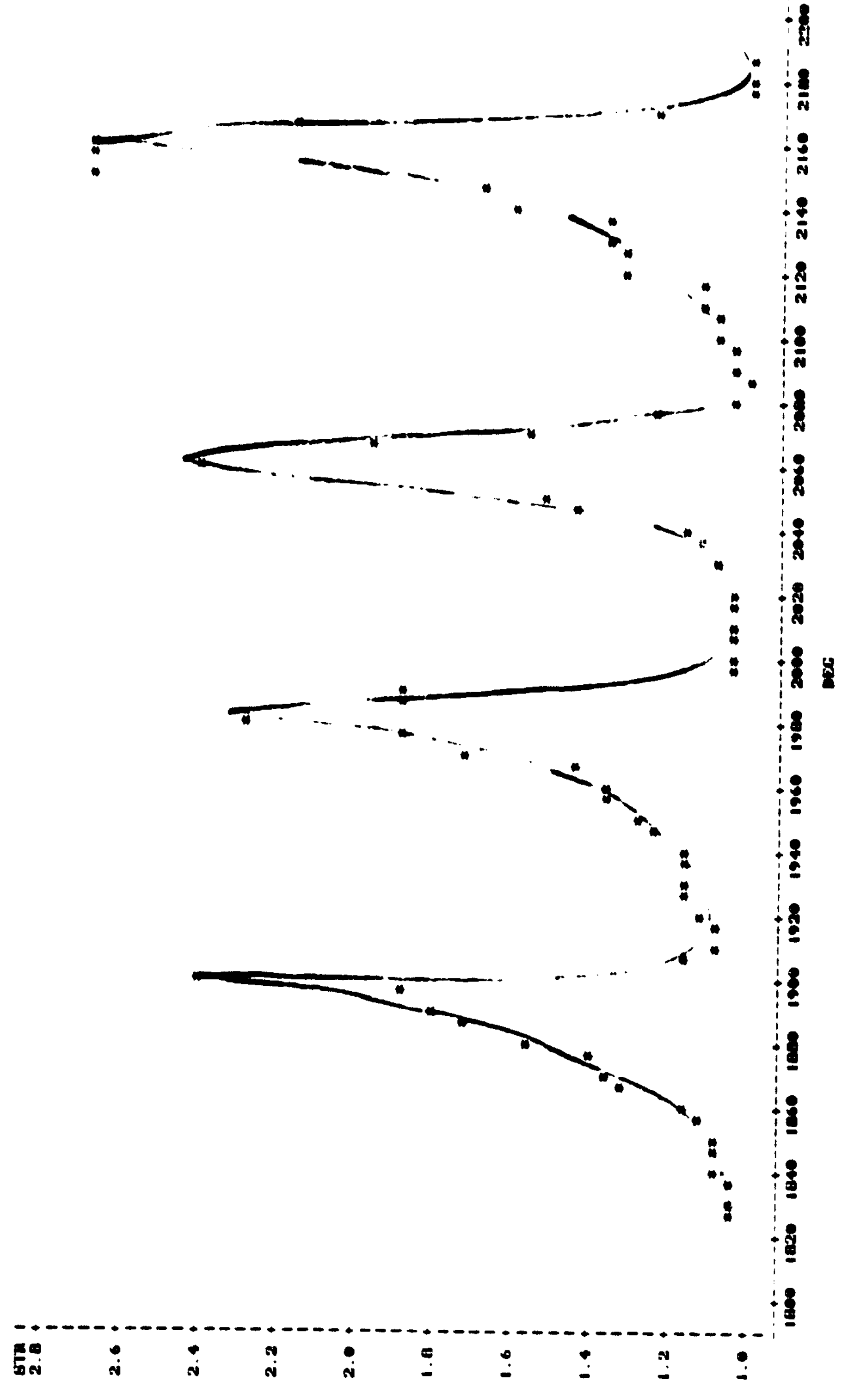

Figure 7.19. Variation of Shear Strain With Orientation for Aluminum With 40° Tool, Test Al 56, Revolution 1

Discussion of Results

Virtually every measurable and calculable quantity shows repeatable four-fold symmetry during a complete revolution about the disk. As alluded to in the previous section, in each case the crystal orientation can explain the repeatable sinusoidal variation. Specifically, the orientation of the (111)[110] and (111)[110] easy slip systems relative to the cutting direction define the phase for each. Table 7.1 summarizes the phase and period for each quantity. When the crystal is rotated such that the easy slip systems are oriented at 45 degrees to the cutting direction, then the shear plane is approximately aligned with the crystallographic slip systems of largest Schmidt factor which results in the maximum shear angle. As a result, the component forces on either shear plane or rake face are minimum as are the shear and normal stress on the shear plane.

Interestingly, the forces on the rake face, while in phase vary at different rates causing the coefficient of friction to oscilate every ninety degrees but approximately 45 degrees out of phase with the component forces such that the maximum friction occurs simultaneously with minimum forces. This explains why the proportion of energy consumed in shear is a minimum at this point. This result is supported by the single crystal friction work of Steijn(77) who found that face centered cubic materials (including

Table 7.1. Summary of the Effect of Orientation in the Machining of Single Crystals

Quantity	Symmetry	Approximate position of (111) $[\bar{1}10]$ and $(1\bar{1}1)$ [110] East Slip Systems Relative to Cutting Direction	
		Minimum	Maximum*
F_H	4-fold	45°	parallel
F_v	4-fold	45°	parallel
F_s	4-fold	45°	parallel
Fn	4-fold	45°	parallel
F	4-fold	45°	parallel
N	4-fold	45°	parallel
R	4-fold	45°	parallel
DIR ($\beta-\alpha$)	4-fold	45°	parallel
TAU (τ_s)	4-fold	45°	parallel
SN (σn)	4-fold	45°	parallel
HPU (hPu)	4-fold	45°	parallel
MU (μ)	4-fold	parallel	45°
STR (γ)	4-fold	parallel	45°
PUS (u_s/u)	4-fold	parallel	45°
PHI (ϕ)	4-fold	parallel	45°

* Small offset noted, varying with material and back rake angle.

copper) have a larger coefficient of friction in the [110] direction than the [100] direction. The maximum friction occurs in the [100] cutting direction, when the rake face of the tool is inclined at 30 to 50 degrees and is approximately parallel to the [110] direction, thus having maximum friction. Conversely, minimum friction occurs with a [110] cutting direction when the [100] direction is approximately parallel to the rake face.

These results are also consistent with the observed direction of shear. A [100] cutting direction produces the largest shear angles since there are two easy slip systems aligned at 45 degrees to the cutting direction, which is approximately parallel to the shear angle. Thus, the maximum shear angle occurs with a [100] cutting direction where there are two highly favorably oriented easy slip systems as indicated by the fact that the orientation has the minimum resolved shear stress. The alignment of the minimum shear stress is consistent for the aluminum but appears to shift for the copper, most probably due to the enormous sidespread, particularly in the [110] cutting direction. In addition, the favorable [100] direction also has the minimum proportion of energy due to shear due to high friction. These results clearly show up by the thickness of the chip or the direct measurement of shear angle. However, it is also mirrored in the chip morphology.

The surface character as well as the lamella thickness vary with crystallographic orientation on the free surface of the chip. Figure 7.20 shows the transition from an unfavorable [110] cutting direction at the bottom to the more favorable one at the top as the cutting direction approaches the [100] direction for a single crystal copper specimen with 20 degree back rake tool. The unfavorable cutting direction yields a thick chip characterized by a rough, wavey surface. As the more favorable orientation is approached, the chip thins, the roughness of the surface decreases and the thickness of the lamella decreases. This result was characteristic for both single crystal copper and aluminum for any geometry tool and is illustrated in Figures 7.21 to 7.26 for the favorable and unfavorably oriented cutting directions. This relationship between the lamella spacing and orientation is verified qualitatively by the single crystal copper results of William and Gane(51). It also verifies qualitatively what is expected from the crystallography on the free surface of the chip and calculated from the mechanics in terms of measured shear strains. A [100] cutting direction is the most favorably oriented for machining as discussed earlier. It is expected and found that this orientation produces the lowest strains as shown in Figure 7.19 and Appendix Q. Thus, the favorable orientation produces the highest shear angle and the associated lowest strain with finer lamella spacing indicating that the

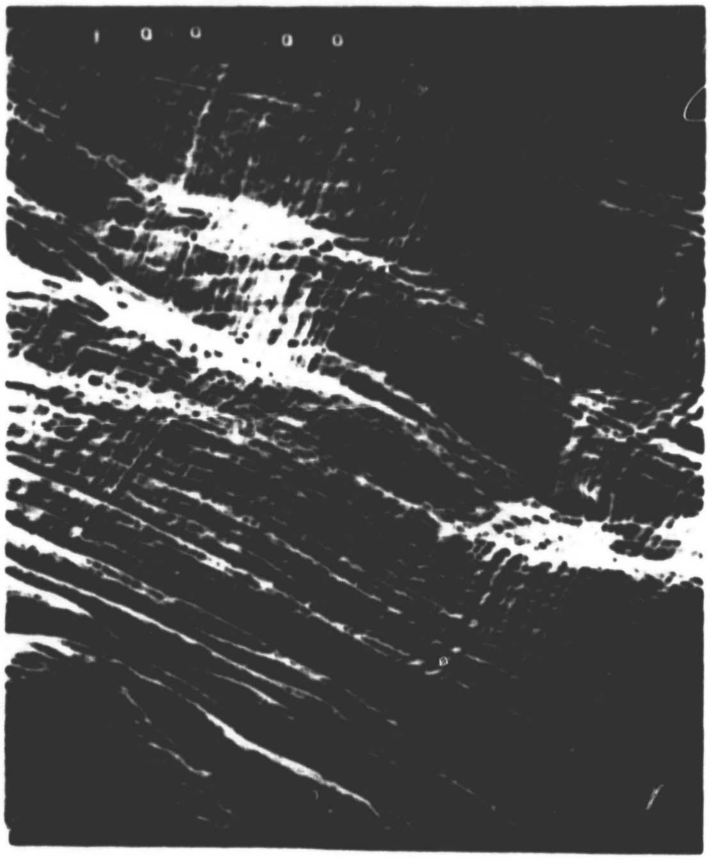

Figure 7.20. Transition From Unfavorable (Bottom) to Favorable Orientation on a Copper Chip With 20° Tool (100X)

Figure 7.21. Unfavorable Orientation on Copper Chip With 20° Tool (100X)

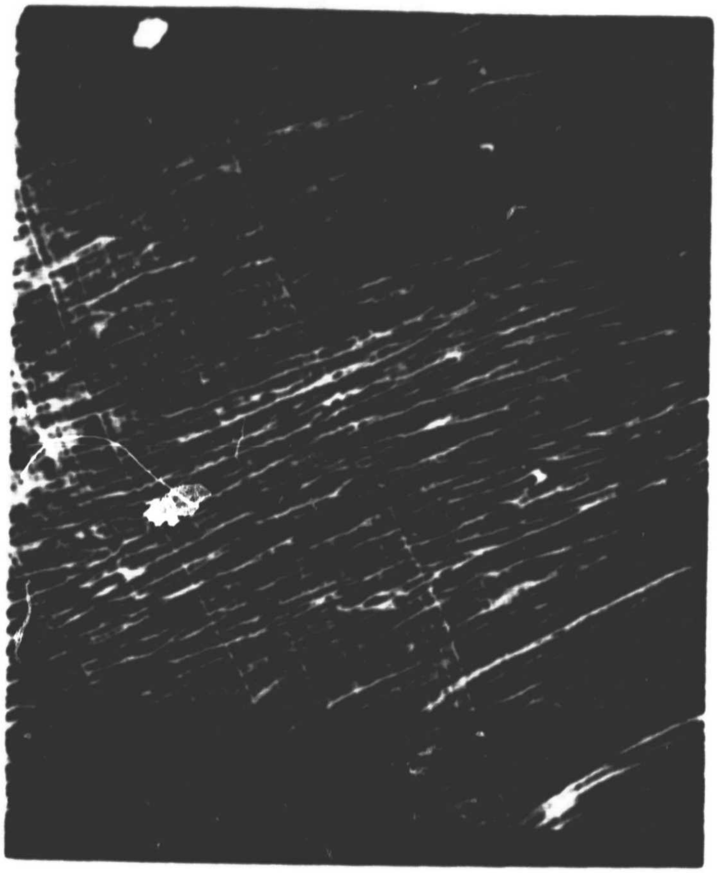

Figure 7.22. Favorable Orientation on Copper Chip With 20° Tool (100X)

Figure 7.23. Unfavorable Orientation on Aluminum Chip With 30° Tool (100X)

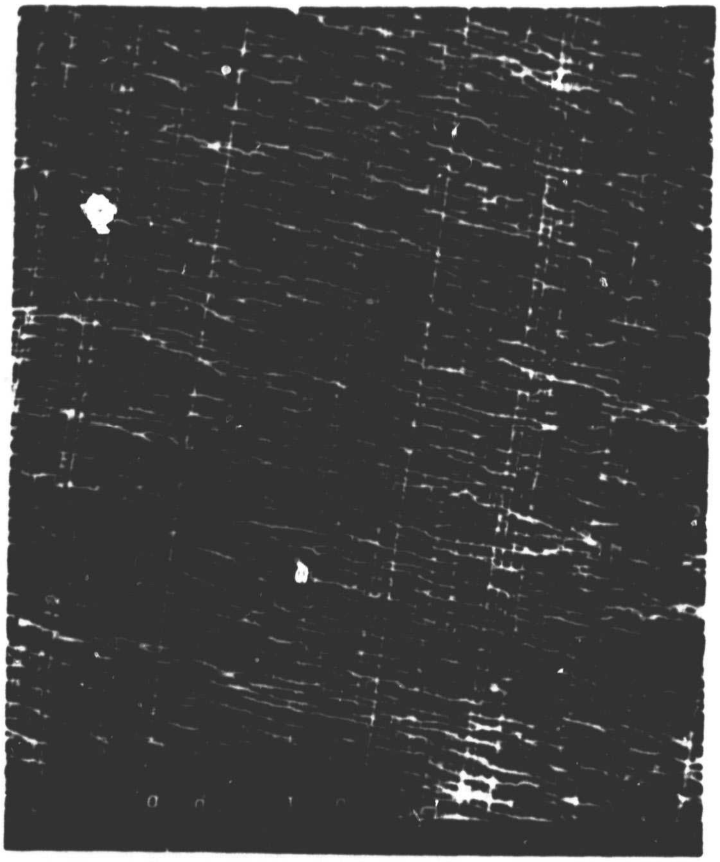

Figure 7.24. Favorable Orientation on Aluminum Chip With 30° Tool (100X)

Figure 7.25. Unfavorable Orientation on Aluminum Chip With 40° Tool (100X)

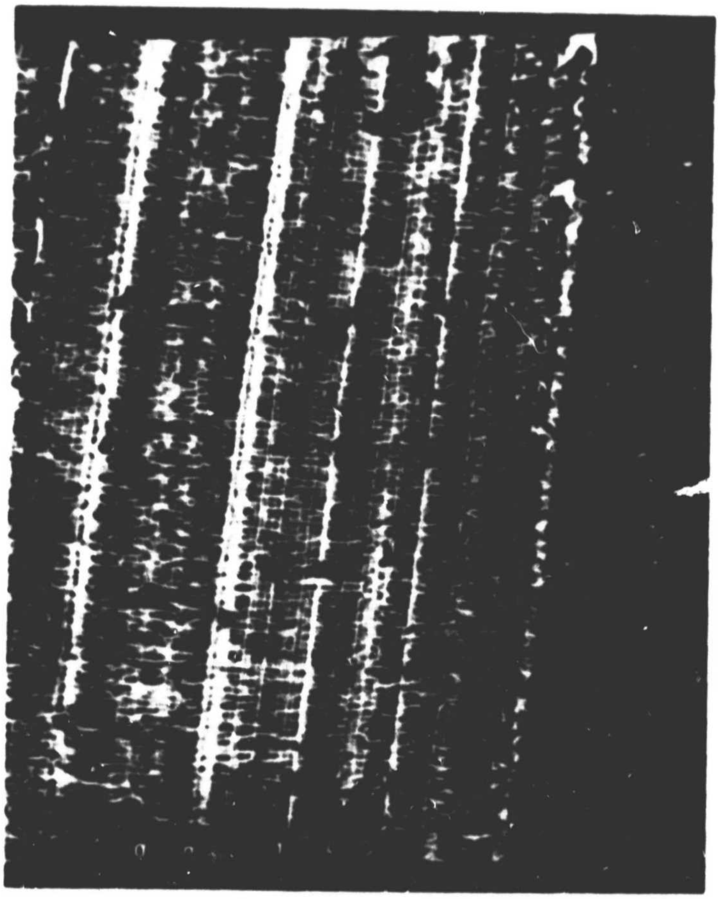

Figure 7.26. Favorable Orientation on Aluminum Chip for 40° Tool (100X)

strain rate probably becomes quite large when the (111)[110] and (111)[110] easy slip system align approximately with the shear angle such that little cross slip is necessary.

The shear angle was found to be strongly correlated to the normal stress on the shear plane (see Figure 7.27 and Appendix R) as well as the proportion of total energy consumed on the shear plane (see Figure 7.28 and Appendix S). The relationship between the proportion of energy in shear and the shear angle is very strong and exists for both single and polycrystalline metals. It should be noted, however, that for some conditions the same proportion of energy can produce two distinct measured shear angle values. This appears to happen close to the [100] and [110] directions where the slope of both the measured forces and shear angle change most rapidly. It is possible at these points for there to be a slight lag in the measured forces since they are displayed only every 0.05 seconds. The correlation might also be affected since these are the directions of minimum and maximum sidespread respectively and all of the computed mechanics are based on the assumption of no sidespread.

It is apparent from the results that the dynamic shear stress varies with crystallographic orientation in a repeatable and predictable manner for both copper and aluminum. Also, the results show a clear difference in

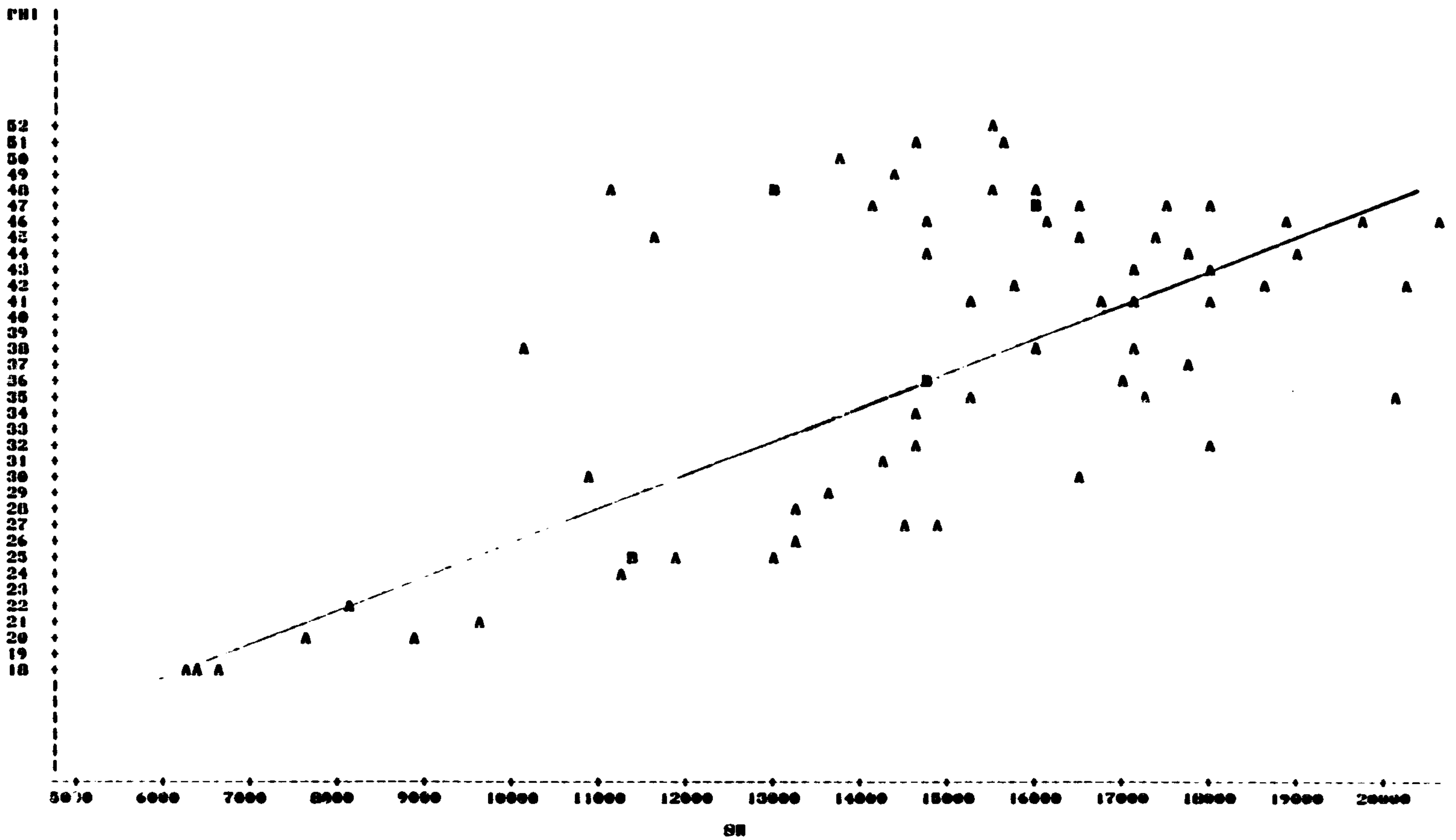

Figure 7.27. Relationship Between Shear Angle and Normal Stress on the Rake Face, Test Al 56, Revolution 1

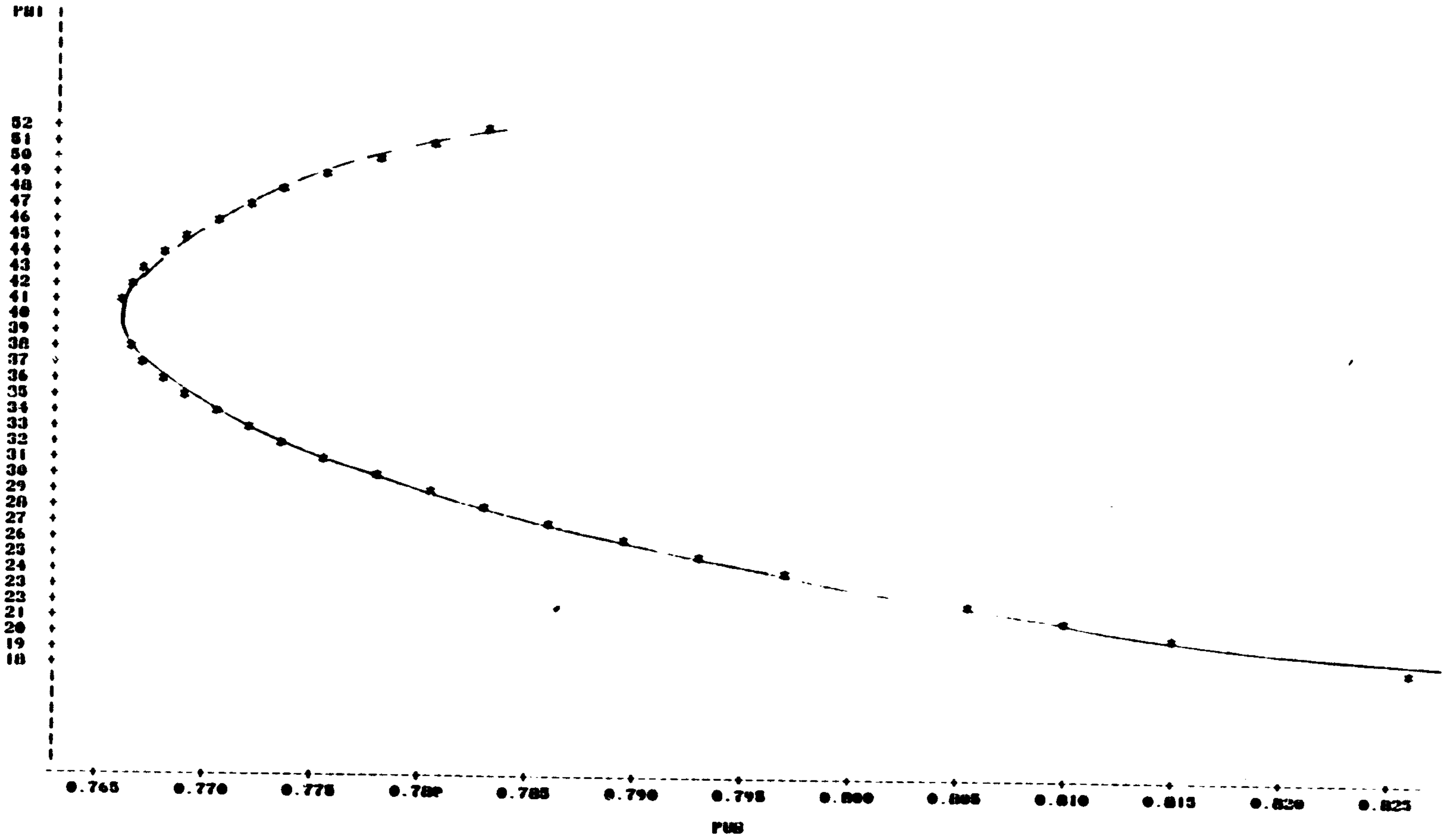

Figure 7.28. Correlation Between Shear Angle and Proportion of Energy in Shear for Aluminum With 40° Tool, Test Al 56, Revolution 1

the dynamic shear stress as a function of the back rake angle. Figure 7.29 shows the shear stress decreasing with larger rake angles accompanied by an increase in shear angle as shown in Figure 7.30 for aluminum. Copper shows the same trend with values for dynamic shear stress and shear angle given in Table 7.2. This is a result never before uncovered but should be expected since changing the tool geometry changes the only external constraint to the process, which should in turn change the geometry of the deformation (shear angle) and the magnitude of the resolved shear stress (dynamic shear stress, τ_s). Also, if one examines the resultant force, R, which acts on the shear plane and rake face as well as its direction (DIR = β-α) of application as measured from the horizontal, both are found to vary sinusoidally with minimum in the [100] direction and maximum in the [110] direction as shown in Figures 7.31 and 7.32 and Appendices R and S. Increasing the rake angle decreases the resultant force, R, and further inclines the angle of application. Thus, smaller rake angles apply larger, more direct loads to deform the single crystal with an accompanying increase in resolved shear stress.

The flow stress dependence of copper on crystallographic orientation is well documented in metal cutting (51,52,53). In addition, Mitchell(37) has documented the orientation dependence of the yield strength in tensile deformation from many sources. Most machining experiments

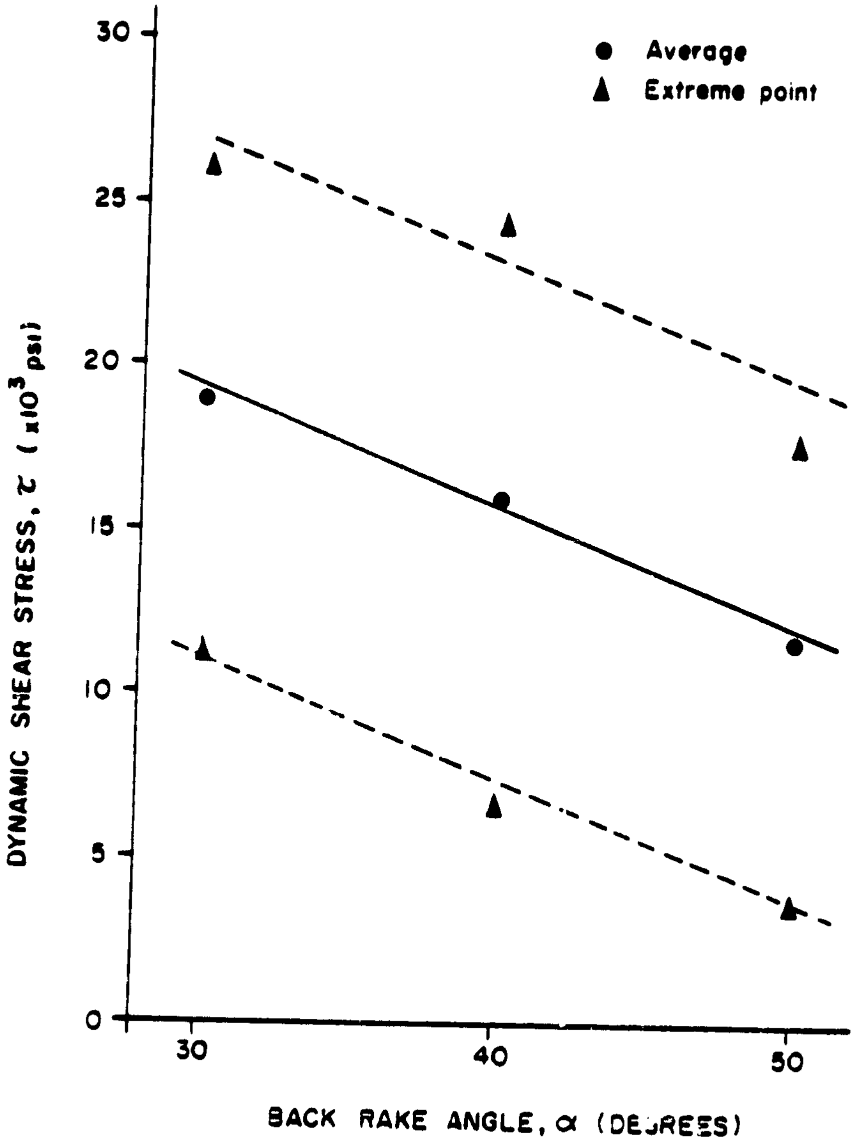

Figure 7.29. Variation of Dynamic Shear Stress With Back Rake Angle

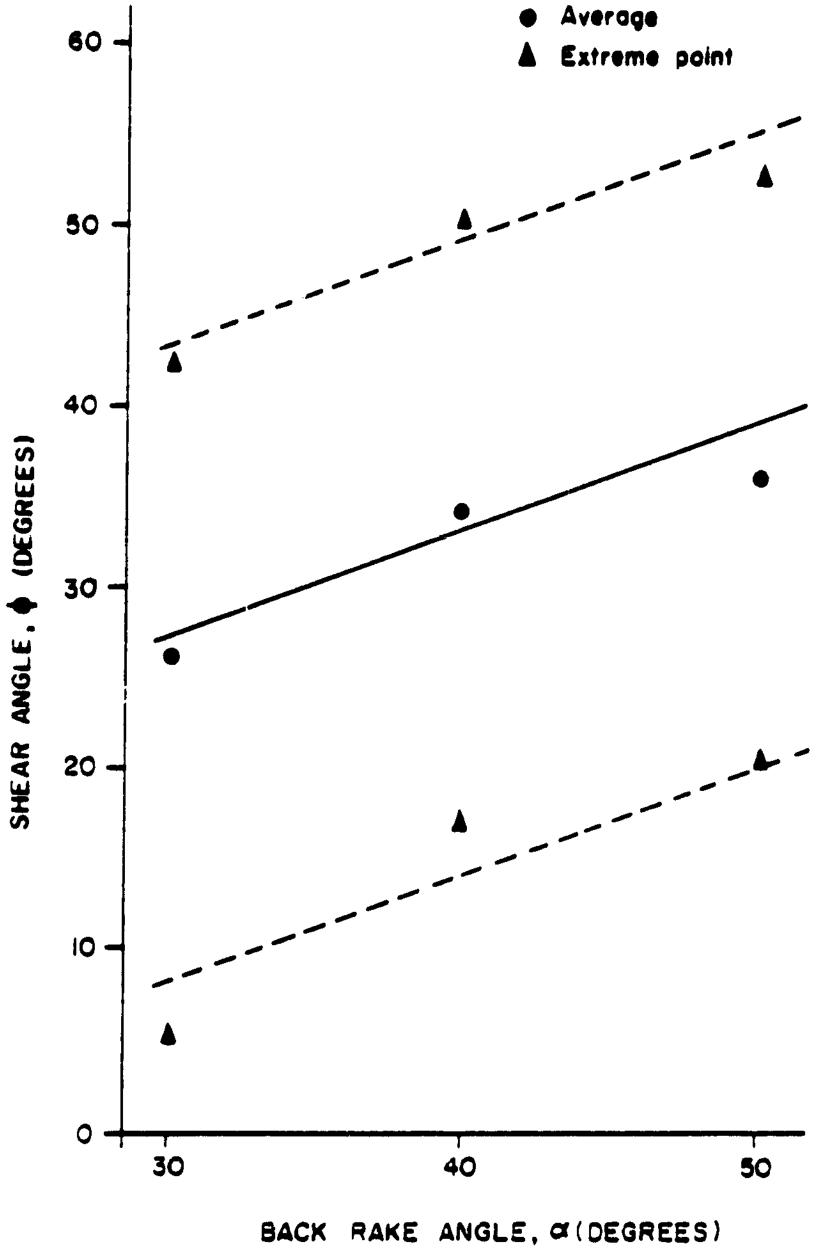

Figure 7.30. Variation of Shear Angle With back Rake Angle

Table 7.2. Variation of Dynamic Shear Stress and Shear Angle With Tool Geometry for Single Crystal Copper

Test	Back Rake Angle	Avg. Shear Stress	Avg. Shear Angle
Cu 1	40°	46,297 psi	19.9°
Cu 6	20°	51,428 psi	8.95°
Cu 33	30°	51,877 psi	15.4°

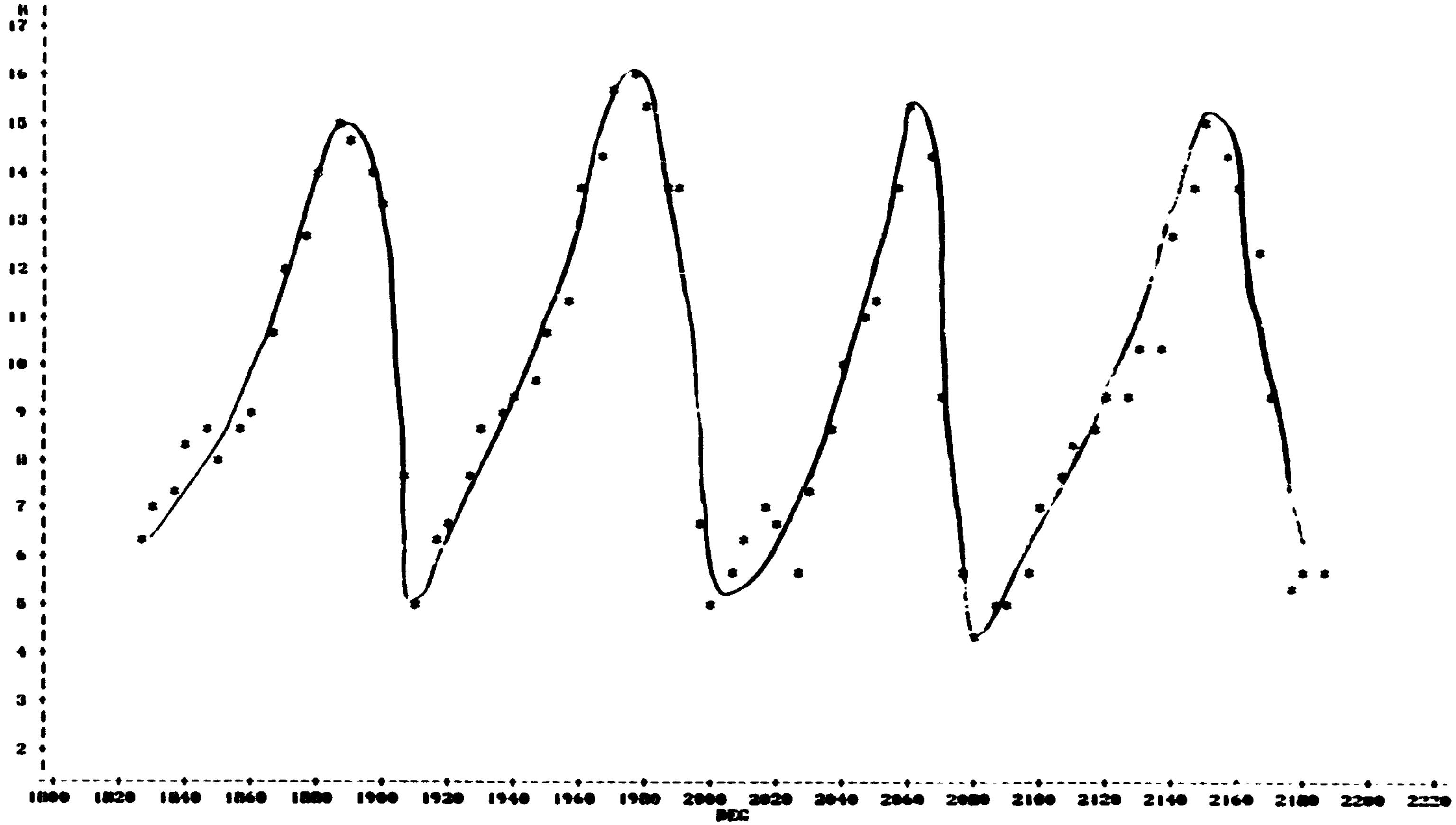

Figure 7.31. Variation of Resultant Force With Orientation for Aluminum With 40° Rake, Test Al 56, Revolution 1

ORIGINAL PAGE IS
OF POOR QUALITY

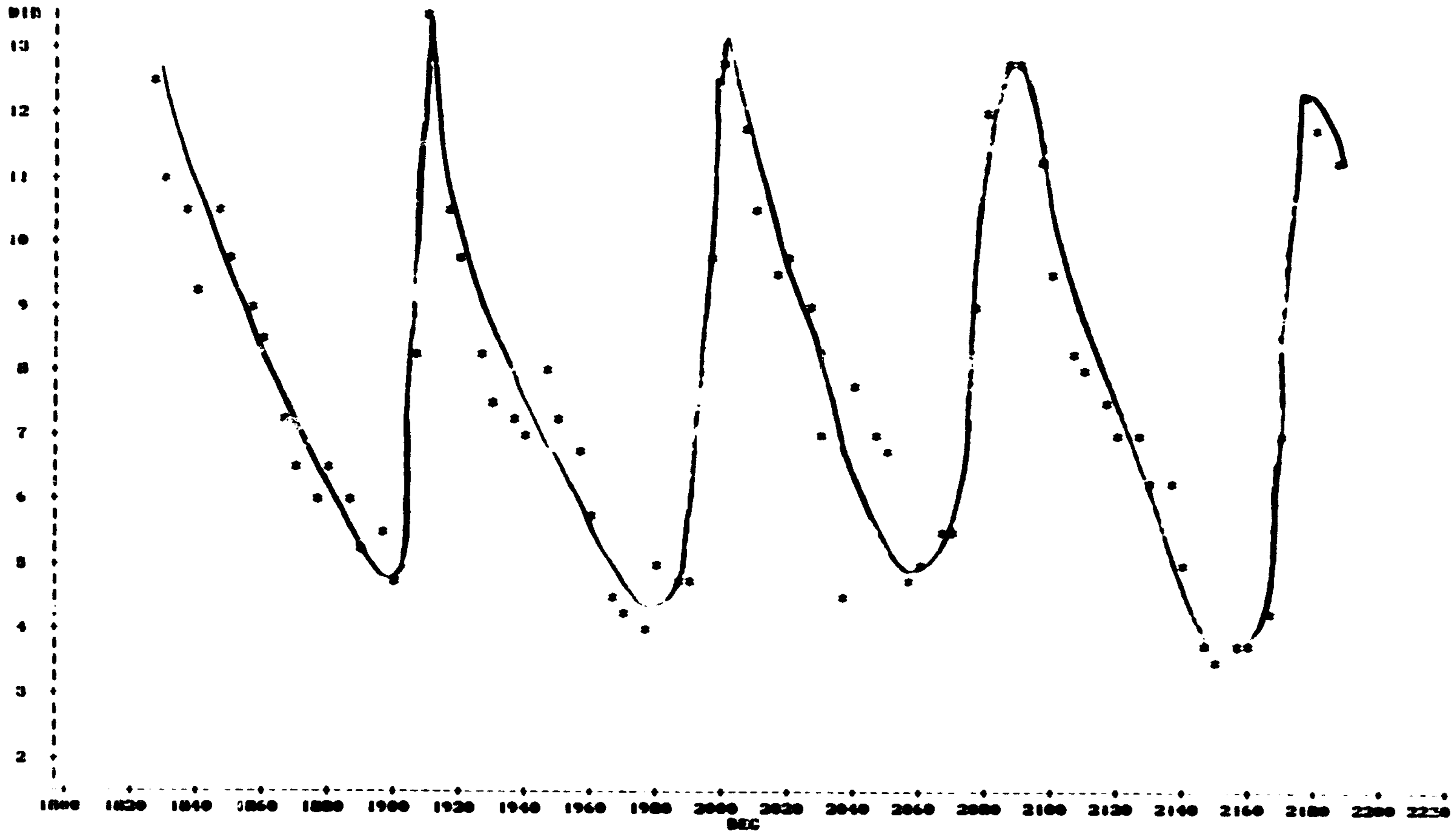

Figure 7.32. Variation of Resultant Force Direction for Aluminum With 40° Tool, Test Al 56, Revolution 1

on aluminum, however, fail to show any effect of crystallographic orientation on flow stress(19,52,54). This was generally explained by the differences in stacking fault energy between aluminum and copper. Aluminum with high stacking fault energy (200 ergs/cm) and narrowly separated partial dislocations was thought to be able to recombine easily, thus the orientation independence of the flow stress. However, aluminum does show an orientation dependence of the critical resolved shear stress in tensile deformation (37,79). The primary reason for the opposite result and conclusion in metal cutting lies in the specific orientations selected for cutting. The orientations selected by Ramalingam and Hazra(19) were random, thus they were unable to select orientations which might represent the extremes in terms of their flow stress nor were they able to look for systematic variations. Horne(52) machined a limited number of orientations for both copper and aluminum. Closer examination of his results shows that the (110)[110] orientation gave the lowest resolved shear stress for copper. This favorable orientation was not, however, run for aluminum, thus making it difficult to draw a comparative conclusion between the orientation dependence of aluminum and copper.

Thus, the results obtained in this study for aluminum are consistent with single crystal tensile data and differ from current machining results due to the orientations cut.

There is, however, one machining study which selected four of the orientations cut on the aluminum disk specimen(80). The cutting conditions, using a 35 degree back rake angle, 0.004 inch depth of cut and 0.065 in/sec are also close to those used during the in-situ testing. The results of Sata, et. al. clearly demonstrate the orientation dependence of the flow stress in metal cutting. The shear stress values generated at each orientation were also close to those calculated from the in-situ testing.

Current literature does not agree whether the dynamic shear stress for a polycrystalline material attains the average or the most unfavorable stress developed in the machining of single crystals. It appears from this research that the polycrystalline material takes on an average value over all orientations and all back rake angles. Referring to θ as the designation for orientation and α for the back rake angle, the polycrystalline shear stress may be expressed as

$$\tau_s\Big|_{\text{polycrystalline}} = \int_\alpha \int_\theta \tau_s(\theta,\alpha)\, \alpha\theta \, d\theta \, d\alpha \qquad (7.1)$$

or designating the absolute orientation between the tool rake face the the crystal as θ^*,

$$\tau_s\Big|_{\text{polycrystalline}} = \int_{\theta^*} \tau_s(\theta^*)\, \theta^* \, d\theta^* \qquad (7.2)$$

Thus, single crystal machining results may be extended to gain an understanding of the polycrystalline material.

CHAPTER VIII

CONCLUSIONS

Metal cutting is a unique deformation process characterized by large strains, exceptionally high strain rates and few constraints to the deformation. These factors, along with the difficulty of directly measuring the shear angle, make chip formation difficult to model and understand. One technique for skirting the difficulty of post mortem chip measurement is to perform a cutting experiment dynamically in a scanning electron microscope.

The performance of the in-situ experiment with full instrumentation which allows for component force measurement, orientation measurement (on a round single crystal disk) and a timing device, all superimposed below the deformation on the T. V. monitor and recorded for future viewing. This allows the shear angle to be directly measured for the screen along with the other needed information. This method allows for a much more accurate determination of the shear angle. In addition, the experiment is performed in a highly controlled and consistent environment where high magnification and resolution viewing of the process is possible and can be used to gain a better quantitative and qualitative understanding of the process.

C-3

Thus, in-situ machining provides a unique opportunity for studying the metal cutting process.

The machining of polycrystalline 2024-T351 aluminum allowed for the accurate measurement of both the shear and chip velocities. Both quantities were found to be reasonably close to the theoretical values calculated from the mechanics. Thus, the velocity triangle for metal cutting was verified. This represents the first measurement and verification of the shear and chip velocities since the mechanics formulation was published 36 years ago.

The in-situ deformation of single crystal aluminum and copper through continuously changing orientations within the microscope provides a unique opportunity to study single crystal deformation over a wide range of orientations in an orderly manner. Machining around the periphery of a (001) zone axis disk produced four-fold symmetry of measured force components (both vertical and horizontal) and shear angle. The [100] cutting direction proved to be the most favorable with lowest forces and highest shear angle since two slip systems, the (111)[110] and $(1\bar{1}1)[110]$ are aligned at 45 degrees to the cutting direction, approximately parallel to the shear angle. The minimum resolved shear stress was also found in this orientation. For the analogous reasoning, the forces and shear stress are maximum and shear angle minimum at the same orientation, which is somewhat offset from the [110] cutting direction.

All component forces on the shear plane and rake face maintain the same period and phase as the measured components as does the specific horsepower and shear strain. Friction, however, is in phase with the shear angle. The [100] cutting direction yields the highest coefficient of friction on the rake face since the [110] direction is approximately parallel to the rake face. The high friction causes the proportion of energy in shear to be a minimum in this orientataion with the resulting large shear angle. For this reason, the proportion of energy in shear has a high correlation to the measured shear angle.

Chip morphology was also found to correlate to crystallographic orientation with the favorable [100] direction having finely spaced lamella and the unfavorable [110] direction having widely spaced lamella.

The resolved shear stress and shear angle were also found to be dependent on tool geometry (back rake angle). This should be expected since changing the inclination of the rake face changes the only constraint to the process. This manifests itself by having lower rake angle tools deform the single crystal with a larger, more direct-acting resultant force which causes a higher resolved shear stress at lower shear angles. The dynamic shear stress for a polycrystalline fcc metal was also found to be the average resolved shear stress value over all crystallographic orientations and all tool geometries.

Thus, the in-situ machining of single crystals has helped to explain how the cutting process operates as well as how single crystal results may be applied at an elementary level towards an understanding of the behavior of polycrystalline materials in machining.

The results presented in this dissertation represent a first study in the use of a fully instrumented in-situ machine tool to understand the metal cutting. Much of the work done represents the first such experimentation of its kind due to the unique opportunity presented by the in-situ apparatus which allows full instrumentation as well as a permanent visual record of the deformation. However, these experiments and the results derived thereof represent only a small fraction of the potential value of in-situ machining experiments.

Fully instrumented in-situ machining has the potential to greatly extend the current state of knowledge in chip formation. The apparatus designed could be used to study

1. The formation and dynamic stability of the built-up edge as well as the effect of workpiece material, cutting tool (geometry, material, surface preparation), and depth of cut.
2. The role of the nose radius of the cutting tool in determining the mode of material deformation (machining or rubbing) as the incursion depth is varied.

3. The affect of controlling the contact length on the rake face of the tool. This would allow a high controlled study of this area as well as the ability to extend this work into the general area of chip curl and the use and mechanics of chip breakers.
4. The nature and distribution of secondary shear on the rake face.
5. The dynamics and formation of the fundamental shear front-lamellae structure in metal cutting.
6. The effect and dynamics of inclusions on the metal cutting process and their influence on machinability.
7. The effect of crystallography on the chip formation for BCC single crystal metals.
8. The effect of crystallography on the chip formation of HCP single crystal metals.
9. The effect of nose radius on the phenomena of major and minor force peaks(53,54).

With some retrofitting, the apparatus designed could control the bulk workpiece temperature. A full range of experiments dealing with temperature effects in metal cutting could then be performed with special emphasis on the change in machining properties (dynamic shear stress, specific horsepower, frictional shear stress) and geometry (shear angle). In addition, the influence temperature of crystallographic effects could be studied.

In conclusion, fully-instrumented in-situ devices for plastic deformation hold tremendous potential towards the development of a full understanding of plastic deformation processes and should continue to receive attention in the future.

BIBLIOGRAPHY

1. Armarego, Brown, The Machining of Metals, Prentice Hall, Inc., 1969.

2. Ernst, "Physics of Metal Cutting", Machining of Metals, ASM, 1938, p. 24.

3. Merchant, "Mechanics of the Metal Cutting Processes I, II", Journal of Applied Physics, Vol. 16, 1945, pp. 267-285.

4. Boothroyd, Fundamentals of Metal Machining and Machine Tools, McGraw-Hill, 1975.

5. Shaw, Metal Cutting Principles, 2nd ed., The M.I.T. Press, Cambridge, 1957.

6. Vidosic, Metal Machining and Forming Technology, The Ronald Press Company, 1964.

7. Cook, Manufacturing Analysis, Addison-Wesley Publishing Company, 1966.

8. Boston, Metal Processing, 2nd ed., Wiley, New York, pp. 160-167.

9. ASTME, Machining With Carbides and Oxides, McGraw-Hill, New York, 1962, pp. 88-93.

10. Machining-Theory and Practice, American Society of Metals, Cleveland, 1950, pp. 218-340.

11. Schmidt, Roubik, Hug, "Measuring Forces in Metal Cutting", Tool Mfg. Eng., March 1961, pp. 71-74.

12. Micheletti, "Notes on Machinability of Metals Measured Through Cutting Energy and Tool Wear", Adv. in Machine Tool Design and Research, 1962, pp. 109-120.

13. Black, J. T., "Momentus Methods on Energy Measurements in Metal Cutting", Int. J. Mach. Tool Des. and Res., Vol. 5, Pergamon Press, 1965, pp. 223-231.

14. Cohen, P. H., Black, J. T., "Development of a Standard Machining Data Machine", Proceedings NAMPC VIII, May 1980, pp. 258-265.

15. Cook, Shaw, Finnie, "Shear Angle Relationship in Metal Cutting", Trans. Amer. Soc. Mech. Eng., 75 (1953), p. 273.

16. Shaw, M. C., *Modern Approaches to Machining Problems*, University of Michigan Short Course, 1959.

17. Kainth, Gupta, "Shear Angle Relationships with Variable Undeformed Chip Thickness", Trans. ASME, Nov. 1974, pp. 1272-1276.

18. Kobayashi, Thompsen, ASME, Journal of Engineering for Industry, Vol. 81, 1959, p. 251.

19. Ramalingam, Hazra, "Dynamic Shear Stress-Analysis of Single Crystal Machining Studies", ASME Publication 72-WA/PROD-20.

20. Rowe, G. W., Spick, P. T., Trans. ASME, 89B, 530 (1967).

21. Wright, P. K., Schmidt, P. F. V., "Minimum Energy Approach to Metal Cutting", Report No. 78/16, University of Aukland, June 1978.

22. Usui, E., Hivota, A., Masuko, M., "Analytical Prediction of Three Dimensional Cutting Process, Part I", J. Eng. Ind., Volume 100, May 1978, pp. 222-228.

23. Usui, E., Hivota, A., "Analytical Predition of Three Dimensional Cutting Process, Part 2", J. Eng. Ind., Volume 100, May 1978, pp. 229-235.

24. Usui, E., Shirakashi, T., Kitagawa, "Analytical Prediction of Three Dimensional Cutting Process, Part 3", J. Eng. Ind., Volume 100, May 1978, pp. 236-243.

25. Palmer, W. B., Oxley, M. A., "Mechanics of Orthogonal Machining", Proc. Inst. Mech. Engrs., Volume 173, NO. 24, 1959.

26. Black, "Thin Film Orthogonal Machining", Trans. ASME, 1970.

27. von Turkovich, "Dislocation Theory of Shear Stress and Strain Rate in Metal Cutting", Advances in Machine Tool Design and Research, 1967.

28. Black, 1974 Proceedings NAMRC-II, Madison, Wisconsin, 1974, p. 504.

29. Ramalingam, Trigger, "On the Dynamic Shear Stress of Dispersion Hardened Alloys", Advances in Machine Tool Design and Research, Pergamon Press, 197o, pp. 565-584.

30. Black, "On the Fundamental Mechanism of Large Strain Plastic Deformation", ASME, Journal of Engineering for Industry, May 1971, pp. 507-526.

31. Black, "Shear Front-Lamella Structure in Large Strain Plastic Deformation Processes", ASME, Journal of Engineering for Industry, Feb. 1972, pp. 307-316.

32. Black, "Flow Stress Model in Metal Cutting", ASME Publication No. 78-WA/PROD-27.

33. Baily, Bhanvadia, "Correlation of Flow Stress with Strain Rate and Temperature During Machining", ASME Publication 73-Mat-E, 1973.

34. Sata, "Flow Stress in Metal Cutting", Sci. Papl I.P.C.R., Vol. 53, pp. 188-200.

35. Wright, Robinson, "Material Behavior in Deformation Zones of Machining Operation", Metals Technology, May 1977, pp. 200-248.

36. Schmidt, E., Boas, W., Plasticity of Crystals, F. A. Hughes and Co., London, 1950.

37. Mitchell, T. E., "Dislocations and Plasticity in Single Crystals of Face-Centered Cubic Metals and Alloys", Progress in Applied Materials Research, Volume 6, 1964.

38. Clarebrough, L. M., Ogilvie, G. J., "Microstructure by Machining", Machining-Theory and Practice, ASM, 1950, pp. 110-121.

39. Phillips, R., "A Study of Metal Cutting by the Examination in the Electron Microscope of Sections Cut with a Diamond Knife", Annual Report FTR No. 1-AEON Laboratories, November 30, 1959.

40. Phillips, R., Brit. J. Applied Physics, 11, 504, (1960).

41. Phillips, R., Brown, A., "The Theory of Microtome Sectioning with an Infinitely Sharp Cutting Edge", Annual Report FTR No. 2, February 28, 1961.

42. Phillips, R., Brit. J. Applied Physics, 12, p. 554.

43. Phillips, V. A., Phil. Mag. 5, 1960, p. 571.

44. Phillips, V. A., "The Use of the Diamond Knife Ultramicrotome in Light and Electron Microscopy on Metals, Praktische Metallographic 4, 1967.

45. Phillips, V. A., in Direct Observation of Imperfections in Crystals, J. B. Newkirk and J. H. Wernick, eds. (John Wiley and Sons, Inc., New York, 1961), p. 179.

46. Ahlers, M. Vassamillet, L. F., "Deformation of Some fcc Metals by Ultramicrotomy", Journal of Applied Physics, Vol. 39, No. 8, 1968, p. 3592.

47. Ogura, I., "Ultra-Microtomy for Electron Microscopie Observation of Metal Structures", J. of the Second College of Engineering, Nihon U., Series B., Vol. 6, March, 1965.

48. Ogura, I., "Plastic Deformation in the Ultramicrotomed Thin Slices of HCP Metal Crystals", Unpublished, 1972.

49. Black, J. T., "Plastic Deformation in Ultramicrotomy of Copper and Aluminum", Ph.D. Dissertation, 1969.

50. B. F. VonTurkovich, J. T. Black, "Micro Machining of Copper and Aluminum Crystals", Trans. ASME, Vol. 92B, No. 1, February 1970, p. 130.

51. Williams, J. A., Gane, N., "Some Observations on the Flow Stress of Metals During Metal Cutting", Wear, 42 (1977), pp. 341-353.

52. Horne, J. G., Ph.D. Dissertation, University of Cambridge, 1978.

53. Shih, A., Masters Thesis, The Ohio State University, 1978.

54. Cohen, Black, Horne, Shih, "Orthogonal Machining of Single Crystals", Proceedings NAMRC-IX, May 1981.

55. Veda, K., Iwata, K., "Chip Formation Mechanism in Signle Crystal Cutting of B-Brass", Journal CIRP, 1980.

56. Hamza, A. A., "The Presnet Development of Dynamic Experiments in the Specimen Chamber of the SEM", Scanning Electron Microscopy/1977, Volume I.

57. Ramalingam, S., Bell, A. C., "A SEM Stage For the Observation of Chip Formation", *Rev. of Sci. Instrum.*, Vol. 44, No. 5, May 1973.

58. Huertel, A., Courtel, R., Maugis, D., "Apparatus for the Measurement of Friction on Thin Foils Inside an Electron Microscope", *Journal of Physics*, Vol. 9, 1976.

59. Brainard, W. A., Buckley, D. H., "Dynamic SEM Wear Studies of Tungsten Carbide Cermets", *NASA Technical Memorandum* TM X-71659, 1975.

60. Joy, D. C., Newbury, D. E., "Dynamic Studies of Deformation Mechanisms in the SEM", *Electron Microscopy*/1977, Volume I.

61. Lashmore, D. S., Gardner, R. N., Jesser, W. A., "A Technique for Preparation of Tensile Samples with an Improved Geometry for In-Situ Electron Microscopy Studies", *Journal of Physics*, Vol. 9, 1976.

62. Pond, R. D., Smith, D. A., Southerden, P. W. J., "On the Role of Grain Boundary Dislocations in High Temperature Creep", *Philosophical Magazine A*, 1978, Vol. 37, No. 1, pp. 27-40.

63. Bell, A. C., Ramalingam, S., Black, J. T., "Dynamic Metal Cutting Studies as Performed in the SEM", *Proceedings NAMRC-II*, 1973.

64. Black, J. T., Ramalingam, S., "Dynamic Metal Deformation Studies in the JSM-03 SEM", *JEOL News*, Vol. 113, No. 1, 1973.

65. Iwata, K., Ueda, K., "Crack Nucleation and its Propagation in Discontinuous Chip Formation Performed Within an SEM", *Proceedings NAMRC-III*, May 1975.

66. Iwata, K., Ueda, K., "The Effect of Lead on Crack Behavior of Leaded Free Machining Steel During Controlled Cutting Temperature Micro-Machining", *Proceedings, NAMRC-IV*, May 1976.

67. Dingley, D. J., Micron, 1, 2, p. 261, 1969.

68. Hearle, J. W. S., Sparrow, J. T., and Cross, P. M., *The Use of the Scanning Electron Microscope*, Pergamon Press, Osford.

69. Wright, P. K., Horne, J. G., Tabor, D., "Boundary Conditions at the Chip-Tool Interface in Machining: Comparisons Between Seizure and Sliding Friction", Wear, Vol. 54 (1979), pp. 371-390

70. Bailey, J., "Friction in Metal Machining-Mechanical Aspects", Wear, Vol. 31 (1975), pp. 243-475.

71. Zorev, N. N. Metal Cutting Mechanics, Pergamon Press, 1966.

72. Chandrasekaran, H., Kapoor, D. V., "Photoelastic Analysis of Tool-Chip Interface Stresses", J. Ind. Eng., Volume 87, No. 4, November 1965, pp. 495-502.

73. Usui, E., Takayama, H., "A Photoelastic Analysis of Machine Stresses", J. Eng. Ind., November 1960, pp. 303-308.

74. Kato, S., Yamaguchi, K., Yamada, M., "Stress Distribution at the Interface Between Tool and Chip in Machining", J. of Eng. Ind., May 1972, pp. 683-889.

75. Hsu, T. C., "A Study of the Normal and Shear Stresses on a Cutting Tool", J. Eng. Ind., February 1966, pp. 51-64.

76. Cohen, P. H., Master's Thesis, The Ohio State University, 1979.

77. Steijn, R. P., "Friction and Wear of Single Crystals", Mechanisms of Sliding Friction, Elsevier Publishing Company, 1964.

78. Tuan, C. H., Masters Thesis, The Ohio State University, 1981.

79. Murakami, H., Kataoka, Y., Yoshida, S., "Orientation Dependence of Critical Resolved Shear Stress of Aluminum", Crystal Lattice Defects, Volume 8, 1979, p. 107.

80. Sato, M., Kato, Y., Kazuhiro, T., "Effects of Crystal Orientation on the Flow Mechanism in Cutting Aluminum Single Crystal", Trans. JIM, Vol. 20, 1979, p. 414.